ISSN en trámite

Geofísica Internacional

Revista Trimestral Publicada por el Instituto de Geofísica de la Universidad Nacional Autónoma de México

México
Volume 61 Number 2
April - June
2022

— Geofísica Internacional —

GEOFÍSICA INTERNACIONAL, Año 61, Vol. 61, Núm. 2, abril - junio de 2022 es una publicación trimestral, editada por la Universidad Nacional Autónoma de México, Ciudad Universitaria, Alcaldía Coyoacán, C.P. 04150, Ciudad de México, a través del Instituto de Geofísica, Circuito de la Investigación Científica s/n, Ciudad Universitaria, Alcaldía Coyoacán, C.P. 04150, Ciudad de México, Tel. (55)56 22 41 15. URL: http://revistagi.geofisica.unam.mx, correo electrónico: revistagi@igeofisica.unam.mx. Editora responsable: Andrea Rostan Robledo. Certificado de Reserva de Derechos al uso Exclusivo del Título: 04-2022-081610251200-102, ISSN: en trámite, otorgados por el Instituto Nacional del Derecho de Autor (INDAUTOR). Responsable de la última actualización Saúl Armendáriz Sánchez, Editor Técnico. Fecha de la última modificación: 31 de marzo 2022, Circuito de la Investigación Científica s/n, Ciudad Universitaria, Alcaldía Coyoacán, C.P. 04150, Ciudad de México.

Geofísica Internacional
Vol. 61, Núm. 2, abril-junio de 2022

Contents

New insights into the seismic activity of Damascus fault (Syria): a quantitative analysis
Mohamad Khir Abdul-Wahed
88

Assessment of the tectonic effects on soil radon activity along the margin of the Arabian plate boundary in northwestern Syria
Mohamed Al-Hilal
100

Seismic risk in the State of Colima, México: Application of a simplified methodology of the seismic risk evaluation for the localities with low-rise, non-engineered housing
Vyacheslav Zobin
114

Voyager's observations in the vicinity of the heliopause
Rogelio Caballero, J. D. Richardson
144

Original paper

https://doi.org/10.22201/igeof.00167169p.2022.61.2.2054

New Insights into the Seismic Activity of Damascus Fault (Syria): a Quantitative Analysis

Mohamad Khir Abdul-Wahed[1*]

Received: May 21, 2020; accepted: January 27, 2022; published on-line: April 1, 2022.

Resumen

La falla de Damasco es una estructura tectónica inversa notable que atraviesa la ciudad de Damasco; posiblemente representa un riesgo sísmico significativo para la ciudad. En ese sentido, el presente trabajo examina la actividad sísmica instrumental y establece un catálogo de terremotos que cubre el período de 1995 a 2012 para esta importante falla, lo anterior con el objetivo de identificar su contribución a la amenaza sísmica regional. El análisis cuantitativo revela que la falla de Damasco se caracteriza por sismos de baja magnitud, lo que implica que la falla podría considerarse en estado de reposo. Si se toma en cuenta la literatura publicaca, el análisis muestra que el valor "b" de la relación Gutenberg-Richter se estima en 0,90 al utilizar el método de mínimos cuadrados, lo cual podría ser compatible con una falla de cabalgamiento, como la falla de Damasco. Este valor podría ser razonable para futuras interpretaciones. Además, se ha estimado que los periodos de retorno de los grandes terremotos son muy largos por extrapolación de la relación de recurrencia establecida. La magnitud máxima del terremoto regional se ha estimado mediante el procedimiento de Kijko como estimador de máxima verosimilitud. Este procedimiento ha pronosticado que la magnitud máxima posible del terremoto es de 4,2. En consecuencia, la quiescencia sísmica, observada en la actualidad a lo largo de la falla de Damasco, y el largo período de retorno estimado implican que un gran terremoto podría estar aún muy lejos.

Palabras Clave: falla de Damasco, terremoto instrumental, relación Gutenberg-Richter y Siria.

**Corresponding author at cscientific@aec.org.sy*
[1]Dept. of Geology, the Atomic Energy Commission of Syria (AECS) P.O. Box 6091 Damascus–Syria.

Abstract

Damascus fault is a remarkable reverse tectonic structure trending through Damascus city, and may possibly represent a significant seismic hazard to the city. In that respect, the present work examines the instrumental seismic activity and establishes an earthquake catalogue covering the period 1995-2012 for this important fault, aiming to identify its contribution to the regional seismic hazard. The quantitative analysis reveals Damascus fault is characterized by low magnitude earthquakes, which implies that the fault could be considered in quiescence status. The analysis exhibits that the *b*-value of Gutenberg-Richter relationship is estimated to be 0.90 using the least-squares method, which could be compatible with a thrust faulting, such as Damascus fault, regarding the published literature. Also, this value could be reasonable for further interpretations. In addition, the return periods of large earthquakes have been estimated to be very long by extrapolation of the established recurrence relationship. Moreover, the maximum regional earthquake magnitude has been estimated by Kijko's procedure as maximum likelihood estimator. This procedure has predicted the maximum possible earthquake magnitude to be 4.2. Consequently, the seismic quiescence, observed at the present along Damascus fault, and the estimated long return period implies that a large earthquake could be still so far away.

Key words: Damascus fault, Instrumental Earthquake, Gutenberg-Richter relationship and Syria.

Introduction

Previous studies in Syria have revealed that the crustal deformation is ongoing along four tectonic zones: the Dead Sea Faults System (DSFS), the Abd-el-Aziz-Sinjar, the Euphrates Fault System, and Palmyra Fold Belt (PFB) (Barazangi *et al.*, 1993; Brew *et al.*, 2001) (Fig. 1). Numerous destructive earthquakes have occurred along these zones in the history (Sbeinati *et al.*, 2005). Damascus is the most populated city in Syria with historical and cultural importance. The city has suffered from several destructive earthquakes, such as 1759 earthquake, which caused much casualties and damage. Damascus fault, the SW ending of PFB, is a remarkable reverse tectonic structure trending through the city of Damascus, and covered by thick recent formations. In Damascus area, the model of regional kinematic predicts a crustal shortening rate across the PFB of ~2 mm a^{-1} (Abou Romieh *et al.*, 2009). This model suggests the activity of Damascus fault with significant slip rates. Furthermore, the GPS measurements estimated this rate to be about ~1.5±1.0 mm a^{-1} crossing the PFB in Damascus area (Alchalbi *et al.*, 2010). Consequently, Damascus fault could represent a significant seismic hazard to Damascus. The seismic activity of this important fault was for many years a subject of debate during many scientific meetings in Syria, such as ASST, 2004; 2009. In this context, the current research is an attempt to identify the seismic activity of this fault, to estimate its contribution to the regional seismic hazard, and evaluate threat to Damascus the megacity located within its vicinity. This issue could be interesting for the scientific society, especially because of the scarce information available about this important fault. Some preliminary results of this research reveal that Damascus fault is at the present in a quiescence state in contrast with other faults segments of the Dead Sea Faults System such as Yammounah and Aqaba segments (Fig. 1) (Abdul-wahed, 2019). The instrumental seismicity of the eastern Mediterranean region shows that the southern part of DSFS is seismically the most active (Hofstetter *et al.*, 2007; Imprescia, 2010; Imprescia *et al.*, 2012). Since the early 1980s, the Gulf of Aqaba was the most active area, where thousands of small earthquakes clusters have occurred during several months to few years (Baer *et al.*, 1999; Klinger *et al.*,

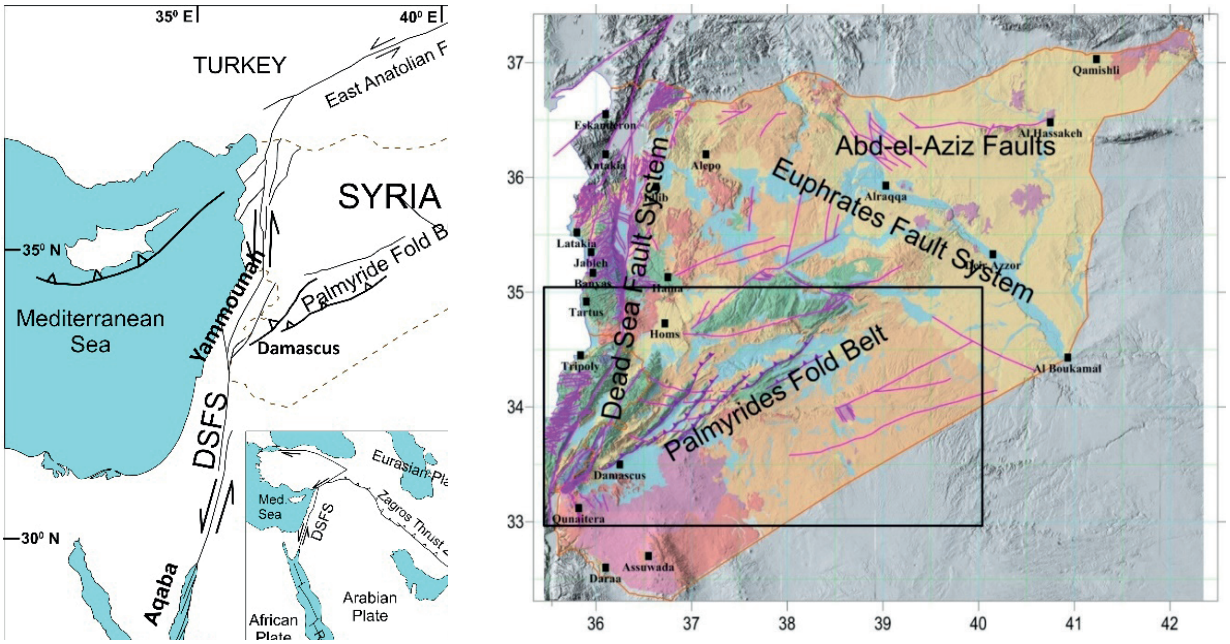

Figure 1. Regional sitting (left) and major tectonic zones in Syria (Right). The rectangle indicates the location of Figs 3 and 5 (modified from Brew *et al.*, 2001).

1999). By comparison to Abdul-wahed (2019), the current paper presents more details and results of additional procedures to identify the seismic activity of Damascus fault. Details are provided to justify determining the Gutenberg-Richter relation assuming a fixed b value. Additionally, the maximum possible magnitude M_{max} of an earthquake on the Damascus fault is calculated using Kijko's maximum likelihood method (Kijko and Sellevoll 1989; Kijko, 2004; Kijko *et al.*, 2021).

Damascus Fault

Damascus city is bounded by Qassioun mountain which extends from the South West to North East, where Paleogene (Middle Eocene) and Cretaceous (Turonian) outcrop (Fig. 2). This folded mountain, which rises ~400 m above the city, constitutes the SW ending of the PFB. The tectonic evolution of this folded mountain system started in Mesozoic period. The PFB represents a major tectonic feature in central Syria that extends SW-NE for about 400 km, from the Damascus area to the Euphrates River (Figs. 1 and 3). Damascus fault is the SW end of the PFB. It is a NW-dipping thrust fault, where the Qassioun mountain is forming its hanging wall and Damascus city is in its footwall (e.g., Sharkov *et al.*, 1994) (Fig. 4). The ~600 m thickness of Pliocene/Pleistocene alluvium in the Damascus basin, which has been dated using interbedded basalt, according to Mouty *et al.* (1992) and Sharkov *et al.* (1994) indicates that this fault has developed a throw of at least ~1000 m on an estimated timescale of 3.6 Ma (neglecting any loss of the hanging-wall escarpment to erosion). This implies a vertical slip rate of at least ~0.3 mm a^{-1} (Westaway *et al.*, 2009). Damascus fault and other reverse faults near the city of Damascus, which adjoins the southwestern trend of the PFB, have been regarded as inactive (e.g. Rukieh *et al.*, 2005). However, Abou Romieh *et al.*, (2009) suggests otherwise and its regional kinematic model proposes a rate of ~2 mm a^{-1} for the crustal shortening across the PFB. Additionally, Abou Romieh *et al.*, (2009) indicated that some historical earthquakes, which previously attributed to the DSFS in western Syria, could be occurred on the faults of PFB, and thereby these faults may possibly represent a significant seismic hazard to Damascus.

Figure 2. General view of Damascus city and Qassioun Mountain. The photo is taken from the SE direction.

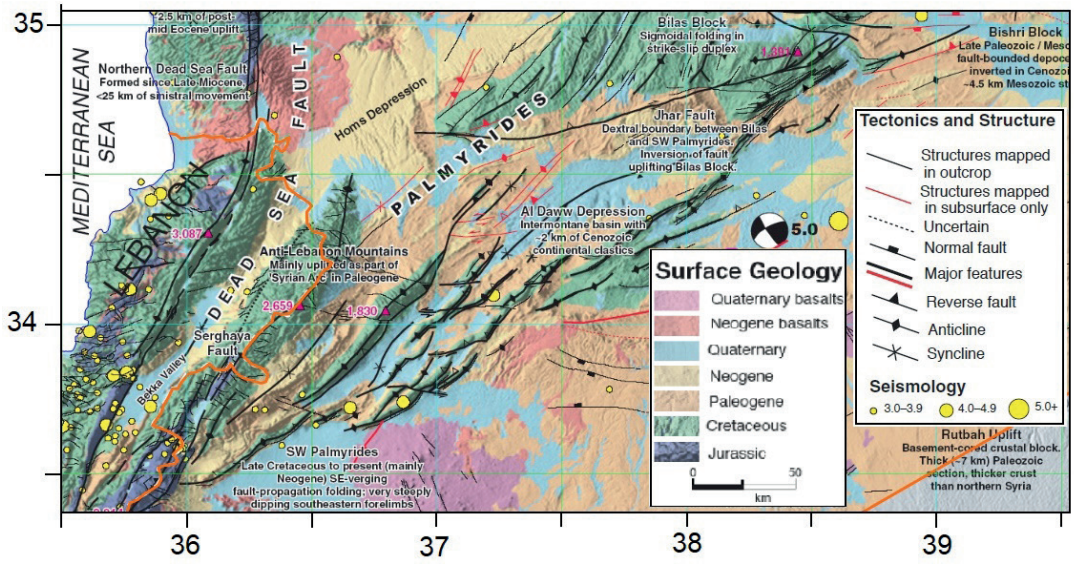

Figure 3. Seismo-tectonic and geological map of Damascus region showing the main reverse faults and structures (modified from Brew *et al.*, 2001).

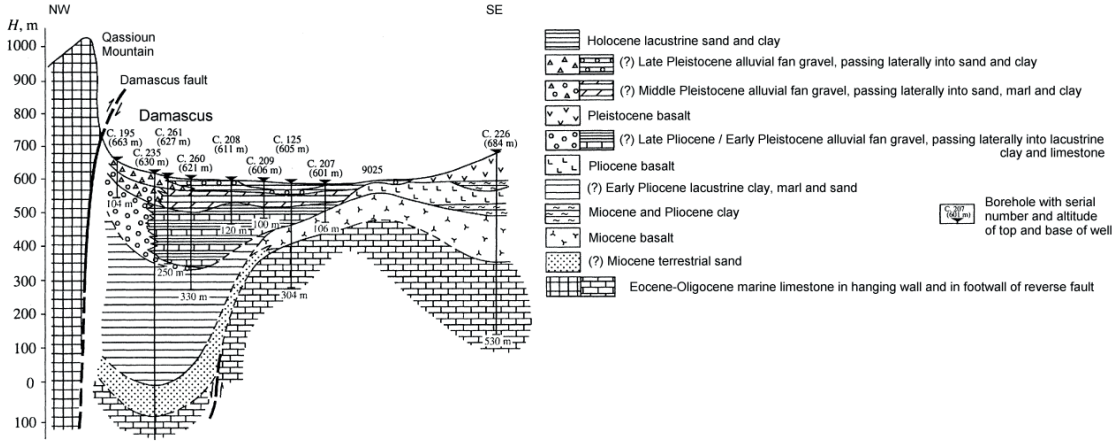

Figure 4. Simplified geological section across Damascus fault (modified from Sharkov *et al.*, 1994).

Given the age of Damascus fault to be ~0.9 Ma, and a revision of its throw to ~2500 m, considering the hanging wall erosion, (Abou Romieh *et al.*, 2012) estimated the vertical slip rates on this reverse fault of ~2.8 mm a^{-1}. Abou Romieh *et al.* (2012) has explained the low slip rate, recently measured on the northern DSFS in western Syria, by absorbance of the northward motion of the Arabian plate, relative to the African plate, by crustal shortening within the PFB. A soil-gas radon survey has been performed across the expected westward ending of Damascus fault, in order to trace the location of the concerned fault where it is covered by unconsolidated formations (Al-Hilal and Abdul-wahed, 2016). The relative abnormal radon values, (2-3 times higher than the background level), has been found to vary in accordance with the expected orientation of the buried fault axis in the bedrock.

Regional Seismicity

Syria has suffered from many large historical earthquakes (Sbeinati *et al.*, 2005). However, the present instrumental seismic activity is passing in quiescent status, which is supported by the low-level magnitude of recorded events during the period 1995-2012 (Abdul-Wahed and Al-Tahan, 2010; Abdul-Wahed *et al.*, 2011; Abdul-Wahed and Asfahani, 2018). The Syrian National Seismological Network (SNSN), operated since 1995, allows recording about 1600 local events during the period (1995-2012) along and around Damascus fault (Fig. 5). These events have been located with errors less than 10 km (Abdul-Wahed and Asfahani, 2018). A noteworthy seismic activity has been observed along the north-eastern of Damascus fault, thus, the South West Palmyra Fold Belt (SWPFB) can be considered as a potential seismic source area. In the SWPFB, 3 seismic swarms of events were observed in 2004 in the west of Jayrud town. The first swarm occurred on 8 February 2004 including 6 events. The second occurred in the same site on 16 and 17 May 2004 including 22 events. Although these events were of low magnitude (Mc=2.6-3.3), they were widely felt in the region of Ma'alula. The third swarm, including 8 events, occurred on 7 June 2004, where the strongest event attends the

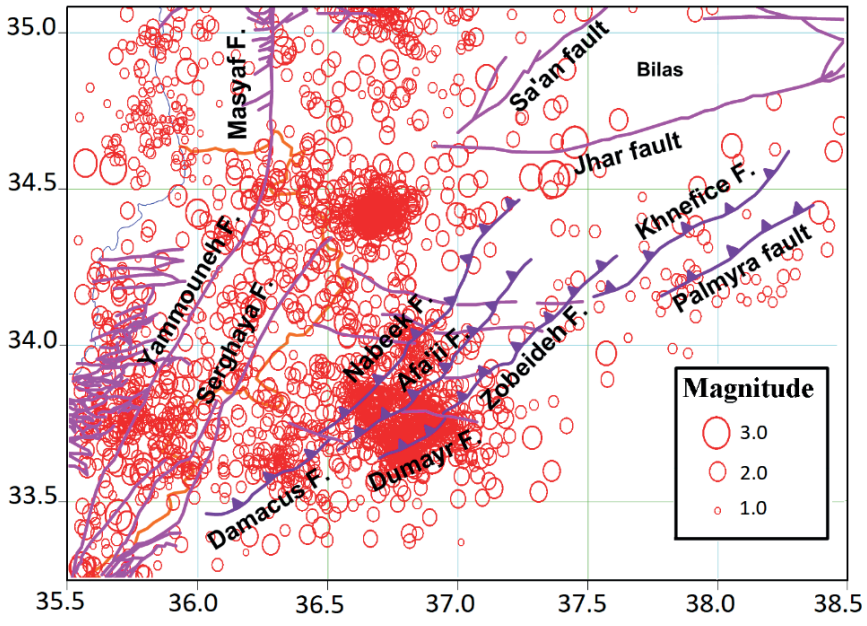

Figure 5. Epicenters map showing the instrumental seismic activity recorded in Damascus region during the period 1995-2012 (F.: fault).

magnitude of 3.7. Another swarm of 8 events was observed on 21 April 2011 in Jayrud region. These swarms can be related to SWPFB reverse faults such as the extension of Damascus fault.

Data and Methods

Special catalogue of earthquakes for Damascus fault covering the period from 1995 to 2012 has been compiled by using essentially the data of the published SNSN bulletins. A total of 1600 earthquake events have been recorded in Damascus region. About 1007 events, that occurred within 25 km around SWPFB during the period of 17 years, are included in this catalogue. The annual average of the recorded events is about 60 events, which could be considered very low in comparing with other parts of DSFS, such as Yammounah or Aqaba Gulf, which consequently indicates that SWPFB is actually passing with a relative quiescence. For comparison, 2414 events were recorded in Aqaba Gulf in 1995 (Jordan Seismological Observatory, 1995) and 948 events in 1997 (Jordan Seismological Observatory, 1997).

Magnitudes are calculated from the coda wave duration via the following formula (SNSN bulletins, 1995-2012):

$$M_C = -3.0 + 2.6 * \log(T) + 0.001 * D \quad (1)$$

Where M_C is the coda magnitude, D is the epicentral distance (in km) and T is the coda duration (in sec). Most of these events are micro-earthquakes (M_C<3.0) and their magnitude varies between 1.0 and 3.7, where the average magnitude is approximately 1.6 (Fig. 6). The largest observed earthquake magnitude in the area is 3.7. A quantitative idea about the seismic activity produced by a fault could be obtained by examining the frequency-magnitude distribution and adopting the empirical relation of Gutenberg and Richter (G-R relation) (Gutenberg and Richter, 1944; 1954). This empirical relation is extensively used in the studies of active faults and their earthquake activity. The G-R relation is given as:

$$\log N = a - bM \quad (2)$$

In this relation, N is the number of events with magnitude larger or equal to M, and a and b are empirical constants, where a-value indicates the level of seismic activity and b-value is the slope of G-R relation and indicates the rate of occurrence within a given magnitude range. "b-value" describes the relative abundance of large to small earthquakes. G-R relation could be applied to cumulative number "N" as well as to incremental numbers "n". In the first case, N is the cumulative number of earthquakes with magnitude larger than M. However, n is the number of events within an interval of magnitudes: $M \pm \Delta M$ in the second case, where ΔM should be carefully chosen for any incremental b-value evaluation. The magnitude data are usually discrete quantities and calculated with a precision of 0.1 magnitude unit in approximately all global catalogs. Thus, a proper choice of ΔM will be a compromise between the magnitude sampling as close to 0.1 as possible and statistically large numbers of events in each magnitude group. Further, the cumulative distribution of magnitudes is preferable; it provides better linear fit since large numbers are less degraded by statistics of small numbers.

Results and Discussion

The empirical G-R relation has been evaluated using Seisan software (Seisan 10.3, 2015; Havskov

and Ottemoller, 2020). The empirical constants of G-R relation, *a*-value and *b*-value, are evaluated from the available recorded events using two techniques: the least square and supposing a fixed *b*-value, and two incremental distributions of magnitudes (ΔM): 0.1 and 0.5. Since some authors, such as Wesnousky (1999) and Kagan (1999), urge that *b*-value must be fixed to 1 as a universal constant for earthquakes; the *b*-value has been fixed to 1 in the second technique. However, other authors (e.g., Frohlich and Davis, 1993; Schorlemmer *et al.* 2005; Madahizadeh *et al.* 2016) reveal that *b*-value is systematically affected by different styles of faulting. Figure 7 shows the obtained forms of G-R relation; also, the results are shown in table 1, where *SD* is the standard deviation of estimator, *COR* is the regression coefficient, and *RMS* is the root-mean-square error of estimate. The obtained results show *b*-value to be 0.93 and 0.90 according to 0.1 and 0.5 incremental distributions of magnitudes, respectively. According to the published literature (e.g., Frohlich and Davis, 1993), the *b*-value commonly ranges from 0.60 to 1.30 depending on the different tectonic regimes. Schorlemmer *et al.* 2005 found the thrust zones are associated with small *b*-value (≈0.90), which corresponds to Damascus fault and indicates that the calculated *b*-value is compatible. Therefore, this *b*-value can be accepted regarding the reported values in the literature and valid for further interpretations. The low standard deviation (*SD* = 0.12), the high regression coefficient (*Cor*=0.99), and the very low residual (*RMS*=0.09) indicate that the return periods can be calculated by extrapolating the obtained G-R relation to larger earthquakes. The return periods for higher magnitude events than those included in the catalogue are deduced by extrapolating of curves fit to the log-linear distribution. The extrapolated return periods are shown in Fig. 8. A return period for an event of magnitude 7.0 is extrapolated to be 2860 years according to the least square method and 0.5 incremental distributions of magnitudes, which can be qualified as very long return period.

Table 1. *a*-value and *b*-value calculated by using two techniques and two steps of magnitudes.

Technique	**ΔMc**	***a*-value**	***b*-value**	**accuracy**	
Least-squares	0.1	4.17	0.93	*COR*=0.99	*RMS*=0.09
Least-squares	0.5	4.07	0.90	*COR*=0.99	*RMS*=0.09
Fixed b	0.1	4.33	1.0	*SD*=0.12	
Fixed b	0.5	4.29	1.0	*SD*=0.15	

The fitting of G-R relation to the observed frequency-magnitude distribution has shown a magnitude completeness down to $M_{completeness}$ =1.5 (Fig. 6). This indicates that not all micro-earthquakes (Mc<1.5) have been detected by the SNSN. Some too small events were not recorded on a sufficiently large number of stations to trigger the recording system in the SNSN and to initiate the location procedure, thus these events have not been reported. It might also that the network operators decided that some micro-earthquakes below a certain threshold (Mc<1.5) are not of interest.

The earthquake catalogue, established in this research for the period of 1995-2012, could be considered as incomplete because the magnitude of the biggest recorded event does not exceed 3.7. Therefore, it was essential to look for an appropriate interpretative procedure to process such an incomplete catalogue. Referring to the related literature, Kijko's procedure (Kijko, 1983) seems to be an adequate technique for processing such catalogue. This procedure (Kijko and Sellevoll 1989; Kijko,

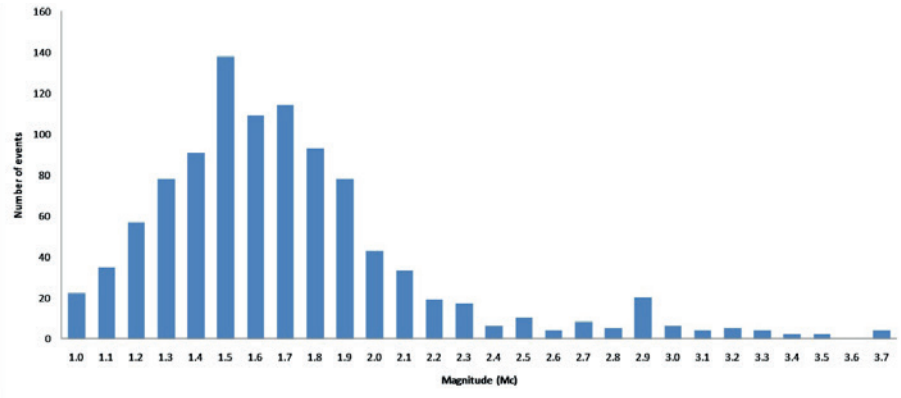

Figure 6. Distribution of the recorded events according to their magnitudes during the period of 1995-2012. The incremental distribution (ΔM) is 0.1.

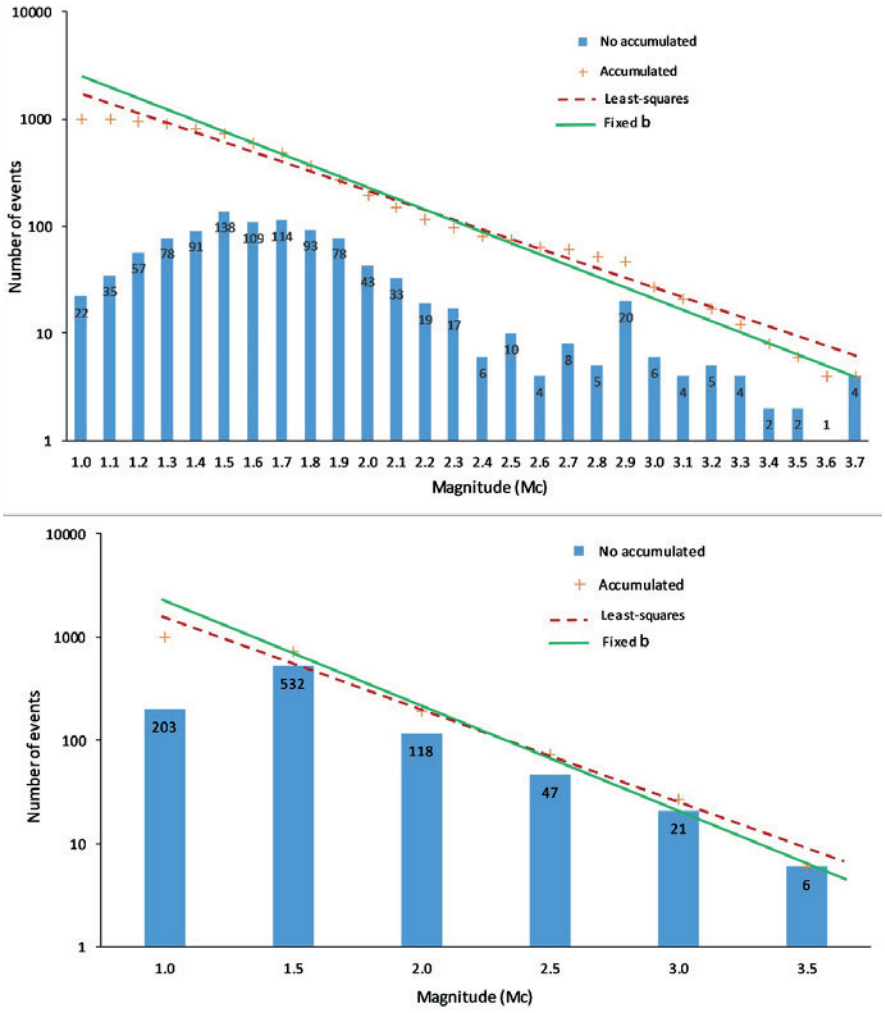

Figure 7. Comparison between the two techniques: least-squares in dashed line and fixed b in continuous line, using two magnitude intervals: ΔM=0.1 in the top and ΔM=0.5 in the bottom. Histograms are showing the number of events in selected magnitude intervals and crosses are showing the accumulated number of events.

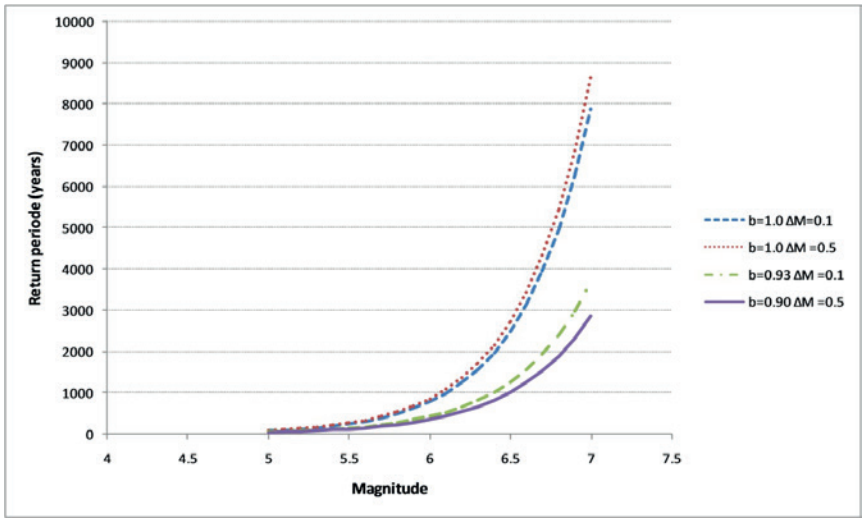

Figure 8. Predicted return periods by the two techniques using two magnitude intervals (ΔM).

2004; Kijko *et al.*, 2021) is based on the estimation of maximum likelihood of the seismic activity rate (λ), *b*-value in the G-R relation, and the maximum possible magnitude M_{max}. It is applicable in the extreme case when no information about the nature of the earthquake magnitude distribution is available. The procedure can also be used in the case of an incomplete earthquake catalogue, which is the case of the earthquake catalogue for Damascus fault.

The Kijko's procedure has been applied in this research on the instrumental earthquake catalogue of the Damascus fault using the Fortran code: hn2.exe: Release: 2.10, 24 June 2005. (The code availability is on request from his author Andrzej Kijko, University of Pretoria, Pretoria, South Africa, andrzej.kijko@up.ac.za). The obtained results are:

$\beta = 2.75 \pm 0.06$ (*b*-value = 1.19 ± 0.03, where β=*b*-value*ln(10))

$\lambda = 234.15 \pm 8.65$

$M_{max} = 4.20 \pm 0.71$

The Kijko's procedure predicts the maximum possible earthquake magnitude (M_{max}) to be 4.2 and expects a return period (λ) of 234 years for this earthquake. Furthermore, this procedure estimates the probabilities of occurrence of large earthquakes within a given interval of time. Figure 9 shows the probabilities of occurrence of earthquakes during the time intervals 1, 50, 100 and 1000 years. The magnitude of the strongest earthquake in these time intervals could attain 2.5, 4.2, 4.5 and 5.3, respectively.

Conclusions

The established catalogue for Damascus fault, covering the period 1995-2012, reveals the earthquake activity produces low magnitude events and passes through a relative status of quiescence in contrast with other adjacent faults segments of DSFS. The empirical G-R relation shows a *b*-value of 0.90 according to the least square technique, which could be compatible with a thrust faulting, such as Damascus fault, regarding the published literature. Also, this value could be reasonable for further

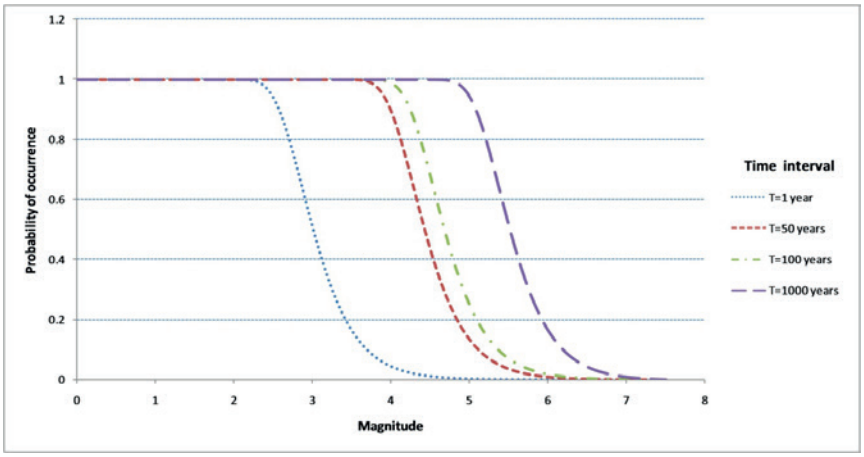

Figure 9. Probabilities of occurrence of earthquakes during the time intervals 1, 50, 100 and 1000 years..

interpretations. Extrapolation of this relation reveals very long return periods of large earthquakes. The seismic hazard parameters, maximum possible magnitude Mmax, earthquake activity rate λ, and the Gutenberg-Richter *b*-value, have been estimated using the maximum likelihood Kijko's procedure. The Kijko's procedure has predicted the maximum possible magnitude to be 4.2. The seismic quiescence, observed along Damascus fault, and the very long return period implies that a large earthquake is still unlikely. This result needs to be confirmed by additional evidences such as palaeoseismological investigation. Some trenches across the Damascus fault could provide reliable information about the slip rate for this fault and its past seismic activity. Based on possible palaeoseismological evidence, it is suggested to evaluate the recurrence interval for surface faulting events.

Acknowledgements

Author would like to thank Prof. Dr. I. Othman, the general director of the Atomic Energy Commission for his support of this research.

References

Abdul-Wahed M. K. and Al-Tahan I., 2010, Preliminary outlining of the seismological active zones in Syria. *Annals of geophysics*, 53 (4), 1-9. http://dx.doi.org/10.4401/ag-4683.

Abdul-Wahed M. K., Asfahani J., Al-Tahan I., 2011, A combined methodology of multiplet and composite focal mechanism techniques for the identification of the seismological active zones in Syria. *Acta Geophysica*, 59 (5), 967-992. http://dx.doi.org/10.2478/s11600-011-0024-2.

Abdul-Wahed M. K., and Asfahani J., 2018, The recent instrumental seismicity of Syria and its implications. *Geofísica Internacional*, 57-2: 121-138. http://dx.doi.org/10.22201/igeof.00167169p.2018.57.2.1655.

Abdul-wahed M. K., 2019, Recent Instrumental Earthquake Activity Along the Damascus Fault (Syria). N. Sundararajan *et al.* (eds.), On Significant Applications of Geophysical Methods, Advances in Science, Technology and Innovation, https://doi.org/10.1007/978-3-030-01656-2_41.

Abou Romieh M., Westaway R., Daoud M., Radwan Y., Yassminh R., Khalil A., AlAshkar A., Loughlin S., Arrell K., Bridgland D., 2009, Active crustal shortening in NE Syria revealed by deformed terraces of the River Euphrates. *Terra Nova*, 21, 427–437.

Abou Romieh M., Westaway R., Daoud M., Bridgland D. R., 2012, First indications of high slip rates on active reverse faults NW of Damascus, Syria, from observations of deformed Quaternary sediments: implications for the partitioning of crustal deformation in the Middle Eastern region. *Tectonophysics*, 538–540, 86–104.

Alchalbi A., Daoud M., Gomez F., McClusky S., Reilinger R., Romeyeh M. A., Alsouod A., Yassminh R., Ballani B., Darawcheh R., 2010, Crustal deformation in northwestern Arabia from GPS measurements in Syria: slow slip rate along the northern Dead Sea Fault. *Geophys. J. Int.*, 180, 125–135.

Al-Hilal M., and Abdul-Wahed M. K., 2016, Tectonic and geologic influences on soil gas radon emission along the western extension of Damascus fault, Syria. *Environmental Earth Sciences*, 75(23):1-11. https://doi.org/10.1007/s12665-016-6292-z.

ASST, 2004, Workshop on "Earthquake Hazard Assessment in Syria and Lebanon: Progress, Results and Future strategies', 7 – 9 September 2004, The Arab School for Science and Technology (ASST), Damascus, Syria.

ASST, 2009, Workshop on "Active Tectonic Studies and Earthquake Hazard Assessment in Syria and Neighboring Countries', 17 – 19 November 2009, The Arab School for Science and Technology (ASST), Damascus, Syria.

Baer G., Sandwell D., Williams S., Bock Y., Shamir G., 1999, Coseismic deformation associated with the November 1995, Mw=7.1 Nuweiba earthquake, Gulf of Elat (Aqaba), detected by synthetic aperture radar interferometry. *J. Geophys. Res.*, 104, 25221– 25232.

Barazangi M., Seber D., Chaimov T., Best J. and Sawaf T., 1993, Tectonic evolution of the northern Arabian plate in western Syria. In, E. Boschi, E. Mantovani and A. Morelli (Eds.), Recent Evolution and Seismicity of the Mediterranean Region. Kluwer Academic Publishers, 117–140.

Brew G., Barazangi M., Al-Maleh A. K., Sawaf T., 2001, Tectonic and geologic evolution of Syria, *GeoArabia*, Vol. 6, PP 573-616.

Frohlich C., and Davis S., 1993, Teleseismic b values: or, much ado about 1.0, *J. Geophys. Res.*, 98, B1, 631-644, https://doi.org/10.1029/92JB01891.

Gutenberg B., and Richter C.F., 1944, Frequency of earthquakes in California, *Bull. Seismol. Soc. Am.*, 34, 4, 185-188.

Gutenberg B., and Richter C.F., 1954, Seismicity of the Earth and Related Phenomena, Princeton University Press.

Havskov, J., Voss, P.H. and Ottemoller, L., 2020, Seismological Observatory Software: 30 Yr of SEISAN. Seismological Research Letters, 91 (3): 1846-1852. https://doi.org/10.1785/0220190313.

Hofstetter R., Klinger Y., Amrat A. Q., Rivera L. and Dorbath L., 2007, Stress tensor and focal mechanisms along the Dead Sea fault and related structural elements based on seismological data. *Tectonophysics*, 429, 165-181, https://doi.org/10.1016/j.tecto.2006.03.010.

Imprescia P., 2010, Meccanismi focali di terremoti come strumento per la definizione della sismotettonica dell'area mediterranea. *Ph.D. thesis*, University of Catania.

Imprescia P., Palano Mimmo, Gresta Stefano, 2012, Mapping crustal strain and stress fields across the Dead Sea Fault System by GPS observations and focal plane solutions. Conference paper: GNGTS November 2012, Volume: Extended Abstract.

Jordan Seismological Observatory, 1995, Earthquakes in Jordan and adjacent areas, Nat. Res. Auth., *Jordan Seis. Obs., Bul.,* No. 27.

Jordan Seismological Observatory, 1997, Earthquakes in Jordan and adjacent areas, Nat. Res. Auth., *Jordan Seis. Obs., Bul.,* No. 29.

Kagan Y., 1999, The universality of the frequency-magnitude relationship. *Pure and Appl. Geophys.,* 155: 537-574.

Kijko A., 1983, A modified form of the first Gumbel distribution: model for the occurrence of large earthquakes, Part II: Estimation of parameters, *Acta Geophys.,* 31, 27-39.

Kijko A. and Sellevoll M. A., 1989, Estimation of earthquake hazard parameters from incomplete data files, Part I, Utilization of extreme and complete catalogues with different threshold magnitudes. *Bull. Seism. Soc. Am.*, 79, 645-654.

Kijko, A., Vermeulen, P.J. and Smit, 2021, A. Estimation Techniques for Seismic Recurrence Parameters for Incomplete Catalogues. *Surv. Geophys.* (2021). https://doi.org/10.1007/s10712-021-09672-2.

Kijko A., 2004, Estimation of the Maximum Earthquake Magnitude, mmax. *Pure appl. geophys.*, 161, 1655-1681. https://doi.org/10.1007/s00024-004-2531-4.

Klinger Y., Rivera L., Haessler H., Maurin J.C., 1999, Active faulting in the Gulf of Aqaba: new knowledge from the Mw7.3 earthquake of 22 November 1995. *Bull. Seismol. Soc. Am.*, 89, 1025– 1036.

Madahizadeh R., Mostafazadeh M. and Ashkpour-Motlagh S., 2016, Earthquake Potential in the Zagros Region, Iran. *Acta Geophys.*, 64, 1462–1494. https://doi.org/10.1515/acgeo-2016-0080.

Mouty M., Delaloye M., Fontigni, D., Piskin O., Wagner J.-J., 1992, The volcanic activity in Syria and Lebanon between Jurassic and Actual. *Schweizerische Mineralogische und Petrographische Mitteilungen*, 72, 91-105.

Rukieh M., Trifonov V. G., Dodonov A. E., Minini H., Ammar O., Ivanova T. P., Zaza T., Yusef A., al-Shara M., Jobaili Y., 2005, Neotectonic map of Syria and some aspects of Late Cenozoic evolution of the northwestern boundary zone of the Arabian plate. *Journal of Geodynamics*, 40, 235-256.

Sbeinati M. R., Darawcheh R., Mouty M., 2005, The historical earthquakes of Syria: an analysis of large and moderate earthquakes from 1365 B.C. to 1900 A.D.. *Ann. Geofis.*, 48 (3), 347-435.

Schorlemmer D., Wiemer S., and Wyss M., 2005, Variations in earthquake size distribution across different stress regimes. *Nature*, 437, 7058, 539-542. https://doi.org/10.1038/nature04094.

SEISAN: The earthquake analysis software, Version 10.3, Jens Havskov and Lars Ottemöller, Department of Earth Science, University of Bergen, Allégaten 41, 5007 Bergen, Norway, 2015. ftp://ftp.geo.uib.no/pub/seismo/SOFTWARE/.

Sharkov E.V., Chernyshev I. V., Devyatkin E. V., Dodonov A. E., Ivanenko V. V., Karpenko M. I., Leonov Yu. G., Novikov V. M., Hanna S., and K. Khatib, 1994, Geochronology of Late Cenozoic basalts in western Syria. *Petrology*, 2,4, 385–394.

SNSN Bulletins,1995, SNSN: Syrian National Seismological Network, General Establishment of Geology and Mineral Resources, Syria. (1995-2012).

Wesnousky S.G., 1999, Crustal Deformation Processes and the Stability of the Gutenberg-Richter Relationship. *Bulletin of the Seismological Society of America*, 89, 4, 1131-1137.

Westaway R., Bridgland D., Sinha R., Demir T., 2009, Flubvial sequences as evidence for landscape and climatic evolution in the Late Cenozoic; a synthesis of data from IGCP 518. *Global and Planetary Chang*, 68, 237–253.

Original paper

https://doi.org/10.22201/igeof.00167169p.2022.61.2.2197

Assessment of the Tectonic Effects on Soil Radon Activity Along the Margin of the Arabian Plate Boundary in Northwestern Syria

Mohamed Al-Hilal[1*]

Received: November 1, 2021; accepted: March 27, 2022; published on-line: April 1, 2022.

Resumen

El objetivo principal del presente estudio es evaluar el papel de la tectónica activa en el nivel de emanación de radón del suelo en dos estructuras tectónicamente activas de la Falla del Mar Muerto del Norte (NDSF, por sus siglas en inglés, al noroeste de Siria, es decir, los segmentos de falla Qastoon y Al-Harif. Las mediciones de radón se basaro básicamente en los resultados extraídos de estudios arqueosísmicos y paleosísmicos anteriores en Al-Harif, además del estudio geofísico y morfotectónico integrado en el sitio de Qastoon. Se realizaron un total de 80 mediciones de gas radón en el suelo, a una profundidad de muestreo de 75 cm; se utilizó el detector de radón AlphaGUARD PQ 2000Pro. El rango de fondo de la emisión normal de radón del suelo local se determinó en un área ubicada lejos de la influencia de las perturbaciones tectónicas. Los datos de radón obtenidos se analizaron estadísticamente y los valores medios se estandarizaron en términos de probabilidad de magnitud, lo ciual mejora el proceso de comparación y facilita la separación de las variaciones normales del radón de otros valores anómalos o relacionados con la geotectónica. Los resultados generales revelaron ocurrencias notables de anomalías de radón asociadas con fallas con valores pico máximos de ~6 a 7 veces por encima del fondo, con una tendencia de acuerdo con los rastros previstos de rupturas de fallas en Qastoon y Al-Harif, respectivamente.

Palabras Clave: gas radón, estructuras tectónicas activas, falla norte del Mar Muerto y oeste de Siria.

**Corresponding author at cscientific@aec.org.sy*
[1]Dept. of Geology, the Atomic Energy Commission of Syria (AECS) P.O. Box 6091 Damascus–Syria.

Abstract

The main purpose of the present study is to assess the role of active tectonics on soil radon emanation level across two tectonically active structures of the Northern Dead Sea Fault (NDSF) northwestern Syria: namely, the Qastoon and the Al-Harif fault segments. Radon measurements were basically directed by the results drawn from earlier archaeoseismic and paleoseismic studies in Al-Harif, besides integrated geophysical and morphotectonic survey at the Qastoon site. A total of 80 soil radon gas measurements were performed at 75 cm sampling depth, using AlphaGUARD PQ 2000Pro radon detector. The background range of normal radon emission from local soil was determined in an area located far from the influence of the tectonic disturbances. The obtained radon data were statistically analyzed and the mean values were standardized in terms of magnitude probability which enhances the comparison process facilitating the separation of normal radon variations from other anomalous or geotectonic related values. The overall results revealed remarkable occurrences of fault-associated radon anomalies with maximum peak values of ~6 to 7 times above the background, trending in accordance with the predicted traces of the fault ruptures at the Qastoon and Al-Harif, respectively.

Key words: Radon gas, Active tectonic structures, Northern Dead Sea Fault, western Syria.

Introduction

The Northern Dead Sea Fault (NDSF) is widely recognized as an active tectonic structure in the eastern Mediterranean region evidenced by many large historical earthquakes (Ambraseys and Barazangi, 1989; Ambraseys and Jackson, 1998; Sbeinati *et al.*, 2005). The fault forms a major continental transform plate boundary between the Arabian plate to the east and the African plate to the west, and it accommodates their differential shift. Thus, the system has become the focus of attention for many researchers who studied its seismotectonic and geologic evolution (Barazangi *et al.*, 1993; Butler *et al.*, 1997; Brew *et al.*, 2001; Meghraui, 2015). Although the NDSF is marked by a rich historical catalogue of large earthquakes, it currently shows an apparent lack of seismicity with a prevailing status of quiescence. Moreover, analysis of recent seismic data revealed that the earthquake activity along most segments of the NDSF in western Syria is presently distinguished by producing a little number of low magnitude seismic events (Al-Hilal and Abdul-Wahed, 2018). Furthermore, Meghraoui *et al.* (2003) found evidences for ~830 years of seismic quiescence along the NDSF at Al-Harif site of Missyaf fault segment. Additionally, recent Global Positioning System (GPS) measurements along the plate boundary in NW Syria showed a fairly small relative motion between the Arabian and African plates with average geodetic velocities of ~0.6 mm/year (Alchalbi *et al.*, 2010). However, these results seem to be inconsistent with the long historical record and the consequences of field observations that bear out the activity and seismogenic potential of the concerned fault system. Thus, even though the concerned region seems nowadays to pass through a period of seismic quiescence, this temporal status is interpreted by most seismologists as a probable reflection of the slow rate of strain accumulation in a locked fault system (e.g. Alchalbi *et al.*, 2010; Kobeissi *et al.*, 2015).

From tectonic point of view, faults are described as complex structures that are generated under the actions of high stresses coupled with accumulated strains which commonly result in significant crustal deformations with massive zones of crushed and broken rocks. Hence, faults often exhibit higher permeability environment compared to the surrounding unaltered rocks. This property may turn most faulted zones into favored paths for upward migration of emanated soil gases during their

way to the Earth's surface. Among these gases, radon, a natural radioactive element constantly generated from soil and rocks is emitted to the atmosphere, particularly through weak zones such as faults (Al-Hilal and Abdul-Wahed, 2016; Mojzes Andrej *et al.*, 2017). Radon (^{222}Rn, with a half-life of 3.825 days) is a progeny nuclide of radium (^{226}Ra), which in turn is generated from the natural decay series of uranium (^{238}U). The gaseous, radioactive and inert nature of radon makes it a significant tracer which can be used to investigate some crustal activities that induce gas emission in the ground (King *et al.*, 1996; Richon *et al.*, 2010).

Radon is commonly transported within the earth's crust by two basic mechanisms, diffusion and/or convection of the gas flow (Tanner, 1964; Etiope and Martinelli, 2002). However, there are some important factors which could facilitate the migration process of radon and enhance the distance reached in the ground. Among these factors is the groundwater flow which plays a major role as driver of radon transport through permeable geologic medium, and could be brought upwards to the surface by a rising flux of some other natural gases, (e.g. CO2 and He) which act as radon carriers via fractures and rupture zones. Accordingly, the primary goal of this work is to investigate the effects of tectonic activity on soil radon emanations across two active fault structures - the Qastoon and Al-Harif segments that are located along the NDSF in northwestern Syria.

The Study Area

The Qastoon and the Al-Harif faults represent prominent structural components of the NDSF in western Syria (Fig. 1). The Qastoon segment is located at the eastern boundary of the Ghab basin, at latitude of (35°.41'.30N) and longitude of (36°.24'.05E). The geological setting of the fault zone and its surroundings is characterized by thick Pliocene lacustrine sediments consisting of calcareous marls, silt, pebbles and clays alternating with repetitive sequences of sandstones and well cemented conglomerate beds at depth. The site is bordered from the north and the east by notable outcrops of Pliocene basalts along with massive deposits of chalky/clayey limestone which belong to the Middle and Upper Eocene (Devyatkin *et al.*, 1997). On the other hand, the north trending Al Harif fault segment is situated along the eastern flank of the Syrian Coastal Mountains Range, about 4 km north of the Missyaf city, at latitude of (35°.06'.01N) and longitude of (36°.20'.05E). The fault interacts with geologically young formations of late Pleistocene and Holocene that are composed mainly of alluvial deposits, sandy loams, clays, flood plains, coarse and fine gravels in a sandy matrix (Ponikarov, 1966).

Tectonically, the left-lateral NDSF forms a key tectonic feature in western Syria that stretches over a distance of about 150 km in parallel to the Syrian Coastal Mountains Range (Brew *et al.*, 2001). Along this distance, two major fault structures were considered important for the purpose of this study; the Qastoon and the Al Harif segments (Fig. 2). Field investigations in the study region revealed some significant geomorphic and topographic expressions which attest to the ongoing tectonic activities of the concerned fault zone. Evidences include the occurrence of recent lava flows; break in slope features; faulted young alluvial fans and the common occurrence of distinct deflected streams which indicates the role of tectonic activity in influencing the outline of drainage system (Meghraui, 2015). Besides, the formations of distinguished colluvial wedges which are commonly associated with recurrent ruptures of fault where each fault rupture creates a scarp with a sharp free face. Then, sediments that eroded from the free face is shed across the fault and filling up on the footwall of the fault due to slope failure as a result of erosion and re-deposition during successive dip

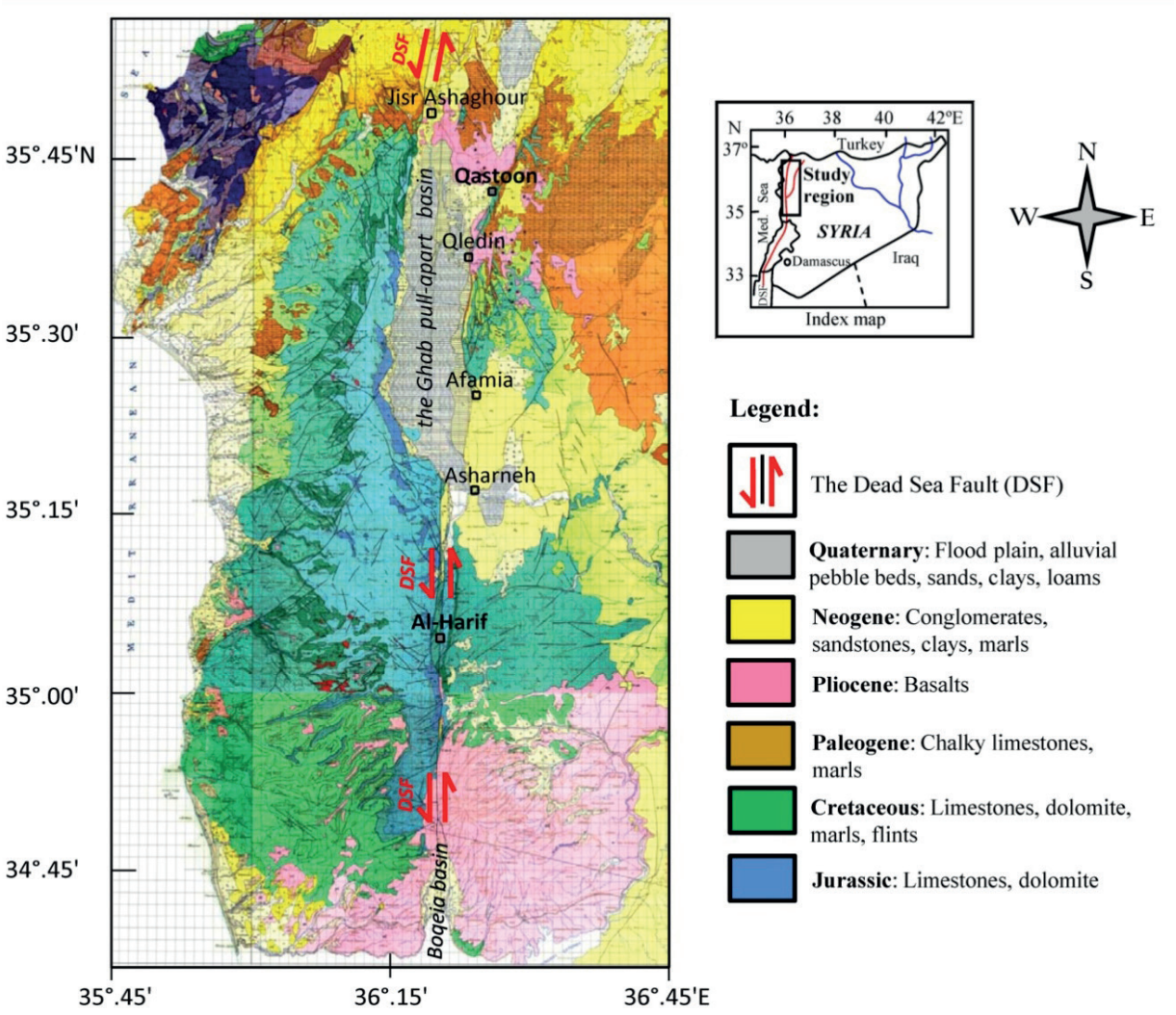

Figure 1. Geological map of western Syria showing the locations of the radon measurement sites at the Qastoon and the Al Harif faults.

slip of faulting, producing a colluvial wedge (Fig. 3). In our case, the observed colluvial wedges along the eastern Ghab fault were developed mostly due to tectonically induced gravity landslide of Pliocene-Quaternary unconsolidated sediments that are eroded from the free face of the fault scarp and accumulated at the footwall of the fault plane, producing a typical colluvial wedge, as shown in Fig. 3a, b and c. Accordingly, the interpretation of colluvial wedge stratigraphy and development may assist paleoseismologists to decode an 'event-stratigraphy' of past earthquakes (McCalpin, 2009).

From seismic point of view, the NDSF in western Syria and southern Turkey has been the site of several strong earthquakes (Ms~7.0) that occurred during the last millennium (Ambraseys and Jackson, 1998; Sbeinati *et al.*, 2005; Akyuz *et al.*, 2006). The return period of large earthquakes in Syria was estimated to be about 200-350 years (Ambraseys and Barazangi, 1989). However, new evidences from palaeoseismology, archaeoseismology and historical seismicity along the NDSF in Syria revealed a seismic gap of ~830 years along the Missyaf fault segment (Megrhaoui *et al.*, 2003). Although such temporal seismic quiescence may imply that the fault has been seismically inactive in

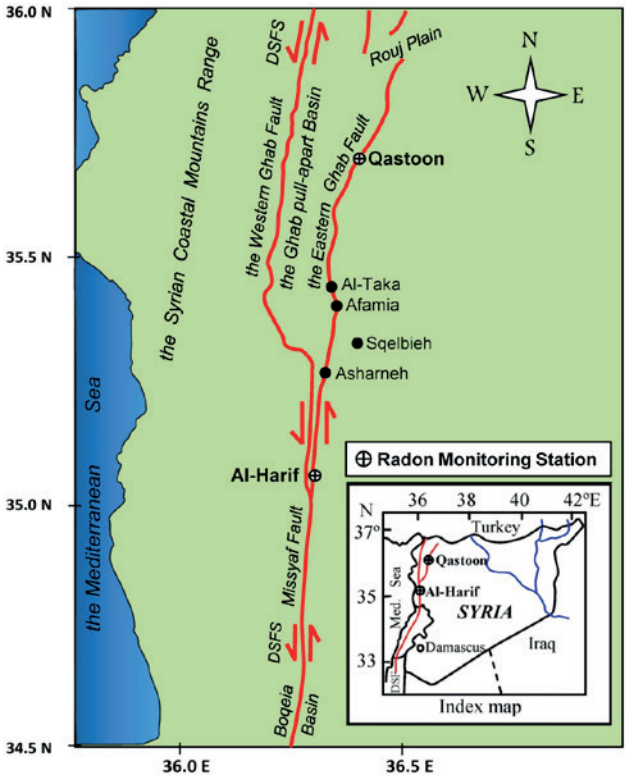

Figure 2.Tectonic map of western Syria showing the general trend of the northern Dead Sea Fault System (DSFS), including the Missyaf, Al-Harif, Qastoon and the Ghab faults.

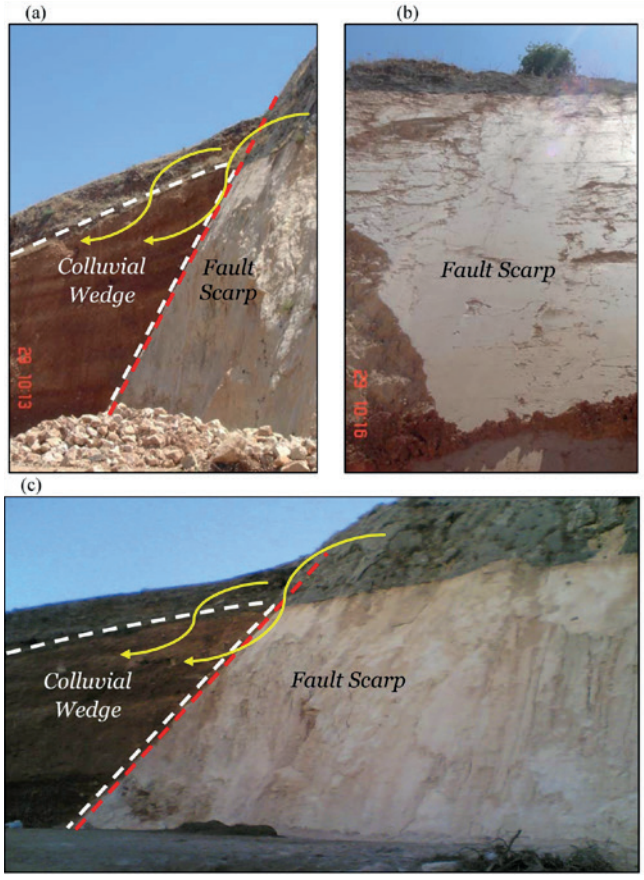

Figure 3.Field Photographs illustrating the development of typical colluvial wedges that formed along the eastern bounding fault of the Ghab pull-apart basin. The dashed red and white lines delineate the fault plane and the colluvial wedge, respectively.

the last few centuries, it might be a sign of high level of seismic hazard in the region due to a probable slow rate of interseismic strain accumulation in a locked fault (Alchalbi *et al.*, 2010). However, analysis of seismic data in Syria during the period (1995-2012) revealed that the earthquake activities in the country produce a little number of low magnitude events (Al-Hilal and Abdul-Wahed, 2018). However, Barazangi *et al.* (1993) concluded that the apparent lack of recent seismicity along the NDSF should not be interpreted as minimizing the potential hazard and risk in the region. Thus, realizing the active crustal deformation, particularly in terms of strain accumulation in the fault, and the average timing for the recurrence interval of large earthquake, are essential issues for seismic hazard assessment in the region.

Radon Measurements

A total of eighty soil gas radon measurements carried out across the Qastoon and the Al-Harif faults, which represent two remarkable tectonic segments located along the northwestern margin of the Arabian plate in Syria (Figs. 4 & 5). The selection of these two structures for radon measurements was based on the results drawn from previous extensive field works which revealed clear evidences of current active tectonics associated with the structural evolution of the NDSF. Accordingly, the radon measurements in the Al-Harif site were oriented in the light of evidences obtained from earlier results of archaeoseismic, palaeoseismic and historical seismicity carried out in the same area (Meghraoui *et al.*, 2003). Similarly, the radon investigations at the Qastoon site were mainly guided by the outcome of previous geophysical surveys and morphotectonic mapping performed in the region by Asfahani *et al.* (2010). The ultimate conclusions of these studies attested to the ongoing tectonic activity and seismogenic potential in both the Qastoon and Al-Harif zones. In view of that, radon surveys at these two selected structures were completed using AlphaGUARD PQ2000 Pro radon monitor. In practice, radon gas is automatically drawn out into the ionization chamber of the device with a steady continuous pumping rate of 0.3L/min. For each measurement, the radon activity is sampled in 10-min intervals over a period of one hour. The system is equipped by an ionization chamber with a detection limit of 2-2000.000 $Bq.m^{-3}$. The applied technique based on the principle that the action of tectonic stresses and shearing processes that commonly occur along the rupture zones of faults could remarkably enhance the level of radon emissions owing to increasing rock permeability of the deformed structures (Yuce *et al.*, 2017). Consequently, considerable information concerning the trend and location of the fault zone, besides understanding the nature of its tectonic activity, could be achieved through analyzing the distribution pattern of soil radon emission and defining the spatial tendency of the anomalous halos in the survey area (King *et al.*, 1996; Baubron *et al.*, 2002; Richon *et al.*, 2010; Al-Hilal and Al- Ali, 2010). The results in most of these researches revealed a clear association between the occurrence of high radon variations and the general trends of fault zones. This finding implies that the movement of radon in the ground is greatly dependent on the degree of soil permeability and the extent of fracturing in bedrocks.

Data Analysis

The set of our radon data was statistically analyzed in order to define their spatial distribution with respect to the fault trend. Such processes would assist the separation between normal radon concentrations from other anomalous or tectonic related values (Table 1). The analysis includes the estimation of minimum, maximum, mean value (x), standard deviation (SD) and the coefficient of vari-

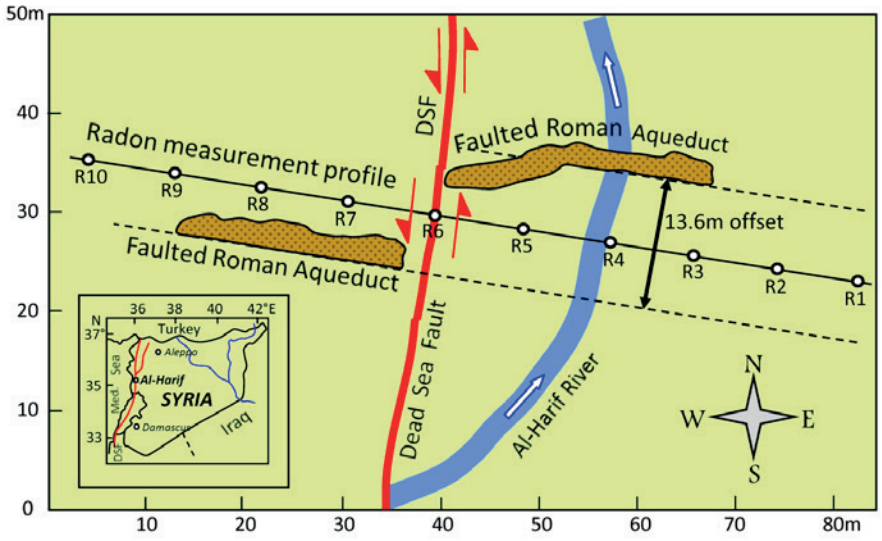

Figure 4. A sketch map of the Al-Harif site showing the trend of the Dead Sea Fault (red solid line), the radon profile (black solid line) and the location of the Al-Harif ancient aqueduct, which was faulted and displaced left-laterally by a total horizontal offset of ~13.6 m.

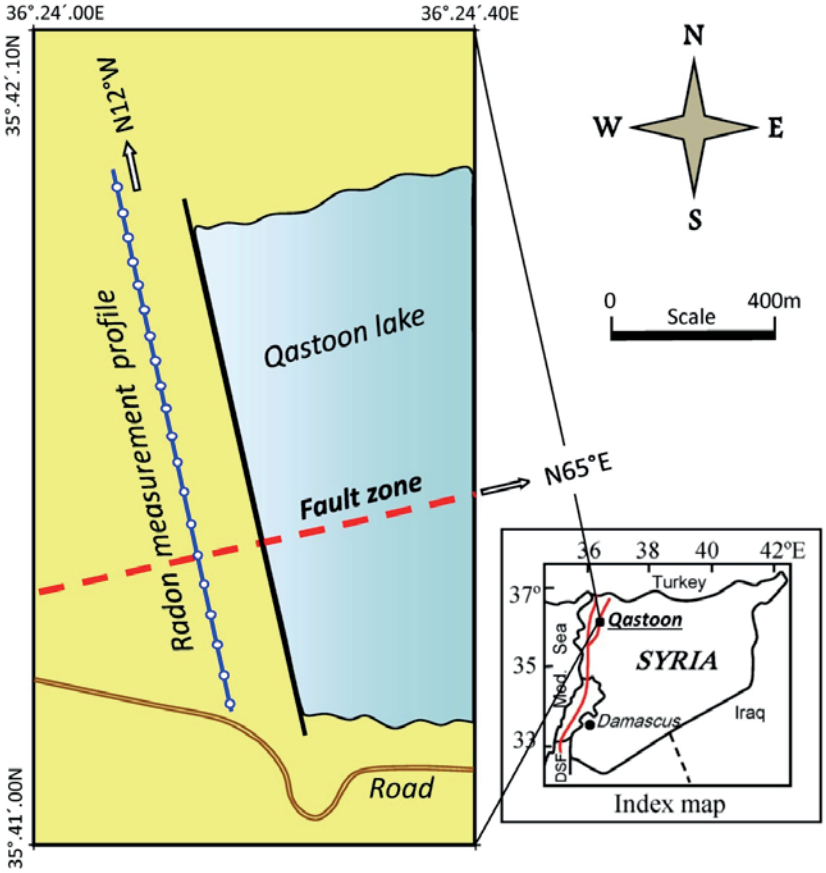

Figure 5. A sketch map of the Qastoon site illustrating the intersection of the radon profile (blue solid line) with the general trend of the Qastoon fault (red dash line.

ability (CV%), which reflects the degree of radon homogeneity in the investigated site, the higher the coefficient of variability, the lower the homogeneity of radon distribution in soil. The value of CV is generally calculated through the following formula:

$$CV\%=(SD/x)*100 \quad (1)$$

Additionally, in order to get a better insight into the variability of radon concentration in soil, radon data was standardized in terms of probability of magnitude, which could assist in identifying anomalous radon signals (Crockett and Holt, 2011). In general, the Standardized Radon Index (SRI) is a statistical procedure by which similar data received in various formats is converted into a common format that enhances the comparison process and helps to maximize compatibility. Accordingly, the monthly mean values of radon concentration (Ci) have been standardized (Cs) by using the following formula:

$$Cs=(Ci-x)/SD \quad (2)$$

Where (x) and (SD) are the mean value and the standard deviation, respectively.

Table 1. Results of soil radon measurement data carried out across the Qastoon and Al-Harif fault segments in northwestern Syria

	Al-Harif Fault Rn±error (Bq.m^{-3})		**The Qastoon Fault Rn±error (Bq.m^{-3})**		
	Round 1	**Round 2**	**Round 1**	**Round 2**	**Round 3**
	13570±1435	12170±1211	9740±1110	12345±1288	13300±1389
	16450±2100	16480±2110	8780±988	11734±1387	13678±1461
	16730±2170	13100±1390	14870±1890	10988±1322	11850±1390
	29622±3766	45750±6112	11488±1366	13456±1400	15300±2000
	68310±8533	62500±7355	18750±2220	12700±1406	19870±2411
	41350±5245	45940±6180	45800±6110	32891±4261	39113±4900
	46540±6645	39300±4980	40500±4960	25366±3000	36300±4767
	17800±2255	13670±1400	50280±6653	53870±7411	56100±7306
	18230±2344	15985±2210	38350±4566	33700±4110	42780±5409
	15433±2150	12811±1408	34650±4430	41258±5176	38200±4908
	-	-	23500±2975	31870±4100	31320±3980
	-	-	24500±3100	26250±3211	30840±3877
	-	-	14950±2000	24880±3005	20950±2560
	-	-	16150±2122	17450±2000	19740±2205
	-	-	13477±1730	19630±2200	18300±2100
	-	-	14334±1895	12744±1408	17677±1984
	-	-	11199±1398	13100±1590	13170±1605
	-	-	11645±1411	13644±1675	12800±1460
	-	-	10790±1302	11488±1367	12022±1400
	-	-	9320±1178	10633±1288	11920±1391
Average	28404±3664	27771±3436	21154±2670	21500±2630	23762±2925
Min	13570±1435	12170±1211	8780±988	10633±1288	11850±1389
Max	68310±8533	62500±7355	50280±6653	53870±7411	56100±7306
SD	18178	18679	13284	12036	12890
CV (%)	64	67	63	56	54

Results and Discussion

According to the data listed in Table 1, it can be observed that radon concentration in the Qastoon fault varied from 8780 to 56100 Bq.m^{-3} with mean average value of 22139 Bq.m^{-3}, a standard deviation of 12737 and 58% coefficient of variability. While radon concentration in the Al-Harif fault ranged between 12170 and 68310 Bq.m^{-3} with mean average value of 28087 Bq.m^{-3}, a standard deviation of 18428 and 66% coefficient of variability. In order to avoid possible effects of meteorological variables on soil radon concentration, the survey was performed under comparable weather conditions during dry seasons, where air temperature varied between (35-40 °C) and (25-30 °C) for the Qastoon and Al Harif sites, respectively. Besides, the prevailing atmospheric pressure varied between (990-995 mb) and (956-960 mb) for the Qastoon and Al Harif, respectively. Further, the normal background level of soil radon activity in the study area was established in a separate stationary site that is located far from the tectonic influence of the studied faults zones. Although the average background value of local soil radon emission was set at ~10000±1200 Bq.m^{-3}, the maximum radon peaks that measured above the predictable traces of the Qastoon and Al Harif fault ruptures showed much higher concentrations, exceeding 56000 and 68000 Bq.m^{-3}, respectively (Figs. 6 & 7). This implies that the value of "signal-to-background ratio" indicates clear fault-associated radon anomalies with six to seven fold increases that are found in a spatial agreement with the general trends of the concerned fault zones. Such finding may verify the possibility of using radon as a reliable indicator for characterizing fault structures, and providing an insight into the significant role of local active tectonics in influencing the activity level of soil radon emissions.

As mentioned previously, the estimated rates of radon coefficient variability (CV) in the Qastoon and Al-Harif sites revealed values of 58% and 66%, respectively. Thus, it can be deduced that the common dispersal pattern of radon variations in both sites seems to be fairly high, and this may reflect low homogeneity model. Such disparity might be referred to the differences in the concentrations between zones with higher radon signals that are usually associated with the fault structures, and area with normal radon emission that are naturally emanated from the surrounding unaltered rocks. Additionally, so as to justify that the anomalously high radon values are mainly related to tectonic activities and not only derived from the decay of radium in soil, chemical analysis for 226Ra content in soil was accomplished in some samples collected from the same locations where the radon concentrations were measured. The results of the analysis revealed very low concentration of radium values ranging from 1.06±0.08 to 1.14±0.20 mg.kg^{-1}, with some results below the detection level (DL= 1 mg.kg^{-1}).

Furthermore, in order to display the differences between normal radon variations from other anomalous or tectonically-induced radon values, we used in this study the method of Standardized Radon Index (SRI). The principle of this technique is comparable to the Standardized Precipitation Index (SPI) used in drought modeling, where negative values indicate dry period and positive values point to wet period due to high precipitations (Crockett and Holt, 2011; Al-Hilal, 2016). According to the SRI method, the spatial correlation between the rate of soil radon emission and the geodynamic activity along the location of the fault zone has been highlighted. Thus, the comparison process of data has been enhanced, in order to show clear radon peaks that are compatible with the assumed trace of the fault ruptures as presented in Figs. 6 & 7. One significant result of this study is the occurrences of remarkable soil radon increases observed across the Al Harif fault in spatial agreement with a gap located between two pieces of a faulted ancient Roman aqueduct named locally as

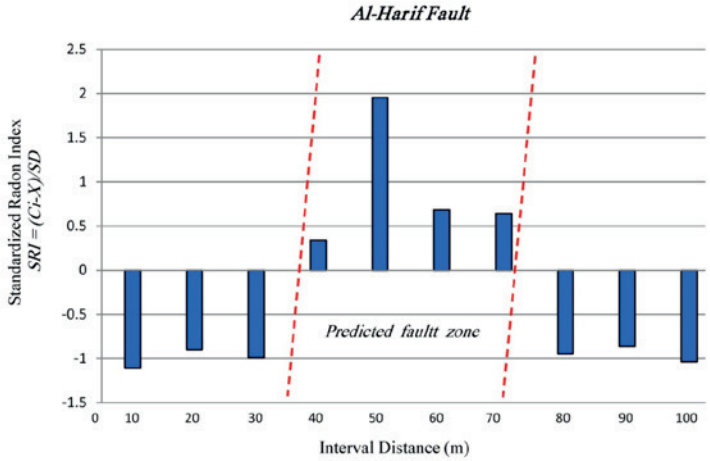

Figure 6. Standardized radon index (SRI), where anomalous radon peaks are correlated with the trace of the surface fault rupture, while negative values point to the background level.

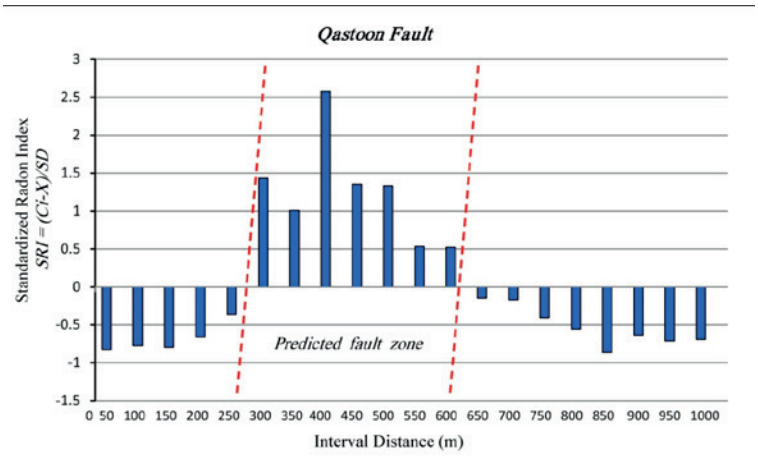

Figure 7. Standardized radon index (SRI), where anomalous radon peaks are correlated with the trace of the surface fault rupture, while negative values point to the background level.

Al-Harif aqueduct (Fig. 4). As mentioned earlier, results from archaeoseismic and palaeoseismic surveys revealed evidences that Al Harif aqueduct was fractured and repeatedly displaced left-laterally by a total horizontal offset of 13.6±0.2 m due to successive displacements of three seismic events occurred along the NDSF (Meghraoui *et al.*, 2003). Additionally, field observations indicated that the displacement of the aforesaid ancient aqueduct is well correlated with clear leftward deflections of some local streams, coinciding with the fault scarp, and most likely implying recent active tectonics along this part of the NDSF. Furthermore, Asfahani *et al.*, (2010) carried out integrated geophysical and morphotectonic surveys in the Qastoon area, which is located along the eastern bounding fault of the Ghab pull-apart basin of the NDSF (Fig. 5). The overall results of their investigations led to the detection of an active tectonic structure which was developed through the ongoing active tectonic processes of the NDSF. Accordingly, it is worth to mention that these findings are very well corresponded with the results obtained from the present study which revealed clear anomalous rises of soil radon signals that occurred in agreement with the general trends of the Qastoon and Al

Harif fault lines. Therefore, it seems quite significant to shed more light on these tectonically active structures, particularly in terms of their potentiality to cause a probable seismic hazard to the study region. In other words, the consequences of our radon survey showed additional evidences of possible spatial fault-associated radon anomalies, and thereby verify the usefulness of using radon method as a reliable approach for characterizing some buried deformed structures and active faults in similar geologic environments elsewhere. In fact, the variability of soil gas radon concentration with regard to the tectonic activity of faults is basically related to the constant effects of the concentrated stress along with accumulated strains which usually result in high crustal deformations and thereby increase the degree of rocks permeability along the fault rupture zone. Such geodynamic changes will in turn enhance the mechanism of upward soil gases flow, and so increase the emanation rate of radon through the fractured bedrocks up to the ground surface.

Lastly, according to our results, and those reported in some other literatures, that the main advantages of using radon measurement technique as an important mean in some geologic and tectonic studies, can be summarized as follows: (1) the relatively low-cost and simplicity of conducting radon measurements; (2) the method is direct and the results are instantly available; (3) radon is a natural element, so this will avoid the addition of any synthetic materials to the environment. On the other hand, attention should be paid to some disadvantages that may encounter the application of radon methods, these include: (1) the variability of radon gas due its sensitivity to the ambient environmental conditions; (2) the effect of geology and the composition of the prevailing rocks at the measurement site; (3) and the relatively short half-life of radon, so it might be dispersed sometimes before reaching the ground surface. Thus, for better results and high accurate performance, it is essential to maintain the radon instrument calibrated before measurements start. Also it is recommended to carry out multiple radon samplings at the same measurement site as this would sufficiently minimize the possible occurrence of errors.

Conclusions

Systematic soil radon measurements have been performed across the Qastoon and the Al-Harif faults which represent two active tectonic segments of the northern Dead Sea Fault in northwestern Syria. The radon investigations were mainly guided by the results drawn from previous geophysical, morphotectonic, archaeoseismic and palaeoseismic surveys which were achieved in the same area and attested to the tectonic activity of the concerned fault structures. The overall results revealed the presence of a clear fault-associated radon anomaly with about six to seven fold increase of radon concentration, trending in accordance with the traces of the surface fault rupture at the Qastoon and Al-Harif, respectively. One significant result of this study is the observation of some anomalous radon increases that are remarkably corresponded with a gap located between two pieces of a faulted ancient Roman aqueduct at Al Harif site. The aqueduct was fractured and repeatedly displaced left-laterally by a total horizontal offset of 13.6±0.2 m due to successive fault movements of three seismic events occurred along the Dead Sea Fault. Another point of interest is the notable occurrences of some anomalous radon emissions that are spatially consistent with the general trend of the Qastoon rupture fault zone which was detected and outlined by previous integrated geophysical and morphotectonic surveys. Ultimately, the aforesaid results could represent additional evidences regarding the possibility of using radon as a reliable and sensitive indicator for characterizing fault structures, and providing an insight into the significant role of local active tectonics in enhancing the level of soil radon emission.

Acknowledgement

The author would like to express his gratitude and thanks to Professor I. Othman, Director General of the Atomic Energy Commission of Syria (AECS), for his constant encouragement. Thanks are also due to Dr. Z. Kattan, Head of the Geology Department of the AECS, for his assistance and support. I gratefully acknowledge the anonymous reviewers and the editors of the *Geofísica Internacional* for their valuable suggestions and remarks that considerably improved the quality of the paper. This work is part of a local scientific research No. AECS-G\RSS 979/2012.

References

Akyuz H., Altunel E., Karabacak V., Yalciner C., 2006. Historical earthquake activity of the northern part of the Dead Sea fault zone, southern Turkey. Tectonophysics 426:281–293

Alchalbi, A., Daoud, M., Gomez, F., McClusky, S., Reilinger, R., Romeyeh, M.A., Alsouod, A., Yassminh, R., Ballani, B., Darawcheh, R., 2010. Crustal deformation in northwestern Arabia from GPS measurements in Syria: slow slip rate along the northern Dead Sea fault. Geophys J Int. 180:125–135. doi:10.1111/j.1365- 246X.2009.04431.x

Al-Hilal M., Al-Ali A., 2010. The role of soil gas radon survey in exploring unknown subsurface faults at Afamia B Dam, Syria. Radiat. Meas. 45:219–224

Al-Hilal M., 2016. Establishing the range of background for radon variations in groundwater along the Serghaya fault in southwestern Syria. *Geofísica Internacional* 55-4:215–225. DOI: 10.19155/geofint.2016.055.4.3

Al-Hilal M., and Abdul-Wahed MK., 2016. Tectonic and geologic influences on soil gas radon emission along the western extension of Damascus fault, Syria. Environmental Earth Sciences 75(23):1-11. DOI: 10.1007/s12665-016-6292-z

Al-Hilal M., and Abdul-Wahed MK., 2018. Soil gas radon measurements for investigating the actual status of seismic quiescence along the bounding fault of the Ghab pull-apart basin in western Syria. *Geofísica Internacional* (2018) 57-3: 89-106

Ambraseys N.N. and Jackson J.A., 1998. Faulting associated with historical and recent earthquakes in the Eastern Mediterranean Region, *Geophys. J. Internat.* 133, 390–406.

Ambraseys, N.N. and Barazangi, M. 1989. The 1759 earthquake in the Bekaa valley: implications for earthquake hazard assessment in the eastern Mediterranean region. *Journal of Geophysical Research*, 94, 4007–4013

Asfahani J., Radwan Y., Layyous I., 2010. Integrated Geophysical and Morphotectonic Survey of the Impact of Ghab Extensional Tectonics on the Qastoon Dam, Northwestern Syria. *Pure Appl. Geophys.* 167 (2010), 323–338. DOI 10.1007/s00024-009-0019-y

Barazangi, M., Seber, D., Chaimov, T., Best, J., Li tak, R., Saad, D. and Sawaf, T., 1993. Tectonic evolution of the northern Arabian plate in western Syria. Recent Evolution and Seismicity of the Mediterranean Region, E. Boschi *et al.*,(eds.), PP.117-140.

Baubron, J.C., Rigo, A., Toutain, J.P., 2002. Soil gas profiles as a tool to characterize active tectonic areas: the Jaut Pass example (Pyrenees, France). *Earth and Planetary Science Letters* 196, 69–81.

Brew G, Lupa J, Barazangi M, Sawaf T, Al Imam A, Zaza T., 2001. Tectonic and geological evolution of Syria. J Geol Soc Lond 158:665–674 Bulletin of the Syrian National Seismological Network (SNSN), (1995-2012), National Earthquake Center, Ministry of Petroleum and mineral resources, Syrian Arab Republic.

Butler, R.W.H. Spencer, S. Griffiths, H.M., 1997. Transcurrent fault activity on the Dead Sea Transform in Lebanon and its implications for plate tectonics and seismic hazard, *J. Geol. Soc. London* 154 (1997) 757-760. 17

Crockett RGM, Holt C P., 2011. Standardized Radon Index (SRI): a normalization of radon data-sets in terms of standard normal variables. Nat. *Hazards Earth Syst. Sci.*, 11, 1839–1844.

Devyatkin, E. V., Dodonov, A. E., Sharkov, E. V., Zykin, V. S., Simakova, A. N., Khatib, K. and H. Nseir, H., 1997. The

El-Ghab Rift Depression in Syria: Its Structure, Stratigraphy, and History of Development. *Stratigraphy and Geological Correlation*, Vol. 5, No. 4, 1997, pp. 362–374.

Etiope G. and Martinelli G., 2002. Migration of carrier and trace gases in the geosphere: an overview. *Physics of the Earth and Planetary Interiors*, 129, 185-204.

King, C.Y., King, B.S., Evans, W.C., Zhang, W., 1996. Spatial radon anomalies on active faults in California. *Appl. Geochem*. 11 (4), 497–510.

Kobeissi M. A., Gomez F., Tabet C., 2015. Measurement of Anomalous Radon Gas Emanation Across the Yammouneh Fault in Southern Lebanon: A Possible Approach to Earthquake Prediction. *Int. J. Disaster Risk Sci.* (2015) 6:250–266 www.ijdrs.com. DOI 10.1007/s13753-015-0058-1

McCalpin, J. 2009. In Paleoseismology, 95. Ed. McCalpin. 2nd ed. Academic Press.

Meghraoui M., 2015, Paleoseismic History of the Dead Sea Fault Zone. Encyclopedia of Earthquake Engineering, DOI 10.1007/978-3-642-36197-5_40-1

Meghraoui M., Francisco Gomez, Reda Sbeinati, Jerome Van der Woerd, Michel Mouty, Abdul Nasser Darkal, Youssef Radwan, Ihsan Layyous, Haithem Al Najjar, Ryad Darawcheh, Fouad Hijazi, Riad Al-Ghazzi, Muawia Barazangi, 2003. Evidence for 830 years of seismic quiescence from palaeoseismology, archaeoseismology and historical seismicity along the Dead Sea fault in Syria. *Earth and Planetary Science Letters* 210, 35-52 18

Mojzes Andrej, Frantisek Marko, Barbara Porubcanova, Andrea Bartosova, 2017. Radon measurements in an area of tectonic zone: A case study in Central Slovakia. *Journal of Environmental Radioactivity* 166 (2017) 278-288

Ponikarov, V. P., 1966. The geology of Syria. Explanatory Notes on the Geological Map of Syria, scale 1:200 000. Sheets I-37-XIX and I-36-XXIV, Ministry of Industry, Damascus, Syrian Arab Republic.

Richon, P., Klinger, Y., Tapponnier, P., Li, Ch.-X., Van Der Woerd, J., Perrier, F., 2010, Measuring radon flux across active faults: Relevance of excavating and possibility of satellite discharges. Radiat. Meas. 45, 211-218.

Sbeinati MR, Darawcheh R., Mouty M., 2005. The historical earthquakes of Syria: an analysis of large seismic events from 1365 B.C. to1900 A.D. *Ann Geophys* 48:347–435

Tanner, A.B., 1964. Radon migration in the ground: a review. In: Adams, J.A.S., Lowder, W.M. (Eds.), the Natural Radiation Environment. *Univ. Chicago Press*, Chicago, pp. 161–184.

Yuce, G., Fu, C.C., D'Alessandro, W., Gulbay, A.H., Lai, C.W., Bellomo, S., Yang, T.F., Italiano, F., Walia, V., 2017. Geochemical characteristics of soil radon and carbon dioxide within the Dead Sea Fault and Karasu Fault in the Amik Basin (Hatay), *Turkey. Chem. Geol.* 469, 129–146.

Original paper

https://doi.org/10.22201/igeof.00167169p.2022.61.2.2199

Seismic risk in the State of Colima, México: Application of a Simplified Methodology of the Seismic Risk Evaluation for the Localities with Low-Rise, Non-Engineered Housing

Vyacheslav M. Zobin[1] and Imelda Plascencia

Received: November 10, 2021; accepted: March 27, 2022; published on-line: April 1, 2022.

Resumen

El estudio de riesgo sísmico es un elemento importante en la evaluación de peligros naturales, especialmente en las regiones de alta actividad sísmica y baja calidad structural de las viviendas. Las nuevas tecnologías, desarrolladas para reducir el riesgo de peligros naturales en las grandes ciudades modernas, son costosas y necesitan un monitoreo instrumental continuo de movimientos fuertes. El problema principal en la estimación del riesgo sísmico para las localidades, que representan las viviendas vulnerables de baja altura y sin ingeniería (BASI) en muchos estados de África, Asia y América Latina, consiste en la búsqueda de una herramienta óptima y de bajo costo para la estimación del alcance del daño físico a la propiedad para diferentes tipos de vivienda. Este artículo propone una metodología simplificada de evaluación de riesgo sísmico para las localidades, donde las casas vulnerables tipo BASI representan la mayoría de las construcciones residenciales. La metodología se basa en la evaluación de las siguientes fuentes de información: los catálogos de terremotos recientes e históricos a nivel mundial disponibles en INTERNET y la inspección visual y clasificación del nivel de vulnerabilidad de las casas residenciales tipo BASI así como la inspección macrosísmica visual de los daños de las casas residenciales después de terremotos destructivos. Esta metodología se aplica a las localidades del Estado de Colima, México caracterizándose con viviendas residenciales tipo BASI. El pronóstico de probabilidad de daños durante un gran terremoto para viviendas residenciales en la ciudad de Colima, basado en esta metodología, fue propuesta por primera vez en 1999 y luego se actualizó en 2007 después del análisis de la distribución de daños ocurridos durante el terremoto de M_w 7.5 de 2003 (*MM* VII en la ciudad de Colima). El artículo presenta la microzonificación del riesgo sísmico para dos localidades del Estado de Colima junto con un pronóstico probabilístico del daño esperado en viviendas y pérdidas financieras durante los terremotos de máxima intensidad en las localidades.

Palabras Clave: riesgo sísmico, peligro sísmico, vulnerabilidad sísmica, terremoto y microzonificación.

**Corresponding author at vzobin@ucol.mx*

[1] *Centro Universitario de Estudios Vulcanológicos, Universidad de Colima, Colima, 28045, México*

Abstract

The study of seismic risk is important element in the natural hazard assessment, especially in the regions of high seismic activity and low structural quality of housing. The new technologies, developed to reduce risk against natural hazards in large modern cities, are expensive and need in continuous instrumental monitoring of strong motions. The main problem in estimation of the seismic risk for the localities, representing with the vulnerable low-rise, non-engineered (LRNE) housing in many states of Africa, Asia and Latin America, consists in a search of an optimal and low-cost tool for estimation of the extent of physical damage to property for different type of housing. This article proposes a simplified methodology of the seismic risk evaluation for the localities, where the vulnerable LRNE houses represent most residential constructions. The methodology is based on evaluation of the following sources of information: the internet-available catalogs of world-wide recent and historical earthquakes and visual inspection and classification of the vulnerability level of residential LRNE houses as well as a visual macroseismic inspection of the residential house damage after destructive earthquakes. This methodology is applied to the localities of the State of Colima, México characterizing with the LRNE type of residential houses. The prognostic of damage probability during large earthquake for residential houses in Colima city, based on this methodology, was firstly proposed in 1999 and then was updated in 2007 after the analysis of damage distribution during the M_w 7.5 earthquake of 2003 (*MM* VII in Colima city). This article presents microzoning of the seismic risk for two localities of Colima State together with a probabilistic prognostic of the expected damage in housing and financial losses during the maximum intensity earthquakes at the localities.

Key words: seismic risk, seismic hazard, seismic vulnerability, earthquake and microzoning.

Introduction

Seismic risk (SR) is the probability that social or economic consequences of earthquakes will be equal to, or exceed, specified values at a site, a several sites, or in an area, during a specified exposure time (EERI Committee on Seismic Risk, 1984). The size of SR is constrained by the convolution of two parameters: the seismic hazard (SH), and seismic vulnerability (SV). The SH is defined as a property of an earthquake that can cause damage and loss (McGuire, 2004). The SV is the probabilistic value of damage in the structure for possible earthquake intensities (Caicedo *et al.*, 1996). Therefore, SH describes the natural phenomenon, or property, of an earthquake and SV describes the ability of houses to resist this earthquake. Finally, SR describes the probability of financial losses and damage that could be caused by SH depending on the level of SV (Wang, 2009).

The higher SR is expected for the regions of high seismic activity and low quality of housing. Both factors are common for many states throughout the world. At the same time, if the level of seismic activity may be the same for a locality, the quality of housing within the locality may differ significantly.

The new technologies, developed to reduce risk against natural hazards in large modern cities, are expensive and need in continuous instrumental monitoring of strong motions. The deterministic seismic hazard analysis has applications for some significant structures, such as nuclear industry, power plants, large dams, large bridges, etc. Probabilistic seismic hazard analysis is a widely used approach for the determination of seismic design loads for engineering structures (Atkinson, 2004; Petersen *et al.*, 2018). The seismic vulnerability assessment, applied to detect, inventory, and rank the most vulnerable buildings in Northern Eskisehir city, Turkey, illustrates the study of the seismic

risk for modern high-rise city (Albayrak *et al.*, 2015). They calculated the Earthquake Risk Score of each reinforced concrete buildings in Northern Eskisehir, and the most dangerous buildings with respect to the expected amount of earthquake damage were identified.

For localities, where the vulnerable low-rise, non-engineered (LRNE) houses represent most residential constructions, these technologies are not acceptable and have no great sense. One- and two-story masonry buildings are common in the rural areas because they require easy workmanship. These buildings are constructed with thick adobe and stone walls and mostly vulnerable to strong ground motions. These structures are constructed with traditional techniques using locally available materials. Nearly no engineering services are used in these buildings. Adobe blocks are produced from local material contains mixed soil with straw and leave dried under the sun. As adobe blocks have low strength, walls of masonry buildings are thick and massive (Maqsood and Schwarz, 2009; Sayin *et al.*, 2013; Yon *et al.*, 2017).

The main problem in estimation of the SR for the localities, representing with the vulnerable LRNE houses in many states of Africa, Asia, and Latin America, consists in a search of an optimal and cheap tool for estimation of the extent of physical damage to property for different type of housing. This does not require the optimal determination of seismic design loads for engineering structures, they have not this type structures. As was noted, for example, in description of the *M* 7.3 Iran-Iraq border earthquake of 12 November 2017, killing more than 400 people and injuring more than 7,000 (https://www.bbc.com/news/world-middle-east-41972338), many homes in the predominantly Kurdish mountainous area were made of mud bricks and became vulnerable in quakes as large as this. The following points are the most important: estimation of the maximum intensity of earthquake for locality and a probability of the level of damage and of financial losses for each type of LRNE houses in this locality.

Our paper proposes the simplified methodology for seismic risk evaluation (SMSRE) for this type of localities. Then this methodology is applied to the localities of the State of Colima, México characterizing with the LRNE type of residential houses. The microzoning of the seismic risk for these localities is presented together with a probabilistic prognostic of the expected losses during the maximum intensity earthquakes at the localities. This study was realized within the project of preparation of the "Atlas of hazards and risks in the State of Colima" (Atlas…, 2015).

Simplified Methodology of the Seismic Risk Evaluation for the Localities With the LRNE Type of Residential Houses

The methodology is based on evaluation of two main sources of information:

(1) The world-wide catalogs of earthquakes and the catalogs of historical earthquakes.

(2) Visual inspection and classification of the vulnerability level of residential LRNE houses and visual macroseismic inspection of the residential house damage after destructive earthquakes.

The seismic risk analysis within S*Ms*RE is basing on the same convolution of two parameters: the SH and the SV, characteristic for any earthquake source zone (ESZ). The analysis requires characterization of all known earthquake sources that could affect the site, including faults (line fault sources) and areas of seismicity (areal sources). To identify the ESZs, the epicentral maps of earthquakes are plotted, basing on the world-wide and (if any) local catalogs of earthquakes.

The world-wide catalogs of earthquakes, used for mapping of ESZs, are available for events, with a cutoff magnitude > 4.0-4.5, beginning from 1963, when the World-wide Standardized Seismograph Network (now developed in The Global Seismographic Network, https://www.iris.edu/hq/progra*Ms*/gsn; last access in February 2020) was installed (Peterson and Hutt, 2014). They may be found at different sites (e.g., http://quake.geo.berkeley.edu/anss/; last access in January 2020).

Calculation of the Elements of Seismic Hazard Generated by Earthquake Source Zone

As the elements of SH, the following characteristics for each ESZ are used: maximum magnitude of earthquakes occurring within a zone, M_{max}; recurrence time of appearance of the maximum magnitude earthquake, t; and the law of earthquake intensity attenuation with distance.

The maximum magnitude, M_{max}, is defined as the upper limit of magnitude for a given region. For areal sources, the estimation of the maximum magnitude has traditionally been computed by considering the largest historical earthquake in the source zone and adding some additional value (e.g. half magnitude unit). For fault sources, the maximum magnitude is usually computed based on the fault dimensions (length or area).

The recurrence time, t, for earthquake of magnitude M, is estimated considering the earthquake catalog corresponding to Poisson distribution of events, in which earthquakes occur randomly, with no regard to the time, size or location of any preceding event. As the recurrence model within the Poisson process of earthquake occurrence we use the log-linear Gutenberg-Richter magnitude-frequency relationship

$$Log\ N(M) = a - b\ M \tag{1}.$$

Here $N(M)$ is the cumulative number of earthquakes per year with a magnitude equal to or greater than magnitude M and a and b are constants for the seismic zone. The slope of the magnitude-frequency recurrence line, defined as a b-value, describes the relative abundance of large to smaller shocks. The magnitude-frequency relationship (1) allows to estimate the recurrence time of earthquakes of magnitude M occurring within ESZ.

Considering the earthquakes to be distributed randomly, the probability $P[N \geq 1]$ of at least one exceedance ($N \geq 1$) of a particular earthquake of maximum magnitude M_{max} in a period of T years is given by the following expression (Anbazhagan, 2011):

$$P[N \geq 1] = 1 - e^{-\lambda T} \tag{2}$$

where λ is the average rate of occurrence of the event with considered earthquake magnitude.

The law of earthquake intensity attenuation with distance may be obtained basing on the visual macroseismic inspection of the residential house damage after destructive earthquakes. The earthquake intensity is generally represented by the Modified Mercalli (*MM*) 12-grade intensity scale (Wood and Neumann, 1931). The standard macroseismic equation has a following form (Musson and Cecic, 2002; Montalvo-Arrieta *et al.*, 2017):

$$I = a\ M - b\ logR - cR \tag{3}$$

Here M is an earthquake magnitude, $R = (A^2 + h^2)^{1/2}$ is the hypocentral distance (in km), A is the epicentral distance (in km), h is the focal depth (in km), coefficients a, b and c are constants determined

by a least-squares fit to the observations. In the case of localities, representing with the vulnerable LRNE houses, the intensity values had to be corrected for the type of masonry and for different soil type (Zobin and Ventura-Ramirez, 1998; Zobin and Pizano-Silva, 2007).

The region of study geographically associates mainly with the province of Sierra Madre del Sur. The rocks forming this mountain chain are Precambrian and Paleozoic metamorphic and associated plutonic bodies, Upper Jurassic-Lower Cretaceous miogeoclinal deposits, and Plio-Quarternary and Tertiary volcanic rocks (de Cserna, 1989). All these rocks formed the firm soils that are good for constructions. They may be considered as high-quality firm rock soils. Only the narrow band of sand along the oceanic coast is unfit for construction use and requires the special foundations and antiseismic design. The sand and alluvial soils are considered as low-quality soft soils. The MM intensities on soft and firm soils differ by as many as 2 or 3; therefore, the difference between the soft and intermediate soil intensities could be equal to one grade.

Classification of the residential masonry buildings in localities with LRNE-type housing may be realized within three types of constructions (Zobin and Ventura-Ramirez, 1998):

Type A, low level of SV. Good quality low-rise buildings constructed with engineering project.

Type B, intermediate level of SV. Low-rise buildings constructed with use of quality materials but without engineering project.

Type C, high level of SV. Low-rise old buildings constructed without engineering project and with use of low-quality materials of adobe and cinder blocks.

The law of earthquake intensity attenuation with distance must be calculated using the intensity values referenced to the intermediate type of masonry and average type of soil.

Taking in account possible difference in macroseismic intensity attenuation during characteristic earthquakes of different source zones, a multi scenario assessment of the law (3) may be expected.

Evaluation of the Seismic Vulnerability of The Localities with LRNE Buildings

Seismic vulnerability is defined by a degree of damage that can be suffered by man-made constructions, and it depends on the design, the quality of materials, and the building techniques employed (Kuroiwa, 2004). The evaluation of SV of localities with LRNE-type residential buildings consists in classification of the buildings according to their level of vulnerability, as was mentioned above, and then in classification of the residential blocks that represent the main unit of the urban infrastructure.

The selection of a single building as a unit for a seismic risk assessment is not a practical choice. As it was mentioned in (ATC-13-1, 2002), it is impossible to use the damage probability derived for a class of buildings for a single-building analysis. For a single building, the uncertainty on a damage estimate can be larger than the uncertainty associated with the distribution of expected damage for a group of similar buildings. Therefore, a residential block must be selected as a convenient unit for a zonation of SR.

Evaluation of the Seismic Risk for the Localities with LRNE Buildings

Evaluation of the seismic risk (SR) for any locality in the regions of development of LRNE buildings may be based on the calculation of the damage probability matrix (DPM) for the masonry characteris-

tic for this region. The DPM, introduced by Whitman (1973), expresses the damage, experienced by a particular type of buildings, designed according to some set of requirements, during earthquakes of various intensities. The DPM is a popular tool for estimating losses caused by future earthquakes and is used widely to estimate the potential liability of insurance companies (ATC-13, 1985; Whitman, 1988; Blong, 2003). The DPM represents the expert-opinion motion-damage relationships for different types of buildings calculated for a set of earthquake intensities. The level of damage is described in terms of seven damage states (Whitman, 1988) and corresponding central damage factors, expressed in % (Table 1).

Table 1. The seven-grade scale of damages (based on Whitman, 1988).

Damage grade	Damage state	Central damage factor (%)	Comments
1	None	0	No fractures in plaster
2	Slight	0.5	Small, not numerous fractures in plaster
3	Light	5	Diagonal fractures in plaster
4	Moderate	20	Narrow closed diagonal cracks in walls
5	Heavy	45	Open diagonal cracks and spalls in walls
6	Major	80	Partly destroyed construction, con intention to demolish
7	Destroyed	100	Total destruction of the majority of the facility

Based on the expert-opinion DPM for three types of buildings described above, the probability P of damage for characteristic residential blocks may be calculated in the following way (Zobin and Ventura-Ramírez, 1999; Zobin *et al.*, 2006):

$$P = k\,(A)\,p\,(A) + k\,(B)\,p\,(B) + k\,(C)\,p(C)$$
$$k\,(A) = N\,(A)/\,N\,(A+B+C);$$
$$k\,(B) = N\,(B)/\,N\,(A+B+C);$$
$$k\,(C) = N\,(C)/\,N\,(A+B+C). \quad (4)$$

Here p (A, B, and C) is the probability of damage to the masonry of type A, B, and C, respectively, taken from the expert-opinion DPM, calculated for the buildings of a locality; N is the number of buildings of different type; and k (A, B, and C) is a weight coefficient for each type of masonry that form a typical block. Then we construct the DPM_block for each of blocks.

The DPM_block can be used to calculate the probabilistic matrix of the loss costs DPM_cost, which gives us knowledge about the probabilistic losses in housing prices of three types of buildings during earthquakes. To estimate the DPM_cost, is proposed to multiply DPM_block with the matrix consisting of the values of the central factors of damage for each of seven degrees of damage $P_{1\text{-}7}$

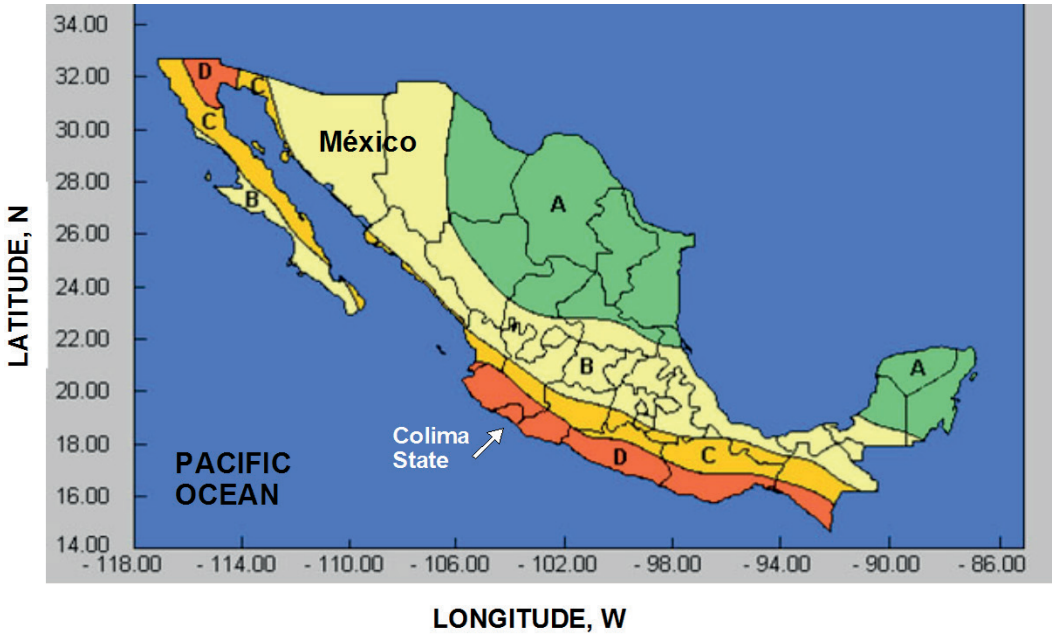

Figure 1. Map of seismic regionalization of Mexican Republic and position of Colima State within this map. Indexes of A, B, C and D indicate zones of different level of expected seismic intensity. Zone A corresponds to the lowest level of expected seismic activity and zone D, to the maximum level of expected seismic intensity. Taken from Manual (1993).

corresponding to the percentage of the losses in costs compared with the price of the house before the earthquake:

$$DPM\_cost = DPM\_block \times P_{1\text{-}7} \quad (5).$$

Here, P_7 corresponds to 100% of the losses compared to the price of the home, P_6 corresponds to 80% of losses, P_5 corresponds to 45% of losses, P_4 corresponds to 20% of losses, P_3 corresponds to 5% of losses, P_2 corresponds to 0.5% of the losses compared to the price of the home, and P_1 corresponds to houses without damage.

The microzonation of seismic risk for the locality with proposed I_{max} is determined by the distribution of three types of residential blocks of different vulnerability. The areas of distribution of the blocks with relatively high quality of buildings are defined as a zone of relatively low risk and the areas of distribution of blocks with relatively low quality of buildings as a zone of relatively high risk. The identification of the level of risk for every zone of locality may be obtained from the DPM_block, characteristic for every zone, by constructing of the probabilistic damage curves corresponding to proposed I_{max}. The probabilistic matrices of the loss costs DPM_cost, calculated for each zone, allow to estimate the probable losses due to building damage during earthquake.

In the following sections, we apply the described methodology for microzonation of the SR in some municipal centers of the Colima state, México (Fig. 1). This state is characterized by a high presence of the LRNE housing in its localities. We give the general characteristics of the tectonic and seismic activity of the state, mapping of its seismic hazard, and vulnerability assessment. Then, microzonation of the SR within municipal centers of the Colima state will be performed based on the DPM_block´s, estimated for housing of these localities.

General Characteristics of the Seismo-Tectonic Activity of the State of Colima

The State of Colima, México, selected as a region of study, is located along the Pacific coast, Western México (Fig. 1), and has an area of 5,784 km². Its population is equal to 711,235 persons (INEGI, 2015; http://cuentame.inegi.org.mx/monografias/informacion/col; last access in March 2020). The seismic regionalization of the Mexican Republic, shown in Fig. 1, indicates that the State of Colima is completely situated within zone *D*, the zone of maximum expected seismic intensity in México (Manual, 1993). The housing in localities of Colima state is characterized by a large percentage (70-80%) of the LRNE buildings (Zobin *et al.*, 2009; 2010).

Catalogs of Earthquakes Used

In this study, the following catalogs of earthquakes are used as a database:

1. The catalog of earthquakes with magnitudes ≥4.0 recorded in the region of study during the period from 1963 to 2016 and compiled by ANSS (Advanced National Seismic System, North California Earthquake Data Center) http://quake.geo.berkeley.edu/anss/.
2. The catalog of earthquakes with magnitude $M_s \geq 7.0$, recorded in the region of study during the period from 1900 to 1990 (Pacheco and Sykes, 1992).
3. The catalog of local shallow (depth 0-30 km) earthquakes with magnitude ≥4.0, recorded in the continental part of the region of study during 1989-2000 by the seismological network RESCO of the University of Colima (Zobin *et al.*, 2000).

Seismo-Tectonic Environment of the Colima State

Western Mexico represents a complex tectonic zone. The main tectonic elements of this region, the oceanic Rivera and Cocos plates, converge beneath the continental North American plate and produce large destructive earthquakes (Fig. 2). The earthquake epicenters outline the limits of the Rivera plate along the Tamayo (TFZ) and Rivera (RFZ) Fracture zones, East Pacific Rise (EPR) and Middle American trench (MAT), and its boundary with Cocos plate. The limits of the Cocos plate are outlined with the EPR and MAT. The Rivera-Cocos plate boundary zone is a complicated across-trench tectonic structure consisting of a few grabens and horsts (Bandy *et al.*, 2005). It runs across the Middle American trench along El Gordo graben (EGG). Earthquakes, associated with activity of the Rivera and Cocos plates and El Gordo graben, represent the earthquake source Zone 1 discussed in this article. Its limits are shown in Fig. 2.

During the period from 1900, totally six earthquakes with magnitude $M_w \geq 7.5$ (Nos 1-4, 7 and 8 in Table 2) were recorded within Zone 1. They occurred along the subduction zones of the Rivera and Cocos plates near Colima state and along the boundary zone between two plates, El Gordo graben. The reported macroseismic effect of these earthquakes reached intensity VII-X *MM* in the localities of Colima state (Figueroa, 1974; Singh *et al.*, 1985; Zobin and Ventura-Ramírez, 1998; Zobin and Pizano-Silva, 2007).

Two earthquakes of 1985 (Nos 5 and 6 in Table 2), shown in Fig. 2 to *SE* from Zone 1, were distant enough from Colima state and did not produce any damage in its localities.

In the continental part, the seismicity occurs along the boundaries of the block of Jalisco, represented by the grabens of Tepic-Zacoalco and of Colima (Fig. 3). The important element of tectonic

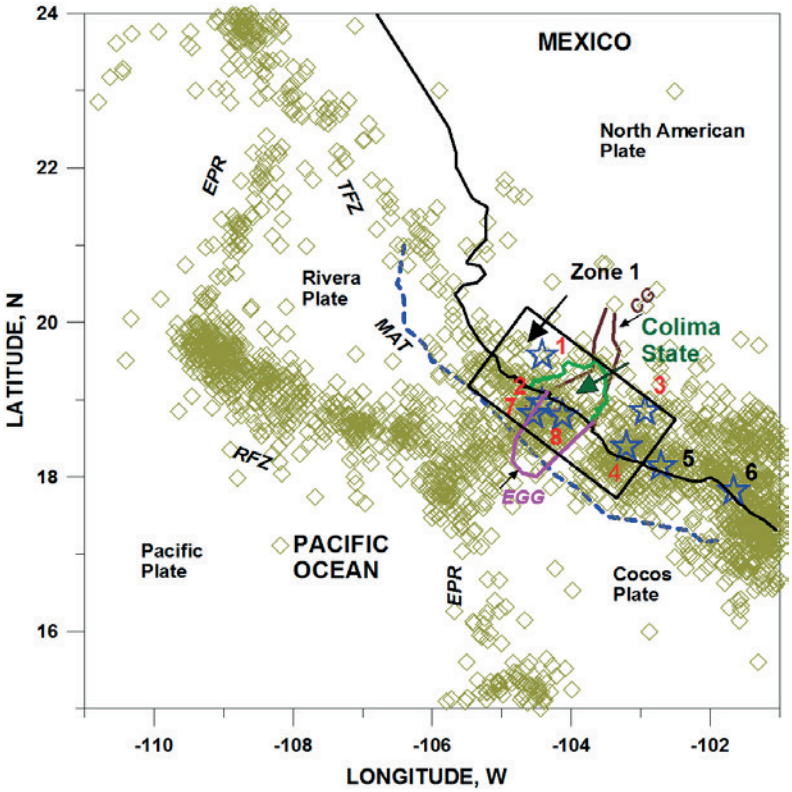

Figure 2. The principal lithospheric plates near the western coast of México and the epicenters of the 1963-2019 earthquakes with magnitudes ≥4.0, compiled by Advanced National Seismic System, North California Earthquake Data Center (http://quake.geo.berkeley.edu/anss/). The epicenters of earthquakes with magnitudes ≥4.0 are shown with diamonds. The stars show the epicenters of large earthquakes ($M_w \geq 7.5$) occurring during the period from 1900 to 2016; the events of Table 2 are indicated with numbers. Earthquake source Zone 1 is shown within rectangle. TFZ is Tamayo Fracture zone; RFZ is Rivera Fracture zone; MAT is Middle American trench; EPR is East Pacific rise; CG is Colima graben; EGG is El Gordo graben. The MAT is shown by a dashed line.

Table 2. List of earthquakes with magnitude $M_w \geq 7.5$ which occurred during the period from 1900 to 2016 within the area of study (See Fig. 2)

No	Date, yyyy_mmdd	Latitude, N	Longitude, W	M_w	M_s	Comments
1	1932_0603	19.57[1]	-104.42[1]	8.0[2–1]	8.0[2]	Rivera-N_A
2	1932_0618	18.95[2]	-104.42[2]	7.7[2–1]	7.6[2]	Aftershock of No 1
3	1941_0415	18.85[2]	-102.94[2]	7.6[2–1]	7.5[2]	Cocos-N_A
4	1973_0130	18.39[2]	-103.21[2]	7.6[2–1]	7.3[2]	Cocos-N_A
5	1985_0919	18.14[2]	-102.71[2]	8.0[2–1]	8.1[2]	Cocos-N_A
6	1985_0921	17.82[2]	-101.67[2]	7.7[2–1]	7.6[2]	Aftershock of No 5
7	1995_1009	18.81[3]	-104.54[3]	8.0[4]	7.3[4]	Rivera-N_A
8	2003_0121	18.79[5]	-104.13[5]	7.5[4]	7.6[4]	Rivera-Cocos

Note. 1, Eissler and McNally, 1984; 2, Pacheco and Sykes (1992); 2_1, magnitudes M_w calculated from seismic moments taken from Pacheco and Sykes (1992); 3, RESCO (Zobin, 1997); 4, Global CMT, http://www.globalcmt.org; 5, RESCO (Zobin and Pizano-Silva, 2007). N_A, North American plate. In comments, the plates, along which the rupturing occurred, are indicated.

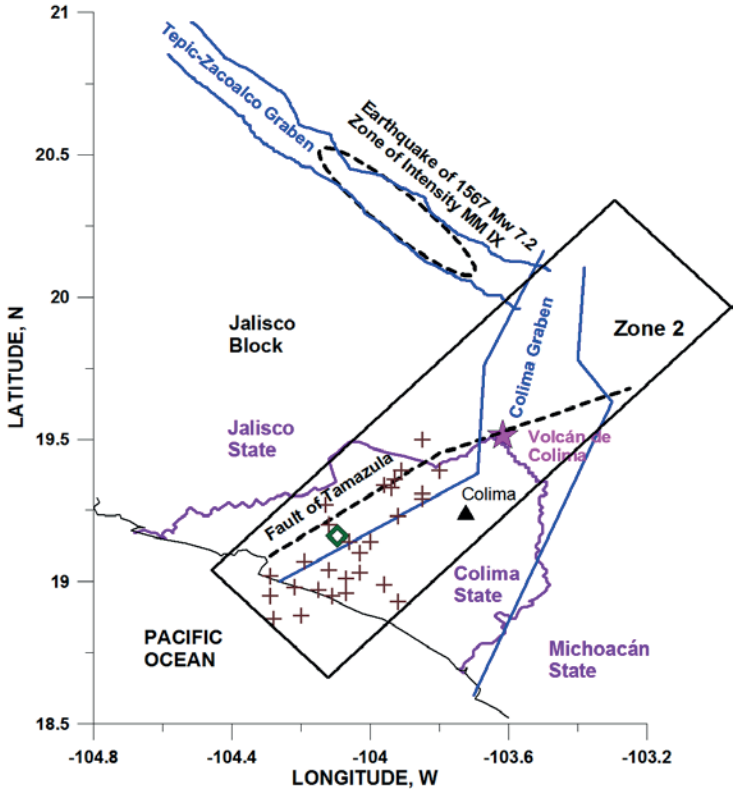

Figure 3. The principal tectonic structures of continental part of the Western México and epicenters of the crustal earthquakes with magnitudes ≥4.0 recorded during 1988-2000 by the seismic network RESCO of Colima University (Zobin et al., 2000). Earthquake source Zone 2 is shown within rectangle. The epicenter of the earthquake of 6 March 2000 (*Mw* 5.3) is shown with a diamond; the epicenters of its aftershocks are shown with crosses. Positions of Colima city and of Volcán de Colima are shown with triangle and star, respectively.

activity of the Jalisco block represents also the 160-km-length Tamazula fault, which goes parallel to Colima graben and then intersects it at surroundings of Volcán de Colima (Garduño-Monroy *et al.*, 1998). The active crustal deformation along the Jalisco block boundary faults serves as the origin of seismicity in the continental part of Western Mexico (Suárez *et al.*, 1994; Suter, 2015). Earthquakes, associated with activity of these tectonic faults, represent the earthquake source Zone 2 discussed in this article. Its limits are shown in Fig. 3.

The largest historical earthquake along the Jalisco block northern boundaries was recorded in December 1567 (or 1568) along the fault system of the Tepic-Zacoalco graben. A 70-km zone of destructions, whose descriptions correspond to intensity IX *MM* (Suárez *et al.*, 1994; Suter, 2015), is shown in Fig. 3. Suter (2015) estimates the magnitude of this earthquake equal to M_w 7.2.

Recent local seismicity of the Colima sector of the Jalisco block, recorded after installation of the regional seismic network in 1989 (Castellanos y Jiménez, 1995), occurs mainly along the Tamazula fault and Colima graben. The largest earthquake was recorded on 6 March 2000. It had magnitude M_w 5.3 and was felt in Colima state with intensity *MM* III-V (Zobin *et al.*, 2000).

Seismic Hazard of Colima State

Seismic hazard for localities of Colima state is conditioned by seismo-tectonic activity within two main zones of earthquake source generation, shown in Figs. 2 and 3 and discussed in Section of *Gen-*

eral characteristics of the seismo-tectonic activity of the State of Colima. In the following sections, three main parameters of the SH, the maximum magnitude M_{max}, the earthquake recurrence time t, and the law of seismic intensity attenuation with distance will be estimated for both zones.

Seismic Hazard of Earthquakes Originated within Zone 1

Zone 1 is outlined in Fig. 2. The rupture areas of 6 large earthquakes with $M_w \geq 7.5$, recorded within Zone 1 during the last 120 years and strongly felt in the State of Colima, are included within this Zone. Five of these large earthquakes occurred along the MAT during the subduction of the Rivera (Events Nos 1, 2 and 7 in Table 2) and Cocos (Events Nos 3 and 4) plates beneath the North American plate. The 2003 earthquake (No 8), also recorded within Zone 1, occurred along the border between the Rivera and Cocos plates within El Gordo Graben. We use the terms "along-trench" and "across-trench" to discriminate between earthquakes whose source ruptures developed in a direction parallel to the MAT or normal to it, respectively. This type of orientation may be traced by aftershock distribution or with reconstruction of the co-seismic slip within the rupture plane.

Maximum Magnitude M_{MAX}

To estimate the maximum magnitude of earthquakes, occurring within Zone 1, we analyze the magnitudes of large earthquakes recorded during the period of 1900-2016 in the area (Table 2). Five of the six $M_w \geq 7.5$ earthquakes of Zone 1, listed in Table 2, are individual events, and one, No. 2, is aftershock of the No. 1 event.

Two of five individual events, which occurred within Zone 1 during the period of about 120 years (Nos 1 and 7), had the magnitudes M_s or M_w equal to 8.0, respectively. The magnitude 8.0±0.5 may be taken as the magnitude M_{max} of the earthquakes from Zone 1.

Earthquake Recurrence Time

The relationship between the number of earthquakes, registered within Zone 1 during the period from 1963 to 2016, and their magnitudes is shown in Fig. 4A. The relationship is based on 524 events that occurred during the period from 1963 to 2016 at the depth interval of 0-100 km with magnitudes ≥4.0 (for events with magnitudes ≥6, only magnitudes M_w were used). The distribution of the cumulative numbers, N, of earthquakes per year, with magnitude greater than M, against their magnitudes M is linear with a correlation coefficient R = -0.995. The least square linear regression equation is

$$Log\ N = 3.64 - 0.68\ (\pm\ 0.02)\ M \qquad (6)$$

Equation (6) gives an option to estimate the annual rate of occurrence of earthquakes with the magnitude M 8.0 equal to 0.017. The recurrence period of earthquakes with magnitude M_{max} 8.0 in Zone 1 is equal to 60 years.

Considering the earthquakes to be distributed randomly, the probability of at least one exeedance of a maximum magnitude M_{max} earthquake in Zone 1 during the period of T=50 years after the last M_w 8.0 earthquake of 1995, given by the equation (2) in Section 2.1, is equal to 58%.

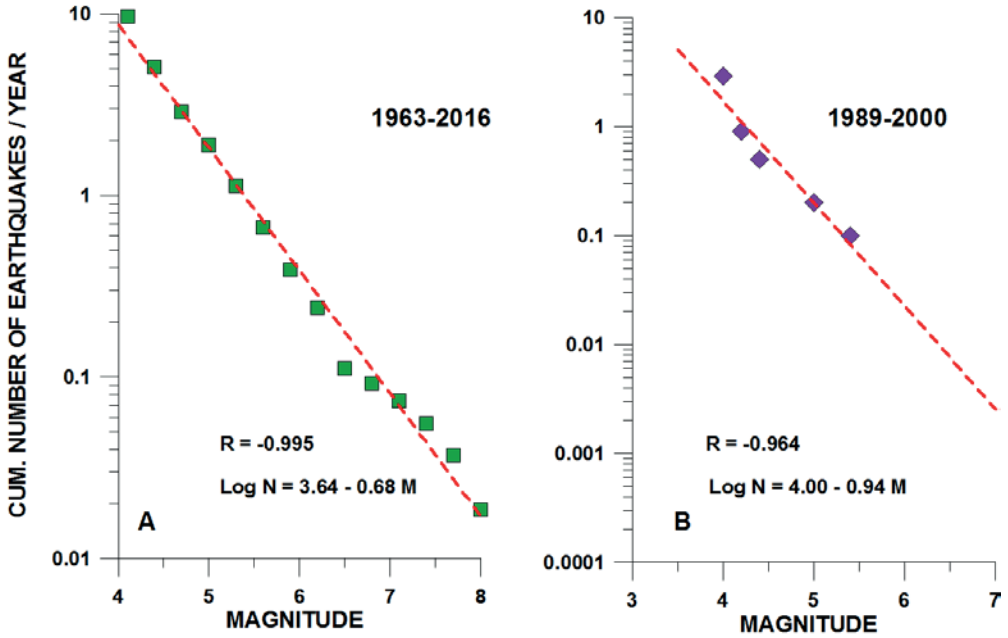

Figure 4. Relationship between the cumulative numbers of earthquakes recorded in Zone I (A) and Zone II (B) and their magnitudes.

Attenuation of Earthquake Intensity with Distance

In this section, we significantly deviate from the standard PSHA method which operates for the study of attenuation of earthquake intensity with distance with the curves of attenuation of instrumentally recorded ground motions or spectral accelerations (McGuire, 2004). The main reason for this deviation is the practical absence of the instrumentally recorded strong motions of the $M_w \geq 7.5$ earthquakes occurring within Zone 1. Only two acceleration records were obtained at the same site, in Manzanillo, for two earthquakes, of 1995 (No 7 in Table 2) and 2003 (No 8 in Table 2). Tejeda-Jácome and Chávez-García (2007) collected the acceleration records for 26 local Colima earthquakes but with magnitudes in the range of $3.3 < M < 5.2$. It gave them possibility to construct the attenuation curve for the magnitude 5 earthquake. In this situation, no data to construct the instrumentally based curves for large ($M_w \geq 7.5$) earthquake intensity attenuation with distance for the Colima state region were acceptable. The PGA attenuation curves, obtained in other regions can not be applied. As was shown by Tejeda-Jácome and Chávez-García (2007), the use of attenuation relations, derived with the data from other subduction regions, may underestimate the seismic hazard for Colima. Thus, this study uses only the macroseismic intensity, I, as a parameter for performing of attenuation curves for large earthquakes.

The intensity values of the 1932, 1941 and 1973 large earthquakes (Nos 1, 3 and 4 in Table 2) were derived from newspaper reports (1932 event, Singh *et al.*, 1985) or from newspaper reports and questionnaires obtained by mail and from municipal reports (1941 and 1973 events; Figueroa, 1974). As usual, this type of information dominated by the impressive destructive effects, observed for the LRNE-type buildings, and there was a high probability of over-estimation of the real intensity for the localities. At the same time, the shapes of the outer isoseismals (over-estimated or not), proposed by the mentioned authors, were not so dependent on the methodology and may show the general tendencies in intensity distribution (Fig. 5). All three earthquakes were characterized by the

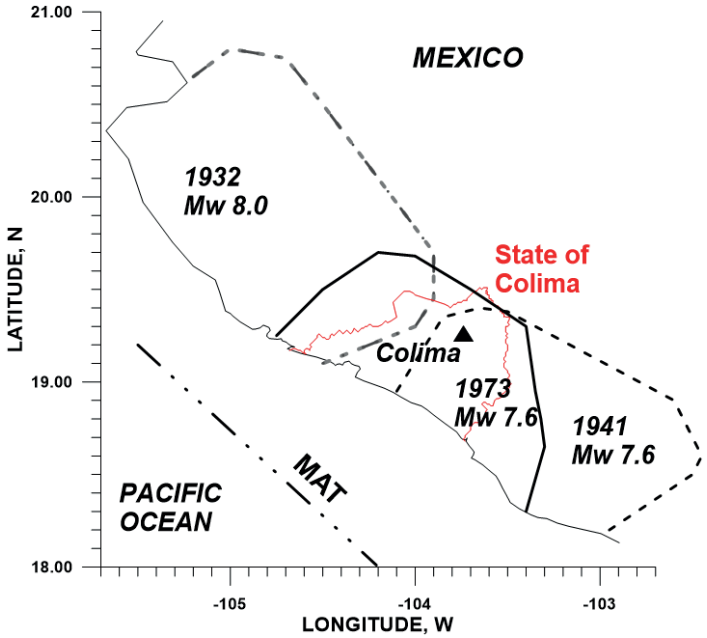

Figure 5. Isoseismals of maximum intensities estimated for large earthquakes of 1932, 1941 and 1973 (Nos. 1, 3, and 4 of Table 2, respectively). Colima city is shown with triangle. The borders of Colima state are shown with red line.

outer isoseismals of maximum intensity extended along the coast and parallel to the direction of the Middle American trench (along-trench events).

The intensity field for more recent earthquakes of 1995 and 2003 was reconstructed using the information, obtained during the personal interviews of the people who felt the earthquakes in their house, and with the inspection of type of masonry and quality of construction of the house. The questionnaires were based on the *MM* 12-grade scale. To avoid the effect of poor quality of rural constructions, the estimations of intensity were referenced to the type B masonry. In the case of absent of this type masonry, the corrections of intensity for the type and age of buildings were applied: +0.5 *MM* intensity for type A masonry and -0.5 *MM* for type C masonry. If the construction was older than 20 years, its category of masonry was decreased by one grade (from A to B, from B to C) (Zobin and Ventura-Ramírez, 1998; Zobin and Pizano-Silva, 2007).

Figs. 6 (A, B) show the isoseismal maps for these events together with the isolines of co-seismic slip within the rupture plane. In the case of the M_w 8.0 October 9, 1995, along-trench earthquake (Fig. 6A), totally 56 localities were inspected (Zobin and Ventura-Ramírez, 1998). Zones of maximum intensities (*MM* VI-VII), as well as the direction of co-seismic slip, were observed along the coastal zone parallel to the MAT.

The macroseismic study of the M_w 7.5 January 21, 2003, across-trench earthquake was performed for 83 localities (Zobin and Pizano-Silva, 2007). The macroseismic map of the 2003 earthquake (Fig. 6B) shows that the narrow (30 km wide) *MM* VII zone was elongated (up to 60 km) in the across-trench direction towards the continental part of Colima state coinciding with the direction of co-seismic slip.

The specific features of intensity patterns caused by the difference in rupture directivity do not allow calculating the *MM* intensity attenuation simply by taking all intensity observations. To have a ho-

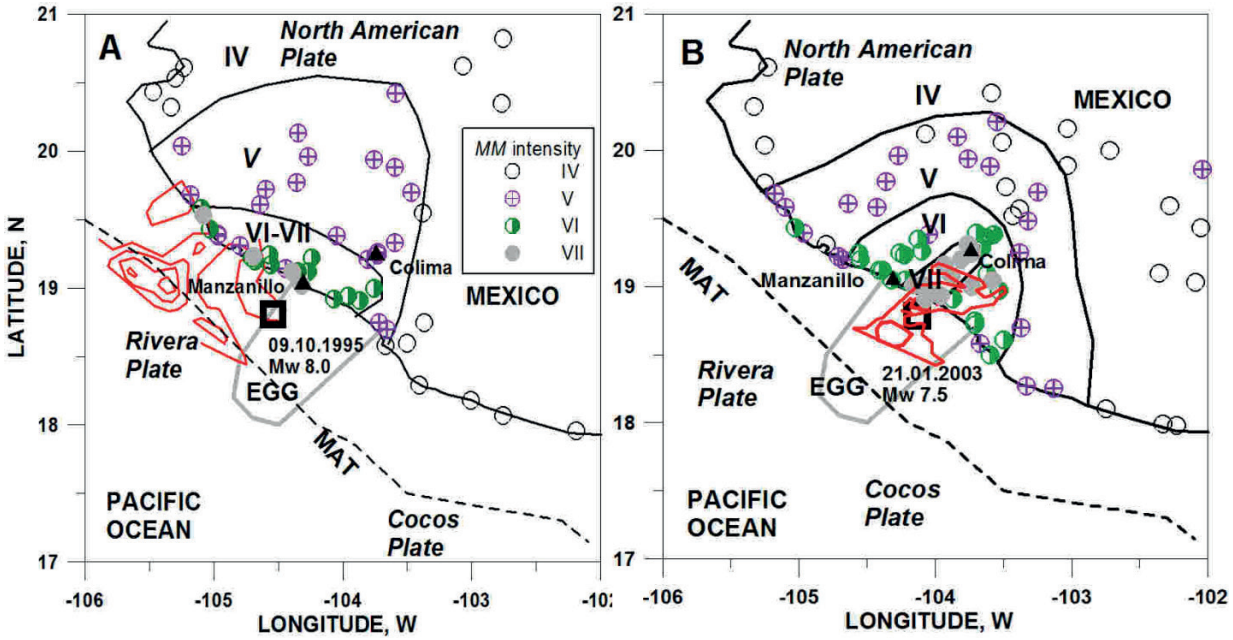

Figure 6. The earthquake intensity patterns observed during the large earthquakes of 9 October 1995 (M_w 8.0) (A) and 21 January 2003 (M_w 7.5) (B). The isolines of co-seismic slip within the rupture plane are shown with red lines (for the 1995 event, according to Mendoza and Hartzell (1999); for the 2003 event, according to Yagi *et al.* (2004). IV–VII are the Modified Mercalli (*MM*) intensities. Open squares show the epicenters of two large earthquakes of 1995 and 2003 located by the Colima regional seismic network RESCO. The cities of Colima and Manzanillo are shown by triangles.

mogeneous set of data, we took as our basis for calculating of the attenuation law only those observations obtained for the same localities for both earthquakes with differences in the estimated intensity between 1 and -1. The earthquake intensity patterns for both earthquakes in direction across the trench, using 44 selected intensity estimations, are shown in Fig. 7A. The least square linear regressions, characterizing the *MM* intensity attenuation I with hypocentral distance R across the coastal

$$I = 1.26\, M_s - 2.24 \log R - 0.0006\, R$$
$$I = 0.92\, M_w - 0.64 \log R - 0.010\, R, \qquad (7)$$

where the hypocentral distance $R = (\Delta^2 + h^2)^{1/2}$ (in km), Δ is the epicentral distance (in km) and h is the focal depth (in km). The intensity I refer to average soil conditions.

According to these equations, the curves of earthquake intensity attenuation for the events with magnitudes M_s and M_w, taken as M_{max} 8.0, were calculated (Fig. 7A). It is seen that taking M_s as M_{max} for the earthquakes, occurring within Zone 1, we can expect larger earthquake intensity at the same distances.

Seismic Hazard of Earthquakes Originated from Zone 2

Zone 2 is outlined in Fig. 3. It represents the epicenters of earthquakes occurring along the crustal local faults of the Colima sector of Jalisco block.

Maximum Magnitude M_{max}

The catalogs of earthquakes, occurring during 1900-2016 within Zone 2, did not give any historically

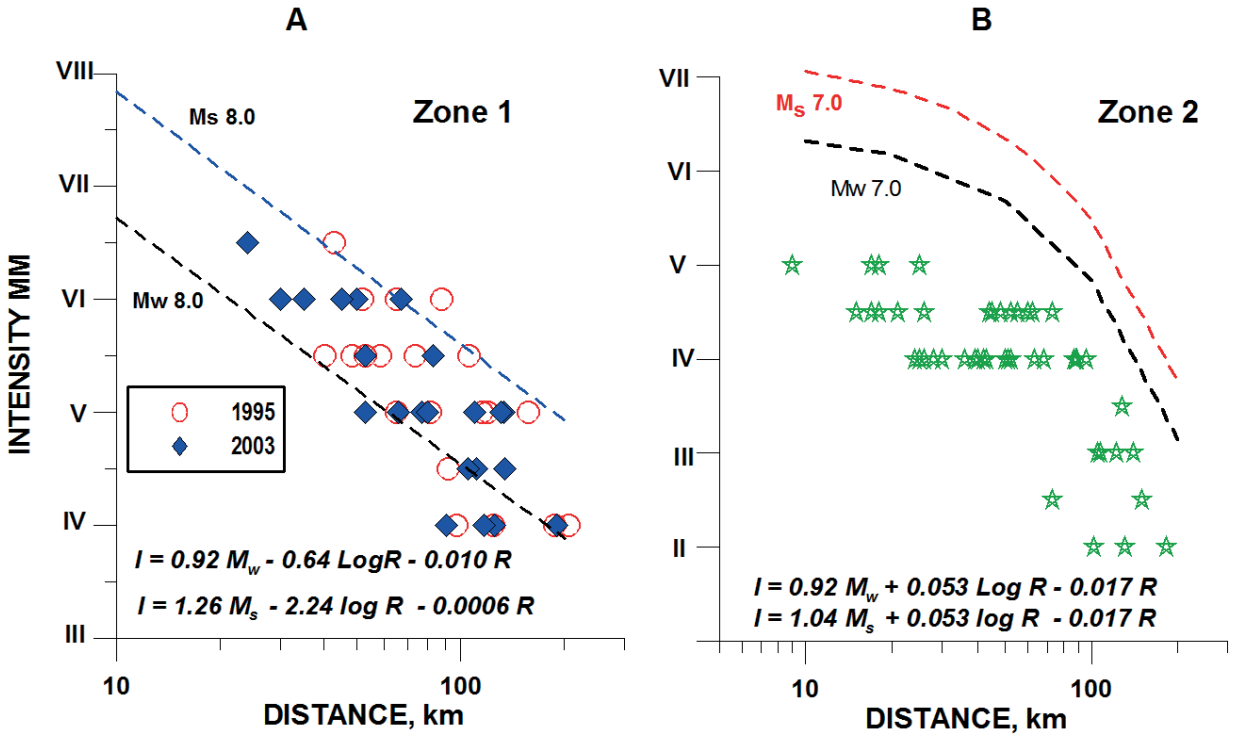

Figure 7. Attenuation of earthquake intensity with distance for events of Zone 1 (A) and Zone 2 (B). In A, the data are shown for large earthquakes of 1995 (No 7) and 2003 (No 8). The curves, calculated with equations, given in A, for earthquakes with magnitudes M_s 8.0 and M_w 8.0, are shown. In B, the data are shown for the M_w 5.3 earthquake of 6 March 2000. The curves, calculated with equations, given in B, for earthquakes with magnitudes M_s 7.0 and M_w 7.0, are shown.

large earthquakes for this Zone. The maximum event was recorded on 6 March 2000 with the magnitude M_w 5.3 (M_s 4.7) (Zobin *et al.*, 2000). It occurred along the Tamazula fault. The event of this size can be produced by movements along the fault of length, L, around 10 km. For the Tamazula fault, which has the length of about 60 km in its part between the Pacific coast and Volcán de Colima (See Fig. 3), the earthquake of 2000 was not maximum, the larger event may occur. We can estimate its size from the empirical relationships between the rupture length, L, and earthquake magnitude, M, obtained for the other seismic zones of the world.

Wells and Coppersmith (1994) proposed the following empirical regression of subsurface rupture length, L, on magnitude M_w for the all-slip-type shallow (depth <40 km) earthquakes:

$$M_w = 4.4 + 1.5 \text{ Log L (km)} \quad (8).$$

According to Eq. (8), the rupture length L = 60 km corresponds to earthquake with magnitude M_w about 7. Therefore, the segment of Tamazula fault, which passes along the Zone 2, has a potential to produce the earthquake with magnitude M_w 7.0 (±0.5).

As was noted in Section 2.2, the large historical earthquake had occurred in December 1567 (or 1568) along the Tepic-Zacoalco graben, representing the northern boundary of Jalisco block (See Fig. 3). The surface rupture of the length of about 60 km, reconstructed from the historical descriptions of this earthquake, corresponds to magnitude M_w 7.2 (Suter, 2015, also based on Eq. 8). There-

fore, the magnitude M_w 7.0 may be considered as the maximum magnitude M_{max} of earthquakes within Zone 2.

Earthquake Recurrence Time

As for Zone 1, the period of recurrence of earthquakes with the magnitude M_{max} for Zone 2 can be estimated using the Gutenberg-Richter law (Eq. 1). The relationship between the number of earthquakes, registered within Zone 2 during the period from 1989 to 2000, and their magnitudes is shown in Fig. 4B. The cumulative distribution of the numbers of earthquakes N against their magnitudes M is linear with a correlation coefficient R = -0.964. The linear regression equation obtained with the least squares method is

$$Log\ N = 4.00 - 0.94\ (\pm\ 0.15)\ M \tag{9}$$

Equation (9) gives us the annual exceedance rate of 0.0026 for earthquakes with the magnitude M_w 7.0, which corresponds to the recurrence period, t, and equal to about 390 years.

Attenuation of Earthquake Intensity with Distance

As was mentioned in Section of *Seismo-tectonic environment of the Colima State*, the largest earthquake, the largest earthquake, recorded within Zone 2, occurred on 6 March 2000. Figure 7B shows the earthquake intensity pattern observed for this earthquake. The intensities were collected for 54 localities of the states of Colima, Jalisco and Michoacán with a visual inspection of the residential houses. For each site, the mean intensity was calculated after the correction for type of masonry. The following equations of attenuation of the intensity, I, with distance, R, were calculated:

$$I = 1.04\ M_s + 0.053\ log\ R - 0.017\ R$$
$$I = 0.92\ M_w + 0.053\ Log\ R - 0.017\ R \tag{10}$$

According to these equations, the curves of earthquake intensity attenuation for the events with magnitudes M_s and M_w, taken as M_{max} 7.0, were calculated (Fig. 7B). It is seen that taking M_s as M_{max} for the earthquakes, occurring within Zone 2, we can expect larger earthquake intensity at the same distances.

Results. Application of the Seismic Hazard Parameters for the Seismic Risk Evaluation for Localities with Low-Rise, Non-Engineered Housing in the State of Colima

Analysis of seismic hazard parameters, proposed for Colima State in Section 4, allowed us to give the prognostics of seismic hazard for localities of the State of Colima. Fig. 8 presents three possible distributions of earthquake intensity for 10 municipal centers in the case of appearance of earthquakes with M_{max} from along-trench (Fig. 8A) and across-trench (Fig. 8B) earthquakes and from the continental fault earthquakes (Fig. 8C). Table 3 summarizes these values for these localities. For following analysis of the seismic risk for the localities, their maximum possible intensity will be taken into account.

The study of seismic risk of a locality is based on its seismic vulnerability assessment and consists of three stages: (1) classification of the buildings and residential blocks of localities, (2) inventory of the

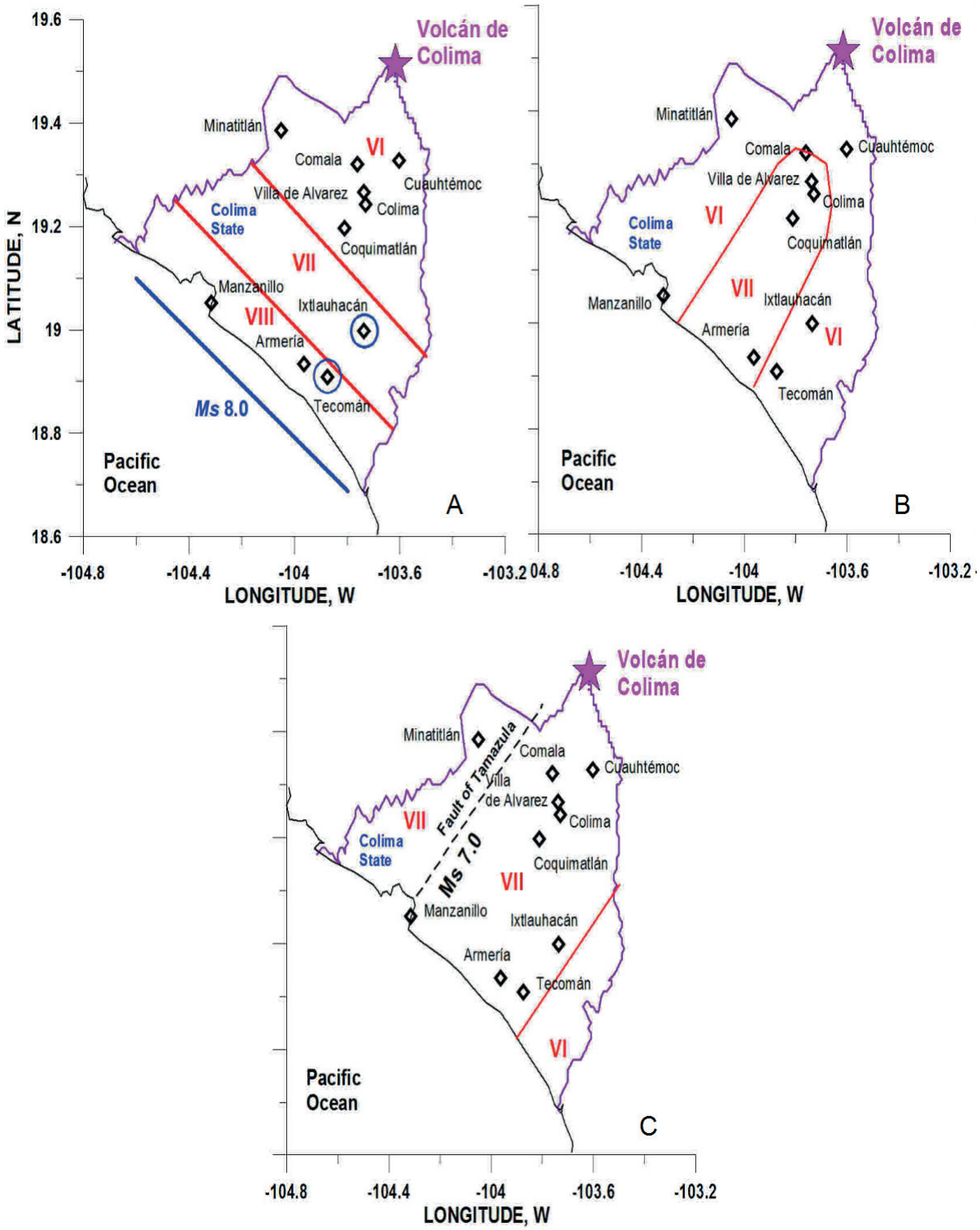

Figure 8. Distribution of zones of earthquake intensity *MM* expected for the localities of the State of Colima in the case of along-trench earthquake of Zone 1 with maximum magnitude *Ms* 8.0 (A), in the case of maximum across-trench earthquake of Zone 1 with magnitude *Ms* 7.8 (B), and in the case of the earthquake of Zone 2 with maximum magnitude *Ms* 7.0 (C). Localities are shown with diamonds. A thick line in A shows the rupture zone of earthquake with magnitude *Ms* 8.0. A dashed line in C shows the Fault of Tamazula.

Table 3. Maximum intensities I_{max} of earthquakes generated within zones I and II for the municipal centers of the State of Colima

Locality	I_{max} of along-trench earthquakes of Zone 1	I_{max} of across-trench earthquakes of Zone 1	I_{max} of earthquakes of Zone II
Colima	VI	VII	VII
Villa de Álvarez	VI	VII	VII
Manzanillo	VIII	VI	VII
Armería	VIII	VII	VII
Tecomán	VIII	VI	VII
Coquimatlán	VI	VII	VII
Ixtlauhacán	VII	VII	VII
Minatitlán	VI	VI	VII
Comala	VI	VII	VII
Cuauhtémoc	VI	VI	VII

Note. These intensity values are presented for intermediate-quality building (Type B) and intermediate type of soil. In the case of bad quality of soil, the values of intensities would be increased (I_{max} + 1).

buildings within the blocks, and (3) construction of damage probabilistic matrices (DPM_block) for different types of blocks for maximum expected earthquake intensity at this locality.

Seismic Vulnerability of Residential Buildings in the State of Colima

The dominant construction types in the Colima state are represented by one- or two-story masonry. Among them, the vulnerable low-rise, non-engineered (LRNE) houses represent most residential constructions. According to the design of these constructions, they can be divided into three groups (Types A, B and C, described in Section of *Evaluation of the seismic vulnerability of the localities with LRNE buildings)*. The characteristic photos of these buildings are shown in Fig. 9.

The residential blocks, consisting of the buildings of three types, were considered as a basic element for the seismic risk zonification. There were identified three types of residential blocks. Type 1 represents the blocks with most A-type buildings and no C-type houses. Type 2 represents the blocks with majority of B-type buildings, and a small proportion of the A- and C-type buildings. Type 3 represents the blocks with most B-type buildings, about 30-40% of C-type houses and the absence of A-type buildings.

Damage Probability Matrix as a Tool to Estimate the Seismic Risk of a Locality

Damage matrices, or vulnerability functions, characterize the probability of material damage expected for each type of masonry during the earthquake, depending on the earthquake intensity and degree of damage (Soares López and Acosta Chang, 1998; Whitman, 1988).

For preparation of DPM, the group of expert's method was used. The experts completed the questionnaires (their form is shown in Table 4), based on their own professional experience, proposing the probability (in %) of damage grade for three types of masonry, affected by earthquakes of different intensities. After a statistical study, the average damage probabilities of each grade for different masonry and the *MM* intensities constitute the DPM.

Figure 9. Examples of three types of residential buildings in municipal centers of Colima state.

The first DPM for three types of masonry in the central part of Colima city was proposed in 1999 for the earthquakes of intensity *MM* VI to IX (Zobin and Ventura-Ramírez, 1999). Later the DPM-1999 was slightly modified in 2007 according to experience, obtained after the 2003 earthquake (Zobin *et al.*, 2010). The DPM-2007, presented in Table 4 and used in this article, was prepared by the group of eleven Colima experts (architects, civil engineers, and structural engineers) having extensive experience in seismic engineering (from 11 to 35 years).

Microzonation of Seismic Risk for two Municipal Centers of the State of Colima

For the following analysis of the seismic risk of localities of Colima we selected two of ten municipal centers, shown in Fig. 8A and marked with circles, the town of Tecomán, situated within zone of maximum seismic intensity *MM* VIII of along-trench earthquakes, and the village of Ixtlahuacán, situated within zones of maximum seismic intensity *MM* VII of along-trench earthquakes and the continental fault earthquakes.

Microzonation of Seismic Risk for the T own of Tecomán

The town of Tecomán is the municipal center with population of 85, 689 inhabitants; its area is equal to 11.97 km2 (INEGI, 2010). Tecomán is located in the Sierra Madre del Sur, which is characterized by outcrops of metamorphic rocks and marine deposits of the Cretaceous. The low-quality alluvial soils are distributed along the margins of the rivers (Atlas de Tecomán, 2011). Tecomán is located at a distance of about 70 km from the Mexican subduction zone. According to Table 3, Tecomán can suffer destructive damage during earthquakes of Zone 1 (I_{max} VIII) and Zone 2 (I_{max} VII).

The evaluation of the housing of Tecomán was carried out during 2014 for 1,361 residential blocks of the town. Of these, 23 (2%) are of type 1, 361 (27%) are of type 2 and 977 (72%) are of type 3. The average distribution of housing of three types within each type of blocks is presented in Table 5A.

To quantify the seismic risk for the housing of Tecomán, represented in these blocks, the probabilistic matrix of expected damages DPM_block for the housing was calculated for expected earthquakes with intensities VII to IX *MM* (Table 6). Intensities VII and VIII *MM* were expected as I_{max} for earthquakes from Zone 2 and Zone 1, respectively (See Fig. 8A and 8C). Intensity IX MM was considered for the case of housing constructed above the low-quality alluvial soils.

Table 4. Damage probability matrix DPM-2007 (in %) for three types of buildings in Colima (intensity MM from VII to IX)

	Type A			**Type B**			**Type C**		
Damage Grade	VII	VIII	IX	VII	VIII	IX	VII	VIII	IX
1	68	46	5	30	15	0	18	8	0
2	24	30	9	17	13	4	12	7	0
3	6	14	17	17	17	5	10	6	4
4	2	5	31	25	15	10	10	11	4
5	0	3	19	7	26	20	29	16	11
6	0	2	13	4	10	35	8	30	21
7	0	0	6	0	4	26	13	21	60

Table 5. Characteristics of the residential blocks in Tecomán (A) and Ixtlahuacán (B)

A

Type of blocks	Number of blocks of each type	Mean number of buildings of Type A	Mean number of buildings of Type B	Mean number of buildings of Type C	% of type A	% of type B	% of type C
Type 1	23	7	2	0	78	22	0
Type 2	361	3	16	1	15	80	5
Type 3	977	2	8	9	11	42	47

B

Type of blocks	Number of blocks of each type	Mean number of buildings of Type A	Mean number of buildings of Type B	Mean number of buildings of Type C	% of type A	% of type B	% of type C
Type 1	0	0	0	0	0	0	0
Type 2	18	0	12	1	2	90	8
Type 3	67	0	6	7	2	43	55

Table 6. Damage probability matrix for three types of residential blocks in Tecomán (in %) for earthquakes with intensity *MM* VII to IX

Damage grade	VII			VIII			IX		
	Blocks of type 1	Blocks of type 2	Blocks of type 3	Blocks of type 1	Blocks of type 2	Blocks of type 3	Blocks of type 1	Blocks of type 2	Blocks of type 3
1	63	34	24	42	19	13	4	1	0
2	23	17	13	28	15	11	8	5	2
3	8	15	12	14	16	11	15	6	5
4	5	21	15	6	13	12	28	13	7
5	4	6	16	2	21	20	2	19	14
6	1	3	5	3	14	20	16	10	24
7	0	0	6	1	3	12	9	22	38

Fig. 10A demonstrates the damage curves for three types of blocks, constructed on the base of Table 6, which illustrate the comparative damage effects. These curves and data of Table 6 indicate that in case of earthquake with intensity VII the damages of both grades 6 and 7 can be expected only for 1% of housing situated within the blocks of type 1. In case of earthquake with intensity VIII the damages of both grades 6 and 7 within this type of blocks can reach 4%, and in case of earthquake with intensity IX this value of damage will be increased up to 25%. For blocks of type 2, the damage of both grades 6 and 7 in housing is expected of 3% in case of earthquake with intensity VII, can reach 17% in case of earthquake with intensity VIII and up to 32% in case of earthquake with intensity IX. For blocks of type 3, totally 11% of damages of grades 6 and 7 in housing can be expected in case of earthquake with intensity VII, 32% in case of earthquake with intensity VIII and 62% in case of earthquake with intensity IX.

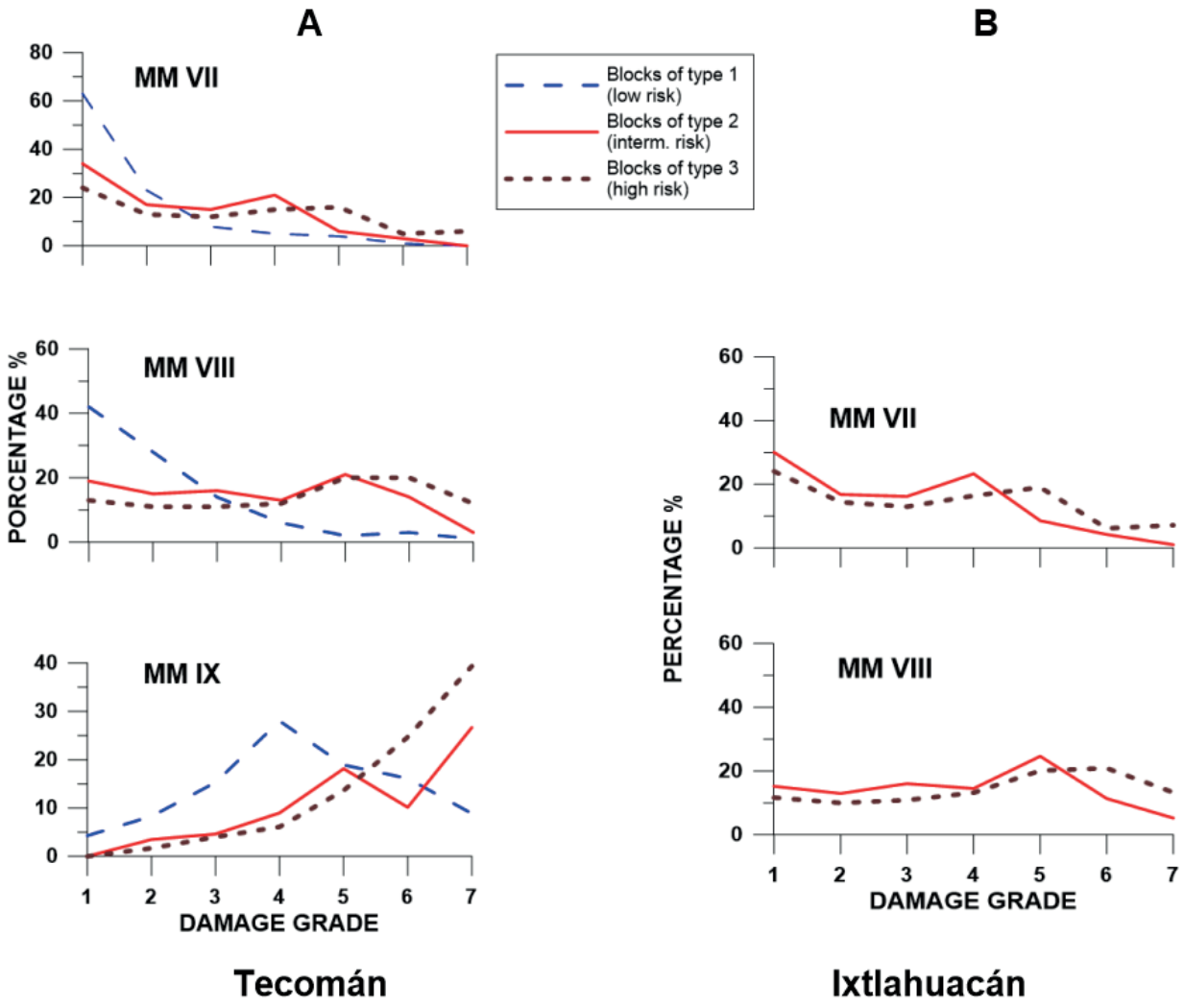

Figure 10. Damage curves corresponding to the DPM-block calculated for three types of residential blocks in Tecomán (A) and Ixtlahuacán (B).

Fig. 11A presents a microzonation of the seismic risk of residential blocks in Tecomán. The blocks with different types of housing do not have a defined distribution. Not numerous blocks of type 1 with relatively low level of seismic risk are located without any regularity. The blocks of type 2 with intermediate seismic risk are dominated here and distributed throughout the entire territory of the settlement. The blocks of type 3 with houses, built of adobe and built without a project, are numerous within this town also and represent the housing of the high seismic risk. They concentrated within the historic center of the city and within outskirts of the town.

Probabilistic appraisal of possible losses in housing of Tecomán, destructed by earthquakes of different intensity, is demonstrated with DPM_cost, giving the percentage of the losses in cost of housing compared with the price of the house before the earthquake. The cost of losses for the residential blocks can be estimated with knowledge of the average cost of all three types of housing that constitutes the blocks. Table 7A shows the percentage of the losses for three types of residential blocks with different level of seismic risk. In the case of earthquake with intensity *MM* VIII, the losses, compared with the price of the housing before the earthquake, will reach 40% for the housing of high level of

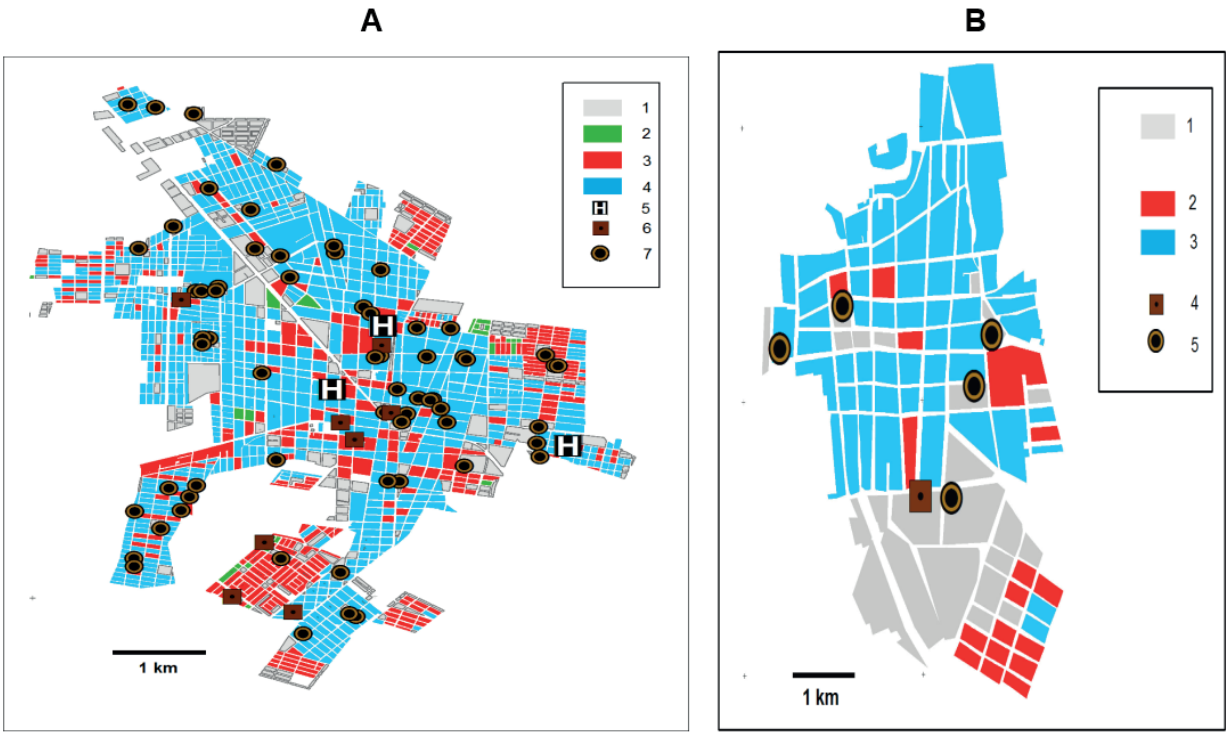

Figure 11. Microzonification of seismic risk for residential blocks of Tecomán (A) and Ixtlahuacán (B). The maps of microzonation of seismic risk represent the distributions of three types of residential blocks which reflected the level of seismic risk for the locality's constructions. In these maps are shown also the positions of hospitals and medical centers, which are important in the case of destructive earthquake, as well as the positions of schools, representing the places of high seismic risk for children. In A: 1, commercial centers and federal zones; 2-4, residential blocks of type 1 (2), type 2 (3) and type 3 (4); 5, hospitals; 6, medical centers; 7, schools. In B: 1, commercial centers and federal zones; 2-3, residential blocks of type 2 (2) and type 3 (3); 4, medical centers; 5, schools. Residential blocks of type 1 represent zone of relatively low risk; residential blocks of type 2 represent zone of relatively intermediate risk; and residential blocks of type 3 represent zone of relatively high risk.

Table 7. Damage probability matrix DPM_cost giving the losses in cost of housing (in %) during earthquakes with intensities *MM* VII, VIII and IX compared with the price of the housing before the earthquake for three types of residential blocks in Tecomán (A) and Ixtlahuacán (B)

A

Intensity *MM*	Blocks of high seismic risk (type 3)	Blocks of intermediate seismic risk (type 2)	Blocks of low seismic risk (type 1)
VII	21	10	4
VIII	40	27	6
IX	65	41	29

B

Intensity *MM*	Blocks of high seismic risk (type 3)	Blocks of intermediate seismic risk (type 2)
VII	14	25
VIII	29	42

seismic risk, 27% for the housing of intermediate level of seismic risk, and 6% for the housing of low level of seismic risk.

Microzonation of Seismic Risk for the Village of Ixtlahuacán

The village of Ixtlahuacán is the municipal center with population of 2,717 inhabitants; its area is equal to 6 km2 (INEGI, 2010). Ixtlahuacán is located within the Sierra Madre del Sur at the heighs of about 150-170 m. Ixtlahuacán is located at a distance of about 110 km from the Mexican subduction zone. According to Table 3, Ixtlahuacán can suffer destructive damage during earthquakes of Zone 1 (I_{max} VII) and Zone 2 (I_{max} VII).

The evaluation of the housing of Ixtlahuacán was carried out during 2014 for 85 residential blocks. The houses are mostly of poor quality. The blocks of type 1 are absent. The housing is represented by 18 (21%) blocks of type 2 and 67 blocks (79%) of type 3. The average distribution of three types of residential buildings within each type of blocks is presented in Table 5B.

To quantify the seismic risk for the housing of Ixtlahuacán, represented in these blocks, the probabilistic matrix of expected damages DPM_block for the housing was calculated for expected earthquakes with intensities VII to IX *MM* (Table 8). Intensity VII *MM* was expected as I_{max} for earthquakes from Zone 2 and Zone 1. Intensity VIII *MM* was considered for the case of housing constructed above the low-quality soils.

Fig. 10B demonstrates the damage curves for two types of blocks, constructed on the base of Table 8, which illustrate the comparative damage effects. These curves indicate that in case of earthquake with intensity VII the damages of both grades 6 and 7 can be expected for 5% of residential blocks of type 2 in case of earthquake with intensity VII, and can reach 16% in case of earthquake with intensity VIII. For blocks of type 3, totally 13% of damages of both grades 6 and 7 in housing can be expected in case of earthquake with intensity VII and 34% in case of earthquake with intensity VIII.

Fig. 11B presents a microzonation of the seismic risk for residential blocks in Ixtlahuacán. As was noted above, the blocks of type 1 with relatively low level of seismic risk are absent. The blocks of type 3, representing the housing of the high seismic risk, are distributed practically throughout the total settlement. The blocks of type 2 with intermediate seismic risk are concentrated mainly within the southern part of the Ixtlahuacán, in the areas of modern urban development.

Table 8. Damage probability matrix for three types of residential blocks in Ixtlahuacán (in %) for earthquakes with intensity *MM* VII and VIII

Damage grade	VII			VIII		
	Blocks of type 1	Blocks of type	Blocks of type 3	Blocks of type 1	Blocks of type 2	Blocks of type 3
1	0	30	24	0	15	12
2	0	17	14	0	13	10
3	0	16	13	0	16	11
4	0	23	16	0	15	13
5	0	9	19	0	25	20
6	0	4	6	0	11	21
7	0	1	7	0	5	13

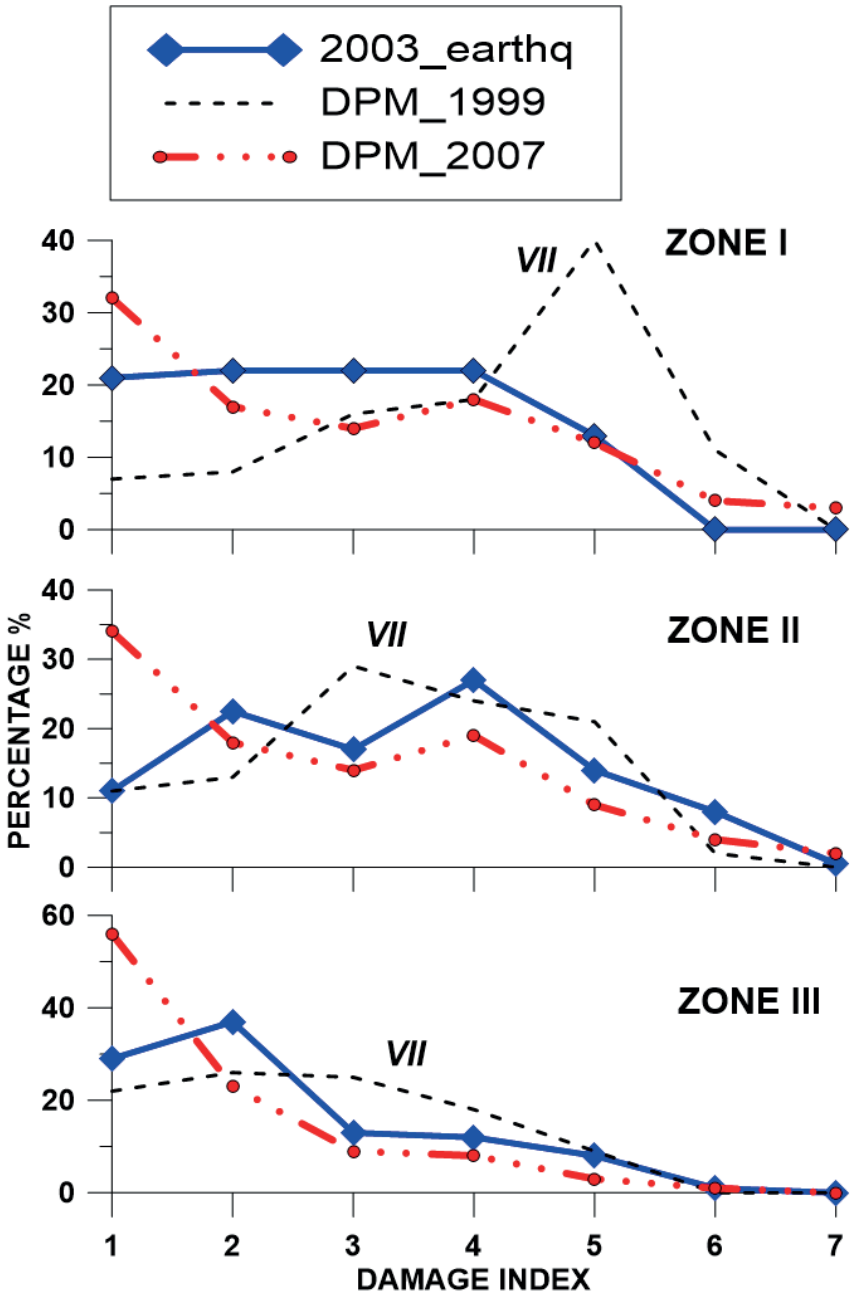

Figure 12. Comparison of observed damage matrix, obtained in Colima city for zones I, II, and III (heavy lines) after the 2003 earthquake, with the prognostic curves, calculated for typical blocks of three zones based on DPM-1999 and DPM-2007, proposed in (Zobin and Ventura-Ramírez, 1999) and (Zobin and Pizano-Silva, 2007) for earthquakes that could be felt in these zones with intensity MM VII (dashed lines).

Probabilistic appraisal of possible losses in housing of Ixtlahuacán, destructed by earthquakes of different intensity, is demonstrated with DPM_cost. Table 7B shows the percentage of the losses for three types of residential blocks with different level of seismic risk. In the case of earthquake with intensity MM VIII, the losses, compared with the price of the housing before the earthquake, will reach 40% for the housing of high level of seismic risk, 27% for the housing of intermediate level of seismic risk, and 6% for the housing of low level of seismic risk.

Discussion

Two elements of the seismic risk, seismic hazard and seismic vulnerability of housing, refer respectively to natural and human activity. The level of seismic hazard, as the natural phenomenon, depends on the magnitude and position of the seismic sources relatively the site of study. Observations of large earthquakes, occurring in the region of study during more than 100 years, allowed us to consider the estimated parameters of the seismic hazard as regular enough.

The seismic vulnerability of housing describes the ability of houses to resist this earthquake action. This element of seismic risk is subjective and depends strongly on the human memory and understanding of destructive effects of previous earthquakes as well as on changing level of the quality of housing. Damage probability matrices, DP*Ms*, are proposed to reflect this understanding and to give notion of possible actions to diminish the risk of loss of life and houses.

Effectivity of DPM, prepared by a group of specialists, may depend on some specific factors. Among them are the existence or not of proper experience of these specialists in sensations of destructive earthquake, and the time interval between destructive earthquakes in the locality. We discuss now the sensibility of proposed DP*Ms* for Colima city on these specific factors.

The first DPM for three types of masonry in the central part of Colima city, described in Section of *Evaluation of the seismic vulnerability of the localities with LRNE buildings* and shown in Figure 9, was proposed in 1999 for earthquakes of intensity *MM* VI to IX for typical blocks of three zones of the city (Zobin and Ventura-Ramírez, 1999). The urban development in Colima has a concentric structure: the older Zone I, which was constructed before 1960, is situated in the central part of the city and is surrounded by Zone II, constructed from 1960 to 1980. The outer circle (Zone III) represents modern buildings. Most old buildings (before 1980) are of types C and B; more recent buildings are of types A and B. Description of the building of three types is given in Section. 2.2. The DPM-1999 version for earthquakes with intensity *MM* VII is shown in Figure 12 for three typical zones of the city.

This DPM was based practically on experience in destructive effects observed in Colima city during the M_w 7.6 earthquakes of 15 April 1941 and of 30 January 1973 (events Nos 3 and 4 in Table 2 and in Fig. 2). In 1941, the total Colima city was situated within Zone I and was occupied mainly with buildings of type C. According to information, presented by the Governor of State in September 1941, 75% of the total 5,115 residential houses of Colima city were destroyed (Bracamontes-Ceballos, 2018). In 1973, the city occupied zones I and II. According to Figueroa (1974), totally 200 residential houses were completely or partially destroyed in Zone I. This information was reflected in the curves of possible damage for housing calculated for three typical blocks based on DPM-1999. As is seen in Figure 12, the prognostic for Zone I predicted, in the case of intensity *MM* VII, heavy damage of index 5 for 40% of the total houses and major damage of index 6 for 10%.

The DPM-1999 was tested soon by the M_w 7.5 2003 earthquake which was felt in Colima city with *MM* VII (Zobin *et al.*, 2006; Zobin and Pizano-Silva, 2007). The 2003 earthquake (event No 8 in Table 2 and Fig. 2) occurred on 21 January near the coast of Colima state. Hypocenter of earthquake was situated within the El Gordo graben, which intersects the Mexican subduction zone and the Middle America trench (See Fig. 6B), locating at a depth of 10 km and at a distance of 65 km from Colima city. The macroseismic investigation of damages produced by the 21 January 2003 earthquake in Colima city, México, was realized for 3,332 constructions within the area of study

representing about 20% of the city area and covered with the different type of constructions. The results of macroseismic study are shown in damage curves (Figure 12).

As is seen, these results for zone I differ with proposed by the curve of DPM-1999. In 2003, Zone I was covered with a mixture of three types of masonry and the experience of 1941 and 1973 did not served. Now only about 15% of housing was characterized by heavy damage of index 5. More modern constructions of zones II and III were better familiar to the members of the 1999 expert group, and it gave a possibility to propose the curves DPM-1999 better corresponding to the 2003 observations of *MM* VII-grade effects in these two zones.

The DPM-2007 version (Table 4) was prepared by the specialists with experience of the 2003 earthquake (Zobin *et al.*, 2007). Figure 12 shows the curves of possible damage, which were calculated for three zones of Colima city based on DPM-2007 for *MM* VII earthquake. These prognostic curves are in good correspondence to the observed damage matrix calculated by Zobin *et al.* (2007) for the effects of the 2003 earthquake and shown in this Figure. Well, we can wait for the next destructive earthquake to check their effectivity. As a practical lesson from these analyses of DP*Ms*, we can propose to re-calculate DPM for every locality each 25-30 years.

The methodology presented in recent article may be applied for many similar in the LRNE housing cities of Asia, Africa, and Latin America. The preliminary reconnaissance carried out in some low-rise cities of the Pacific coast areas of México, Colombia and Perú showed that the buildings of these cities are similar to three types of Colima buildings (Zobin, 2008). This allows the application of this non-instrumental, inexpensive but efficient methodology for the microzonation of seismic risk in the LRNE housing cities situated in similar zones.

Conclusions

This article proposes a simplified methodology of the seismic risk evaluation for the localities, where the vulnerable low-rise, non-engineered (LRNE) housing represents the majority of residential constructions. The methodology is based on evaluation of two main sources of information: the internet-available catalogs of world-wide of recent and historical earthquakes and visual inspection and classification of the vulnerability level of residential LRNE houses, and visual macroseismic inspection of the residential house damage after destructive earthquakes. This methodology was applied to the localities of the State of Colima, México, characterizing with the LRNE type of residential houses. The microzoning of the seismic risk for two localities of the State is presented together with a probabilistic prognostic of the expected financial losses during the maximum intensity earthquakes at the localities. The damage probability matrix DPM-2007, proposed for Colima city, may be used for urban planning for other towns of Colima state as well as of for the cities of other Mexican states situated along the Pacific coast and having similar masonry.

Acknowledgments

The comments of two anonymous reviewers helped to improve the manuscript. The students of Colima University Victor A. Hernández and J. Daniel Ramírez helped us with evaluation of the seismic vulnerability of masonry. This study was supported by Project FOPREDEN “Atlas de peligros y riesgos en el Estado de Colima”.

References

Albayrak, U., Canbaz, M., Albayrak, G. (2015). A rapid seismic risk assessment method for existing building stock in urban areas. Proc. Engineering 118, 1242 – 1249.

Anbazhagan, P. (2011). Introduction to Engineering Seismology. https://nptel.ac.in/courses/105108076/module2/lecture12.pdf.

ATC-13 (1985). Earthquake damage evaluation data for California. Federal Emergency Management Agency, Redwood City, California.

ATC-13-1 (2002). Commentary on the use of ATC-13 earthquake damage evaluation data for probable maximum loss studies of California buildings, Applied Technology Council, Redwood City, 66 pp.

Atkinson, G. (2004). An overview of developments in seismic hazard analysis. Proc. 13th World Conference on Earthquake Engineering, Vancouver, B.C., Canada, 1-22.

Atlas de peligros y riesgos en el Estado de Colima (2015). Gobierno de Colima, Colima. 1307 pp.

Atlas de Tecomán (2011). Actualización de Atlas Municipal de Riesgos y por Amenazas Naturales (Geológicas e Hidrometereológicas) del Municipio de Tecomán, Colima. http://www.normateca.sedesol.gob.mx/work/models/SEDESOL/Resource/2612/Atlas_Estados/06009_TECOMAN/1_ATLAS_TECOMAN.pdf

Bandy, W.L., Michaud, F., Bourgois, J. (2005). Subsidence and strike-slip tectonism of the upper continental slpe off Manzanillo, Mexico, *Tectonophys.*, 398, 115–140.

Blong, R. (2003). A review of damage intensity scales, Natural Hazards, 29, 57-76.

Bormann, P., Giacomo, D. (2010) The moment magnitude and the energy magnitude : common roots and differences. *Journal of Seismology*, Springer Verlag, 2010, 15 (2), pp.411-427.

Bracamontes-Ceballos, B. (2018). El terremoto de 1941 en la Ciudad de Colima: desastre, respuestas y reconstrucción. Tesis, Universidad de Colima, Colima. 267 pp.

Caicedo, C., Yépez, B., Canas, J.A. and Barbat, A.H. (1996). Vulnerabilidad sísmica de edificios en entornos urbanos para estudios de riesgo. En: F.Vidal, M. Espinar y J.A. Esquivel (Ed). Homenaje en Honor al Profesor Fernando de Miguel Martínez, Universidad de Granada, pp. 97-117.

Coburn, A.W., Spence, R.J.S, and Pomonis, A. (1994) Vulnerability and Risk Assessment, Disaster Management Training Programme. http://www.proventionconsortium.org/files/undp/VulnerabilityAndRiskAssessmentGuide.pdf.

Cornell, C. A. (1968). Engineering seismic risk analysis. Bull. Seismol. Soc. Am. 58, 1583–1606.

Courboulex, F., Singh, S.K., Pacheco, J.F., Ammon, C.J. (1997). The 1995 Colima-Jalisco, Mexico, earthquake (M_w 8): A study of the rupture process. *Geophys. Res. Lett.*, 24, 1019-1022.

de Cserna, Z. (1989). An outline of the geology of Mexico, in The Geology of North America, A. W. Bally and A. R. Palmer (Editors), Vol. A, Boulder, Colorado, 233-264

Deniz, A., Korkmaz, K.A., and Irfanoglu, A. (2010). Probabilistic Seismic Hazard Assessment for Izmir, Turkey. *Pure Appl. Geophys.* 167 (2010), 1475–1484

EERI Committee on Seismic Risk (1984). Glossary of terms for probabilistic seismic-risk and hazard analysis, Earthquake Spectra 1: 33–40.

Eleftheriadou, A.K. and Karabinis, A.I. (2013). Evaluation of damage probability matrices from observational seismic damage data. Earthquakes and Structures, Vol. 4, No. 3, 1-27.

Figueroa, A.J. (1974). Sismicidad en Colima. Macrosismo del 30 de enero de 1973. Informe No 332, Instituto de Ingeniería, UNAM, México. 51 p.

Garduño-Monroy, V.H., Saucedo-Girón, R., Jiménez, Z., Gavilanez-Ruiz, J.C., Cortés-Cortés, A. y Uribe-Cienfuentes, R.M. (1998). La falla Tamazula, limite suroriental del bloque de Jalisco y sus relaciones con el complejo volcánico de Colima. *Revista Mexicana de Cien. Geol.*, 15: 132-144.

Kuroiwa, J. (2004). Disaster Reduction, Quebecor World Peru, Lima, 496 pp.

Manual (1993). Manual de diseño por sismo, Comisión Federal de Electricidad, México, D.F., 162 p.

McGuire, R. K. (2004). Seismic hazard and risk analysis, Earthquake Engineering Research Institute, MNO-10, 240 pp

Maqsood S. T., Schwarz J. (2009). Building vulnerability and damage during the 2008 Baluchistan earthquake in Pakistan and past experiences. *Seismol. Res. Lett.*, 81, 514–525. doi:10.1785/gssrl.81.3.514

Montalvo-Arrieta, J.C., Sosa-Ramírez, R.L. and Pérez-Campos, X. (2017). Evaluation of macroseismic intensities in Mexico from recent earthquakes using ¿Sintió un sismo? (Did you feel it?). *Geofís. Intern.,* 56, 27-36. DOI: 10.19155/geofint.2017.056.1.3.

Musson, R.M.W. and I. Cecic (2002). Macroseismology, In: International Handbook of Earthquake and Engineering Seismology, Part A (eds. W.H.K. Lee, H. Kanamori, P.G. Jenning, and C. Kisslinger). Academic Press, Amsterdam, pp. 807–822.

Pacheco, J.F. and R.L. Sykes (1992). Seismic moment catalog of large shallow earthquakes, 1900 to 1989. *Bull. Seismol. Soc. Am.*, 82, 1306-1349.

Papanikolaou, A. and Taucer, F. (2004). Review of non-engineered houses in Latin America with reference to building practices and self-construction projects, ELSA, 2004, 258p.

Petersen, M.D., Harmsen, S.C., Jaiswal, K.S., Rukstales, K.S., Luco, N., Haller, K.M., Mueller, C.S., and Shumuay, A.M. (2018). Seismic hazard, risk, and design for South America. *Bull. Seismol. Soc. Am.*, 108, 781–800.

Peterson, J. and Hutt, C.R. (2014). World-Wide Standardized Seismograph Network: A Data Users Guide. USGS, Open-File Report 2014–1218. 74 p.

Sayın E., Yön B., Calayır Y., Karaton M. (2013). Failures of masonry and adobe buildings during the June 23, 2011, Maden-(Elazığ) earthquake in Turkey. Engineering Failure Analysis. 34:779–791. doi:10.1016/j.engfailanal.2012.10.016

Singh, S.K., Ponce, L. and Nishenko, P.S. (1985). The great Jalisco, Mexico, earthquakes of 1932: Subduction of the Rivera Plate. *Bull. Seismol. Soc. Amer.*, 75, 1301-1313.

Soares López, J. y Acosta Chang, J. (1998). Microzonación sísmica de la ciudad de Ensenada, B.C. GEOS, 18, 265.

Suárez, G., García-Acosta, V. and Gaulon, R. (1994). Active crustal deformation in the Jalisco block, México: evidence for a great historical earthquake in the 16th century. Tectonoph., 234, 117-127.

Suter, M. (2015). The A.D. 1567 M_w 7.2 Ameca, Jalisco, Earthquake (Western Trans-Mexican Volcanic Belt): Surface Rupture Parameters, Seismogeological Effects, and Macroseismic Intensities from Historical Sources. *Bull. Seismol. Soc. Am.*, 105, 646-656.

Tejeda-Jácome, J. and Chávez-García, F.J (2007). Empirical ground-motion estimation equations in Colima from weak motion records. ISET *J. Earthq. Technol.*, 44, 409–419.

Yon, B., Sayin, E. and Onat, O. (2017). Earthquakes and structural damages. In: Earthquakes - Tectonics and Risk Mitigation (Ed. T. Zouaghi). IntechOpen. DOI: 10.5772/65425. Available from: https://www.intechopen.com/chapters/52524.

Wang, Z. (2009). Seismic hazard vs. seismic risk, *Seismol. Res. Lett.* 80, 673–674

Wang, Z. (2011). Seismic Hazard Assessment: Issues and Alternatives. *Pure Appl. Geophys.* 168 (2011), 11–25

Wells, D.L. and Coppersmith, K.J. (1994). New empirical relationships among magnitude, rupture length, rupture width, rupture area, and surface displacement. *Bull. Seismol. Soc. Am*, 84, 974-1002.

Whitman, R.V. (1973). Damage probability matrices for prototype buildings. Structures publication 380. Boston: MIT.

Whitman, R. V. (1988). Earthquake loss estimation methodology, In: A. Vogel and K. Brandes (eds), Earthquake Prognostics, Wiesbaden: F. Vieweg & Sohn, pp. 259–278.

Wood, H.O. and Neumann, F. (1931). Modified Mercalli intensity scale of 1931. *Bull. Seismol. Soc. Am*, 21, 277-283.

Zobin, V.M. (2008). Microzonation of seismic risk in a low-rise city based on the macroseismic evaluation of the vulnerability of residential buildings. Conference paper. 2008 GSA Cordilleran/ Rocky Mountain Joint Section Meeting.

Zobin, V.M. and Ventura-Ramírez, J.F. (1998). The macroseismic field generated by the M_w 8.0 Jalisco, México, earthquake of 9 October 1995. *Bull. Seismol. Soc. Amer.*, 88, No 3, 703-711.

Zobin, V.M. y Ventura Ramírez, J.F. (1999). Vulnerabilidad sísmica de edificios residenciales y pronóstico de daños en caso de sismos fuertes en la ciudad de Colima. GEOS, 19, No. 3, 152-158.

Zobin, V.M., Reyes-Dávila, G.A., Pérez-Santa Ana, L.M., Ramírez-Vázquez, C.A. y Ventura-Ramírez, J.F. (2000). Estudio macrosísmico del temblor de Colima (M_w 5.3) del 6 de marzo de 2000. GEOS, 20, No 4, 414-417.

Zobin, V. M., Ventura-Ramírez, J. F., Gutiérrez-Andrade, C., Hernández-Cruz, L. and Santibáñez-Ibáñez, S. (2006). The M_w 7.4 Colima, Mexico, earthquake of 21 January 2003: The observed damage matrix in Colima city and its comparison with the damage probability matrix. Natur. Hazards, 38, 391-410.

Zobin, V.M. and J.A. Pizano-Silva (2007). Macroseismic study of the M_w 7.5 21 January 2003, Colima, México, across-trench earthquake. Bull. Seismol. Soc. Am., 97, 1221-1232. DOI: 10.1785/0120060080

Zobin, V., F. Ventura, A. Cruz y E. Arellano (2009). Microzonificación de riesgo sísmico para las ciudades pequeñas del estado de Colima de acuerdo con el nivel de vulnerabilidad de la vivienda. Memorias, XVII CNIS, Artículo II-22, Nov. 11-14, 2009, Puebla, México.

Zobin, V.M., Cruz-Bravo, A.A. and Ventura-Ramírez, J.F. (2010). Microzonation of seismic risk in a low-rise Latin American city based on the macroseismic evaluation of the vulnerability of residential buildings: Colima city, México. *Nat. Hazards Earth Syst. Sci.*, 10, 1347-1358, 2010. doi:10.5194/nhess-10-1-2010.

Zúñiga, R., Suárez, G., Ordaz, M., and Garcia-Acosta, V. (1997). Seismic hazard in Latin America and Caribbean: Volume 2, México. Project 89-0190. IDRC, Ottawa, Canada. 82 pp.

Original paper

https://doi.org/10.22201/igeof.00167169p.2022.61.2.2201

Voyager's Observations in the Vicinity of the Heliopause

R. A. Caballero-López[1] and J. D. Richardson[2]

Received: November 20, 2021; accepted: February 1, 2022; published on-line: April 1, 2022.

Resumen

Este trabajo analiza las observaciones del Voyager 2 en noviembre de 2018 y las compara con lo detectado por el Voyager 1 en las proximidades de la heliopausa en julio-agosto de 2012. Describimos las variaciones del plasma y los rayos cósmicos a la distancia radial de ≈ 1 unidad astronómica (AU) de la heliopausa. Usamos un modelo simple de modulación de los rayos cósmicos por convección-difusión para explicar cualitativamente las observaciones de partículas. Encontramos una capa delgada, con un espesor de 0.04 AU en la cual desaparece la componente radial de la velocidad del viento solar, la intensidad de los rayos cósmicos galácticos aumenta rápidamente para alcanzar su nivel en la frontera de la heliosfera, y disminuye la intensidad de los iones heliosféricos de baja energía. Llamamos a esta capa la "piel de la heliosfera". Los datos de plasma sugieren que el Voyager 2 cruzó la heliopausa el 5 de noviembre de 2018, a la distancia radial de 119.03 AU. Aplicamos nuestro análisis a las observaciones del Voyager 1 y concluimos que un comportamiento similar en la velocidad del viento solar podría cualitativamente explicar la intensidad observada de los rayos cósmicos galácticos y que la "piel de la heliosfera" puede ser una característica global a lo largo de la heliopausa.

Palabras Clave: Sol, heliosfera, heliopausa, viento solar y rayos cósmicos.

Abstract

This work analyzes Voyager 2 observations on November 2018 and compares them with Voyager 1 data at the vicinity of the heliopause in July-August 2012. We describe the plasma and cosmic-ray variations at the radial distance of ≈ 1 astronomical unit (AU) from the heliopause. We use a simple convection-diffusion cosmic-ray modulation model to qualitatively explain the particle observations. We found a thin layer, with a thickness of ≈ 0.04 AU where the radial component of the solar wind speed vanished, the galactic cosmic ray intensity rapidly increased to reach its heliosphere boundary level, and low-energy heliospheric ion intensity drooped. We called this layer the "skin of the heliosphere". Plasma data suggest that Voyager 2 crossed the heliopause on November 5, 2018, at the radial distance of 119.03 AU. We apply our analysis to Voyager 1 observations and conclude that similar behavior in solar wind speed could qualitatively explain the GCR counting rate and that the "skin of the heliosphere" maybe a global characteristic along the heliopause.

Key words: Sun, heliosphere, heliopause, solar wind and cosmic rays.

**Corresponding author at rogelioc@geofisica.unam.mx*

[1] *Instituto de Geofísica, Universidad Nacional Autónoma de México, Ciudad Universitaria, 04510, CDMX, MEXICO*

[2] *Kavli Institute for Astrophysics and Space Research, Massachusetts Institute of Technology, Cambridge, MA, USA*

Introduction

On July 28, 2012, at the distance of 121.33 AU, and after traveling for 35 years, Voyager 1 crossed the heliopause, the boundary of our solar system, and entered the interstellar space (Burlaga & Ness 2014). Since then, the onboard detectors have been recording magnetic field, particle and wave data from the interstellar medium. Because of the plasma instrument onboard Voyager 1 is off from early 2007, there is not any observation on solar wind velocity in the vicinity of the heliopause.

Krimigis *et al.* (2011) calculated the anisotropies of low-energy particles observed by Voyager 1 in the heliosheath. From their results, these authors predicted that the spacecraft entered into a transition layer at the distance of ≈ 113 AU, where the radial component of the solar wind speed (VR) went down to zero, meaning that about 8 AU inside the heliosheath from the heliopause, the solar wind plasma became azimuthal. At the same time, the cosmic-ray instrument did not observe any abrupt change in the high-energy galactic cosmic-ray intensity (see for instance Webber *et al.* 2012; Burlaga & Ness 2014), which means that radial inward diffusion and outward convection processes were unaffected by the new solar wind conditions in the transition layer. Only a few days before Voyager 1 crossed the heliopause, galactic cosmic-ray intensity showed an abrupt increase to reach its heliosphere boundary value.

Cosmic Ray Subsystem (CRS) onboard Voyager 1 started to observe large increases in GCRs and significant decreases in low-energy heliospheric ions in July–August 2012 (Stone *et al.* 2013). Figure 1 shows (in red) these particles observations, shifted in time by six years and 99 days for easier comparison with Voyager 2 observations in 2018. The overall picture is that when Voyager 1 approached to the heliopause the radial intensity gradient for GCRs and heliospheric ions changed, and after the heliopause crossing (HPX) it eventually reached the interstellar level. Base on CRS observations, these authors concluded that the HPX for Voyager 1 was on August 25, 2012 (day 238). Before that day, GCR intensity had two temporary increases, that were simultaneous with decreases of low-energy ions. However, the analysis of magnetic field data made by Burlaga & Ness (2014) showed that from about a month early (July 28, day 210) Voyager 1 started to observe the interstellar magnetic field. These authors concluded that on the day 210, V1 crossed a current sheet having the structure of a tangential discontinuity. This current sheet (CS0) is represented in Figure 1 by the solid red vertical line. According to these authors, Voyager 1 observed a sector boundary before CS0 (shown by the second right dash line in panel A and B, called SB-1), where the magnetic field azimuthal angle change from "away" to "toward" polarity. At CS0 the azimuthal angle changed from "toward" to "away" polarity. The first right dash line was identified by Burlaga & Ness (2014) as a beginning of the first of two step increases in GCR intensity observed by Voyager 1 in 2012. The last five vertical lines after CS0 represent five particle boundaries, none of then associated with magnetic field polarity change. The final particle boundary occurred on August 25. Magnetic field observations after the first GCR step increase did not allow these authors to conclude about the nature of this region (heliosheath or interstellar origin). Their conclusion that Voyager 1 has been detecting the magnetic field of interstellar origin from CS0 crossing, is supported by the fact that magnetic field polarity has not changed since then.

Burlaga & Ness (2014) also pointed out that the two temporal changes in galactic and heliospheric particles could be explained if we assume that in this region (after CS0) there were heliospheric tube flux connected to the interstellar medium as proposed by Opher & Drake (2013) and heliosheath

particles may enter this tube and restore the intensity of low-energy ions. Following the results of Burlaga & Ness (2014), in this work, we will consider that the heliopause crossing was on July 28, 2012. Our qualitative analysis will not be affected by this assumption.

Observations made by plasma and cosmic-ray instruments on board Voyager 2 indicated that this spacecraft crossed the heliopause at the distance of ≈ 119 AU. Figure 1 shows Voyager 2 plasma observations (in blue): plasma density (panel D) and the radial component of the solar wind speed (panel C) from day 100 to day 309 of 2018. These data reveal, for the first time in the space era, the plasma parameters at the heliopause, on November 5, 2018 (day 309). In the interval of five days (from November 1 to November 5) plasma density jumped from about 0.002 cm^{-3} to 0.0093 cm^{-3} (4.65 times), and the radial component of solar speed went from about 74 km/s to zero. Since then, plasma data disappeared from the three sunward pointed detectors. This fact is a clear indication that the Voyager 2 crossed the heliopause and entered the new region in front of the heliosphere. During these five days, the cosmic-ray detector on Voyager 2 observed that the counting rate of > 70 MeV galactic protons (panel A) showed a very high gradient of about 100%/AU, and the counting rate of low-energy heliospheric ions (panel B) started dropped to a level below the detector background.

These simultaneous observations of plasma and galactic cosmic rays indicate that once VR went to zero, meaning that radial convection and radial diffusion are also zero, the solar modulation of cosmic rays vanished. Therefore, just in this thin layer of the heliosphere (we call it "skin of the heliosphere") with a thickness of about 0.04 AU, the cosmic-ray intensity must increase to reach its value at the heliopause. This work aims to show a simple qualitatively explanation of the Voyager 2 observations in the vicinity of the heliopause and show a possible scenario for radial solar wind profile when Voyager 1 crossed the heliopause in 2012.

Cosmic-Ray Modulation in the Vicinity of the Heliopause

The cosmic-ray transport equation was first derived by Parker (1965), and the details of this and subsequent derivations, and its various solutions were reviewed by Moraal (2013). The lowest- order approximation is the so-called Convection-Diffusion formalism (CD) which assumes spherical symmetry of the heliosphere, ignores adiabatic energy changes and assumes a steady-state, so that the transport equation, for the omnidirectional distribution function, $f(r, p)$ is reduced to:

$$Vf - \kappa \partial f / \partial r = 0, \tag{1}$$

where r is the radial position, p is the particle momentum (energy), V is the radial solar wind speed, and κ is the diffusion coefficient.

The CD model is a good approximation of the transport equation for high-energy cosmic rays and close to the modulation boundary (see for instance Caballero-Lopez & Moraal 2004). The reason is:

1) energy change is an accumulative modulation effect, and therefore it is bigger in the inner than in the outer heliosphere), 2) high-energy particles are less affected by energy changes and 3) in the outer heliosphere drift in the radial direction plays little role. CD model is also the simplest model for solar modulation.

The solution of the Eq. 1 is

$$f = f_b e^{-M}, \tag{2}$$

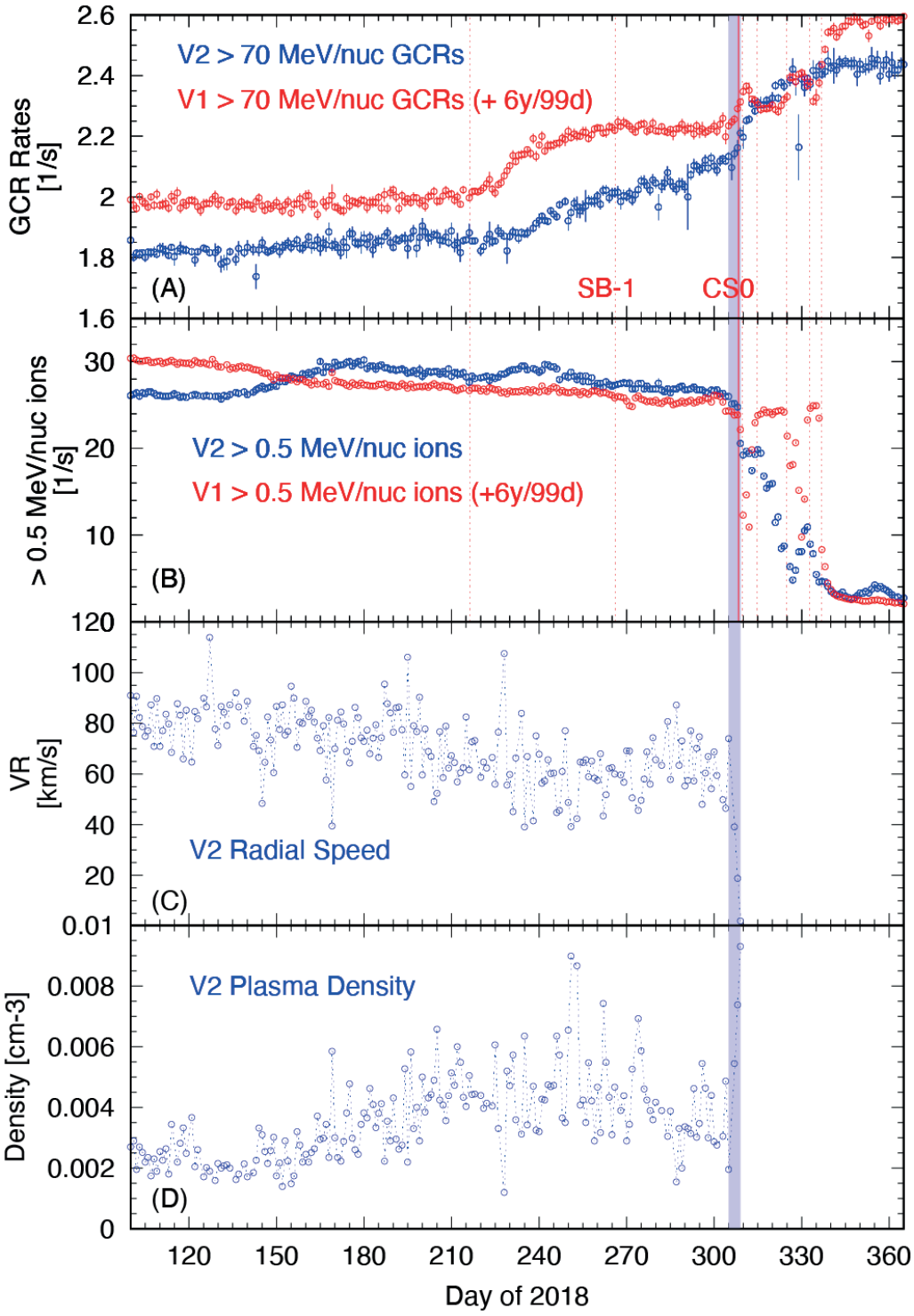

Figure 1. Voyager 1 (in red) and Voyager 2 (in blue) observations. We show daily averages of (A) counting rate for high-energy GCRs, (B) low-energy ions, (C) V2 radial component of the solar wind speed, and (D) V2 plasma density. Vertical red lines are from Burlaga & Ness (2014) (see text for explanation). The blue rectangular band shows the region where the radial component of the solar wind speed abruptly dropped, and the plasma density rapidly increased, ending on November 5, 2018 (day 309). This behavior on radial speed and plasma density is an indication of the Heliopause crossing. Since then, Voyager 2 is outside of the Heliosphere

where $M = \int_r^{r_b} \frac{V dr}{\kappa}$, and f_b is the local interstellar spectrum (LIS) at the outer boundary, r_b , of the heliosphere (heliopause).

The modulation parameter M describes the level of reduction of cosmic-ray intensity from the LIS value (M = 0 at the heliopause). In this model, if the radial component of the solar wind speed is zero, M vanishes, and therefore the intensity reaches its interstellar value. However, the quantity that determines the modulation parameter is the ratio V/κ, and it is challenging to know which is the appropriate value for the diffusion coefficient, from the available observations. For our analysis, we consider the diffusion coefficient in the form $\kappa = \beta P \kappa_o(r)$ (P is the particle rigidity, β the ratio of particle velocity to the spped of light). We point out that we will only use this model to qualitatively describe the last months of Voyager observations inside the heliosphere (about 1 AU from the heliopause, see Table 1). In this region, the radial transport of the galactic cosmic rays plays the relevant role on the intensity variations observed by the spacecraft. We must notice that the cosmic rays in this layer have just entered the overall modulation region.

Finally, in our analysis, we use the interstellar spectrum observed by Voyager 1 and described in Vos & Potgieter (2015). For our study, this spectrum is sufficient because we are looking at the qualitative picture of the cosmic-ray modulation in the thin region close to the heliopause.

Results and Discussion

In Figure 2 we present the results of our analysis for Voyager 2 observations. From ≈ 118 AU, VR (blue line in bottom panel) started to decrease at approximately a constant rate from 75 km/s to 60 km/s at ≈ 118.3 AU, and kept this value for 2.5 months until V2 reached the distance of 118.99 AU, where VR dropped to zero on the day 309 of 2018 (November 5) at 119.03 AU. On the other hand, cosmic-ray detector observed an increase in the intensity gradient of the > 70 MeV protons from 118 AU (≈ 3%/AU), when VR was decreasing from 75 to 60 km/s (see top panel of Figure 2). At about 118.34 AU, the cosmic-ray intensity gradient increased at a constant rate of ≈ 22%/AU until the day 305 at the radial distance of 118.99 AU. When VR abruptly went to zero in the next five days, the intensity rapidly increased by ≈ 100%/AU. Although this happened in a very short radial distance, this gradient of GCR is much larger than those previously observed by Voyager 1&2 in the heliosheath (see for instance Webber *et al.* 2012).

To apply the CD model to these observations, we use a VR profile, shown in red (bottom panel of Figure 2). Using Eq. 1, we compute the distribution function, f. Then, taking into account the relationship between f and the observed intensity (j) as $j \propto P^2 f$, we obtained the counting rate for GCR protons, and therefore the radial intensity gradient is calculated by the expression:

$g_r = \frac{1}{f}\frac{\Delta f}{\Delta r} = \frac{1}{j}\frac{\Delta j}{\Delta r}$. The top panel of Figure 2 shows in blue the observed counting rate from CRS onboard Voyager 2 and with red line the modulated rate as result of the convection-diffusion model, using the diffusion coefficient shown in Table 1. As we can see, the diffusion coefficient, needed to fit the observed rate, is decreasing toward the heliopause, having its smaller value in a thin layer at the heliopause; and therefore the radial gradient of GCRs entering the heliosphere decreases from the heliopause in agreement to the observations. We must mention that this is a qualitative analysis, and therefore it gives us a possible explanation for the observed quantity. In particular, we are very interested in point out the existence of the "skin of the heliosphere", with a thickness of about

0.04 AU, that clear appears just five days before Voyager 2 crossed the heliopause. The CD model properly reproduces the galactic counting rate through it. This layer is characterized by 1) the radial component of the solar wind speed vanishes, 2) the GCR intensity rapidly increases with a gradient of about 100%/AU, and 3) the intensity of heliospheric low-energy ions starts the final rapidly decrease to reach the interstellar level.

These Voyager 2 plasma observations motivated us to describe a possible scenario for solar wind speed when Voyager 1 crossed the heliopause on July 28, 2012. Counting rate of GCR protons observed by Voyager 1 shows the following features. 1) From day 100 (≈ 120.3 AU) to day 117 (≈ 120.44 AU) the radial gradient was ≈ 6%/AU. 2) Then, when the first step increase began, the radial gradient increased to ≈ 23%/AU until it reached a plateau when Voyager 1 crossed the sector boundary SB-1 on about the day 167 (≈ 120.93 AU). 3) From day 167 to day 206 (≈ 121.3 AU) the radial gradient was small, ≈ 2%/AU. And 4) in the next five days until Voyager 1 crossed the heliopause on the day 210 (≈ 121.33 AU) the radial gradient jumped to ≈ 93%/AU. These changes in the radial gradient are the results of spatial variations in the magnetic turbulence that affect the diffusion of cosmic rays. However, there is a lack in the understanding of the turbulence regime in this region of the heliosphere. Despite the plateau region between SB-1 and CS0, the counting rate at V1 is similar to that observed at V2 just before the HPX.

As we mentioned early, Voyager 1 plasma instrument was off at that time, so we did not have solar wind speed data during the heliopause crossing. Decker *et al.* (2012) estimated the radial component of the solar wind from the analysis of the low-energy charged particle observations on board Voyager

1. According to Figure 3 (panel j) of that paper, VR at the beginning of 2012 is very low, about 10 km/s. We use this VR value and assume a similar radial dependence as for Voyager 2 to apply the CD model to GCR rate at Voyager 1. This dependence of VR is shown in the bottom panel of Figure 3.The result is shown with a red line in the top panel of Figure 3. In bottom panel, we present the radial solar wind speed profile, similar to that of Voyager 2 in Figure 2. For the CD model, the diffusion coefficient has the same energy dependence, but its level is different, as suggested by different radial gradient mentioned above. In Table 1 we can see that the diffusion coefficient applied to V1 observations follows the V2 diffusion coefficient radial dependence: increased from the heliopause (except for the plateau region where perhaps the turbulence was very low). It is important to note that, the diffusion coefficients used in this work depend on the assumptions of the radial component of the solar wind, and therefore, they only give an indication of the relative level of the turbulence in each region. The "skin of the heliosphere" at the Voyager 1 location was the same as that observed by Voyager 2, about 0.03 AU. This "skin" is a remarkable picture of the heliosphere boundary.

Table 1. Diffusion coefficient, $\kappa_o(r)$, normalized to its value at the boundary: $\kappa_o(r_b)_{V2} = 7.2 \times 10^{19} cm^2 s{-}1 GV^{-1}$; $\kappa_o(r_b)_{V1} = 2.7 \times 10^{18} cm^2 s^{-1} GV^{-1}$.

Voyager 2 Day of 2018	Distance (AU)	$\kappa o/\kappa o(r_b)$	Voyager 1 Day of 2012	Distance (AU)	$\kappa o/\kappa o(r_b)$
180–190	117.90–117.99	62.5	100–117	120.29–120.44	222.2
190–230	117.99–118.34	56.3	117–167	120.44–120.93	26.4
230–305	118.34–118.99	10.8	167–206	120.93–121.30	444.4
305–309	118.99–119.03	1	206–210	121.30–121.33	1

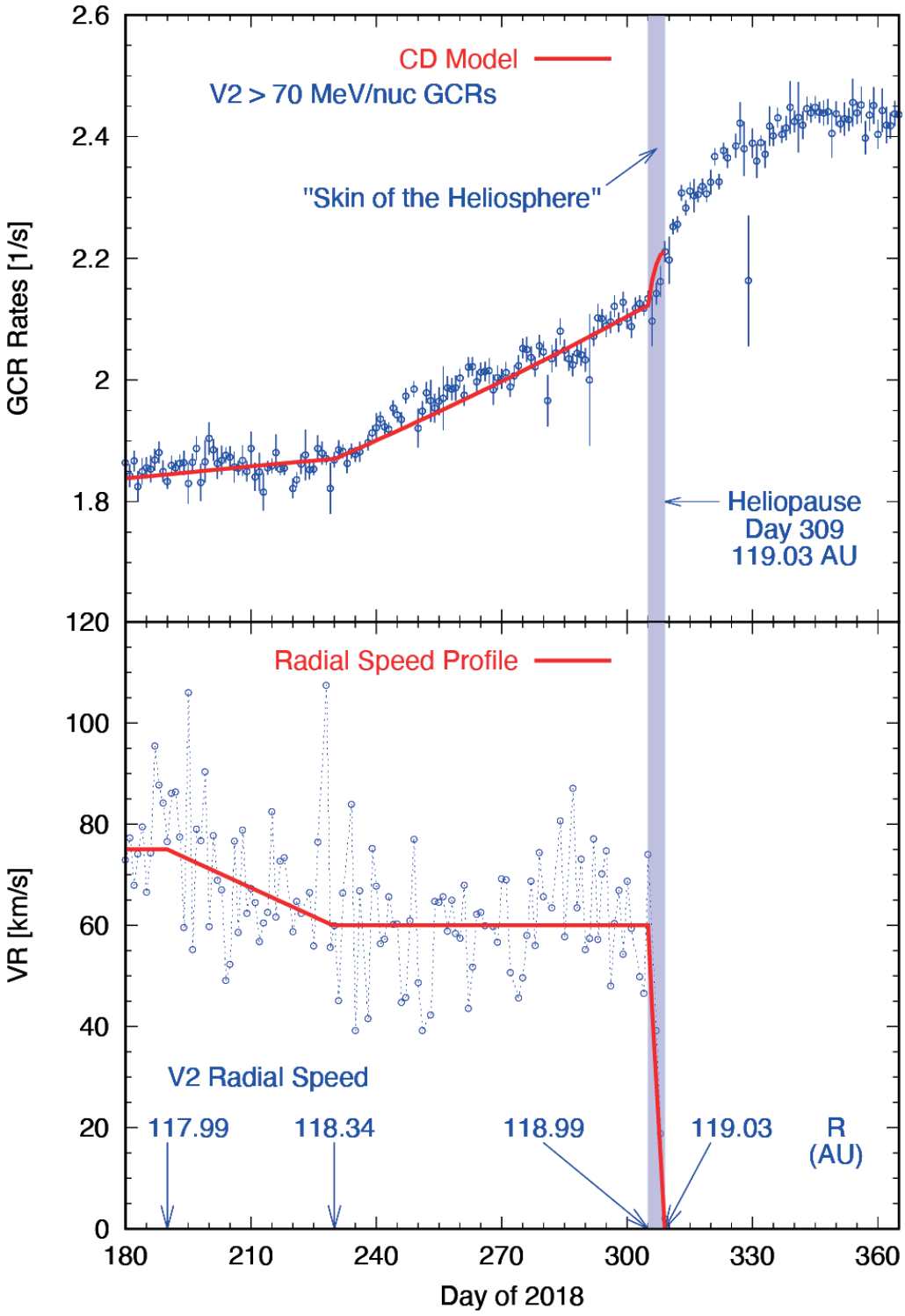

Figure 2. Voyager 2 observations in the vicinity to the heliopause. The top panel shows the daily average counting rate for galactic cosmic-ray protons, > 70 MeV (in blue), red line is the result of the modulation, explained in the text. In the bottom panel we present the radial component of the solar wind speed (in blue). The red line is a qualitative representation for speed.

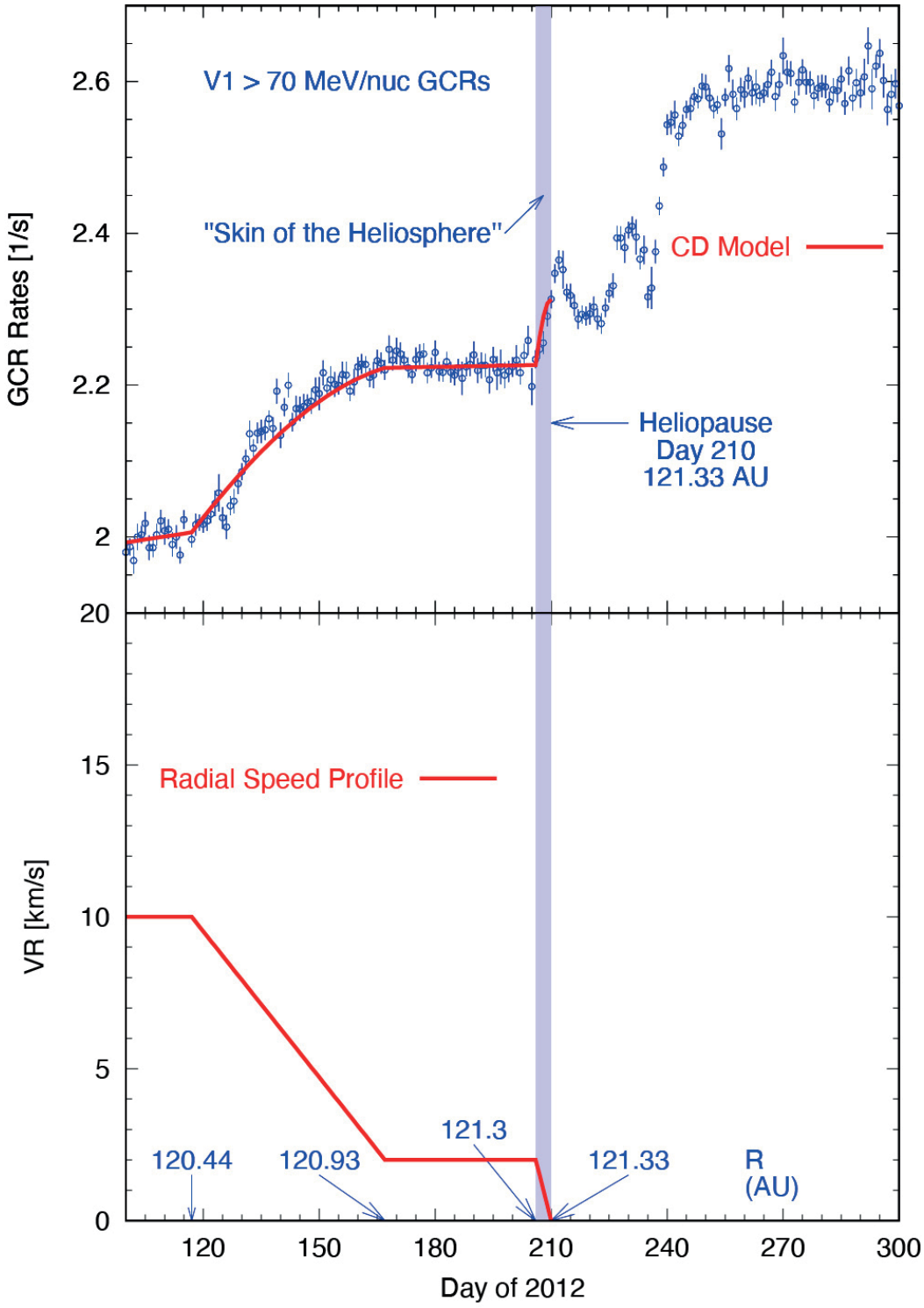

Figure 3. Voyager 1 observations close to the heliopause. Top panel: counting rate daily averages for galactic cosmic-ray protons, > 70 MeV (in blue), the red line is the result of the modulation, explained in the text. The bottom panel shows the assuming radial profile of the solar wind speed, similar to the observed at Voyager 2.

Conclusions

This work presented the recent plasma and cosmic-ray observations made by Voyager 2 in the vicinity of the heliopause. The simple convection-diffusion modulation model supported the analysis. We propose the existence of a thin layer on the heliosphere boundary, called here "skin of the heliosphere", with a thickness of about 0.04 AU. This "skin" has four features: 1) the radial component of the solar wind speed vanishes, 2) rapidly increase in the plasma density, 3) rapidly increase in GCR intensity to reach the outside spectrum, and 4) low-energy heliospheric ion intensity start to drop to a very low level outside of the heliosphere.

Another important conclusion is that the observed "skin" during Voyager 2 heliopause crossing could also be during Voyager 1 crossing in 2012. Therefore, it may be a global layer along the heliopause. The similarity in the observed galactic cosmic-ray intensity by Voyager 1&2 in the vicinity of the heliopause, suggests that radial component of the solar wind speed was different from zero (but very small, ≤ 10 km/s) up to the Voyager 1 entered this "skin" just four days before the heliopause crossing.

JDR is supported by NASA. We thank the Cosmic Ray Subsystem team (E. Stone, P.I.) for providing data via their web site.

References

Burlaga L. F., & Ness N. F., 2014, Voyager 1 observations of the interstellar magnetic field and the transition from the heliosheath, *ApJ*, 784:146 (14pp), doi:10.1088/0004-637X/784/2/146.

Caballero-Lopez R. A. , & Moraal H., 2004, Limitations of the force field equation to describe cosmic ray modulation, *J. Geophys. Res.*, 109, A01101, doi:10.1029/2003JA010098.

Decker R. B., Krimigis S. M., Roelof E. C, & Hill M. E., 2012, No meridional plasma flow in the heliosheath transition region, *Nature*, 489, 124–127, doi:10.1038/nature11441.

Krimigis S. M., Roelof E. C., Decker R. B., & Hill M. E., 2011, Zero outward flow velocity for plasma in a heliosheath transition layer, *Nature*, 474, pp. 359–361, doi:10.1038/nature10115.

Moraal H., 2013, Cosmic-ray modulation equations, *Space Sci. Rev.*, 176, pp. 299–319, doi:10.1007/s11214-011-9819-3.

Opher M., & Drake J. F., 2013, On the rotation of the magnetic field across the heliopause, *ApJL*, 778, L26 (6pp), doi:10.1088/2041-8205/778/2/L26.

Parker E. N., 1965, The passage of energetic particles through inter- planetary space, *Planet. Space Sci.*, 13, pp. 9–49.

Stone E. C., Cummings A. C., McDonald F. B., *et al.*, 2013, Voyager 1 observes low-energy galactic cosmic rays in a region depleted of heliospheric ions, *Science*, 341, pp. 150-153, doi:10.1126/science.1236408.

Vos E. E. & Potgieter,M. S., 2015, New modeling of galactic proton modulation during the minimum of solar cycle 23/24, *ApJ*, 815:119 (8pp), doi:10.1088/0004-637X/815/2/119.

Webber W. R., McDonald F. B., Cummings A. C., Stone E. C., Heikkila B., & Lal N., 2012, Sudden intensity increases and radial gradient changes of cosmic ray MeV electrons and protons observed at Voyager 1 beyond 111 AU in the heliosheath, *Geophys. Res. Lett.*, 39, L06107, doi:10.1029/2012GL051171.